

Master's thesis

# New insight on heart failure using strain rate tensors from motion-encoded MRI

**Lasse Totland**

Biological and Medical Physics  
60 ECTS study points

Department of Physics  
Faculty of Mathematics and Natural Sciences

Spring 2024



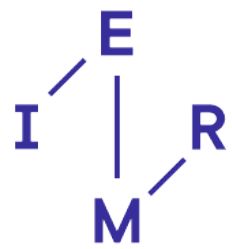
**Lasse Totland**

New insight on heart failure  
using strain rate tensors from  
motion-encoded MRI

Supervisor:  
Emil Knut Stenersen Espe

# Scientific environment

This thesis was carried out at the Institute of Experimental Medical Research, Oslo University Hospital (IEMR, OUS) as part of the MSc study program "Biological and Medical Physics" at the Department of Physics, University of Oslo (UiO).





# Acknowledgements

Firstly, I especially want to thank my supervisor, Emil, for coming up with a really interesting master's project. Our many discussions over the last year on heart dynamics and MR physics have been very exciting and insightful, and your enthusiasm for the field and my work was inspiring and motivating throughout. I can confidently say that this thesis is my proudest work, and it would not have happened without your guidance and encouragement.

My thesis is built upon the previous work done by the MR group at IEMR, and would not have been possible without their exciting research on cardiology and imaging techniques. I want to sincerely thank Einar, Gary, Bård, Kaja, Ioanni, Lili, Ida Marie, Vidar and Emil who were involved with the handling of the study animals and the MR acquisitions that were used in my analysis. I also want to thank the many other talented and inspirational people at IEMR for including me in meetings and events, showing interest in my work and for sharing their thoughts on my findings from a medicine and biology perspective. The experience and insight I have gained from being a small part of this medical research institute in the past year has been very valuable, and I feel better equipped for a career in medical physics because of it.

I want to thank my fellow students at UiO. Your companionship during my bachelor and master studies in Oslo has made the countless courses, lectures, assignments, lab experiments, exams and my thesis work an unforgettable experience and it would not have been as fun without you. I especially want to thank my comrade Sander who has been sharing an office with me at IEMR throughout the last year. As physics students with next to no experience with cardiology and medical research we both had a lot to learn, but it was certainly easier doing it together.

Lastly, I want to thank my friends and family for encouraging and supporting me throughout my studies and believing in me all the way.



# Abstract

**Background:** Heart failure (HF) is life-threatening disease that is increasing in prevalence, and is a major priority in global public health. Left ventricular (LV) strain measurements can be used as an early indicator of myocardial dysfunction after infarct. Previous studies have proven the possibility of deriving strain rate tensors from motion-encoded Magnetic Resonance Imaging (MRI) data to describe the direction and magnitude of deformation on voxel scale, though this method has not yet been implemented to investigate heart dysfunction.

**Aim:** Our aim was to apply this method to gain new insight on regional myocardial function in rat hearts after myocardial infarction using 3D Tissue Phase Mapping (TPM) data of the left ventricle with high spatial and temporal resolution. We also explored the possibility of using strain rate tensor direction, irrespective of strain rate magnitude, to describe myocardial function.

**Materials & Methods:** First, to validate the method, a framework developed in Python was used to reproduce global and regional strain and strain rate curves from 2D short-axis (SHAX) cross-sections of the LV that were compared to literature using established methods. The framework was then used to assess the 2D and 3D direction of strain rate independently from the conventions of radial, circumferential and longitudinal axes as well as the development of these measurements as a function of days post-infarct. The measurements were compared to a sham-operated control group.

**Results:** Global values of circumferential strain and strain rate calculated using our framework agreed well with similar studies using different methods and modalities. Regional analysis revealed that the strain rate magnitude is reduced in the infarcted area and that this area has reduced strain compared to the other LV wall sections and the Sham control group. Our data also indicate that the strain rate angles, relative to radial direction from the LV center, become less uniform over time after infarct.

**Conclusion:** We have shown, for the first time, that strain rate tensor analysis of TPM MRI data as a tool to assess regional myocardial strain and strain rate is functional and shows potential. We have also, for the first time, used strain rate angle distributions to identify regional myocardial dysfunction.



# Contents

<b>Scientific environment</b>	<b>i</b>
<b>Acknowledgements</b>	<b>iii</b>
<b>Abstract</b>	<b>v</b>
<b>Abbreviations</b>	<b>1</b>
<b>1 Introduction</b>	<b>3</b>
<b>2 Theory</b>	<b>5</b>
2.1 MR theory overview . . . . .	5
2.1.1 The spin . . . . .	5
2.1.2 RF pulse . . . . .	6
2.1.3 Slice selection . . . . .	7
2.1.4 k-space . . . . .	9
2.1.5 Pulse sequences . . . . .	10
2.1.6 Motion encoded MRI . . . . .	12
2.2 Heart physiology . . . . .	14
2.2.1 Heart anatomy and the cardiac cycle . . . . .	14
2.2.2 Myocardial infarction . . . . .	15
2.3 Myocardial strain and strain rate . . . . .	16
<b>3 Material and Methods</b>	<b>21</b>
3.1 Data overview . . . . .	21
3.1.1 Rat MI model . . . . .	21
3.1.2 MRI Acquisition . . . . .	22
3.2 Strain rate tensor analysis framework . . . . .	22
3.2.1 LV segmentation models . . . . .	23
3.2.2 The velocity field . . . . .	24
3.2.3 Numeric implementation of Selskog method . . . . .	26
3.2.4 Ellipsoid tensor visualization . . . . .	27
3.2.5 Eigenvector decomposition . . . . .	29
3.2.6 Global LV strain rate . . . . .	30
3.2.7 Global LV strain . . . . .	32
3.2.8 Regional strain rate and strain . . . . .	33

3.2.9	Eigenvector angle distributions . . . . .	34
3.2.10	Framework adjustments for 3D analysis . . . . .	35
3.2.11	Parameter summary . . . . .	36
3.3	Statistical analysis . . . . .	37
3.3.1	Linear regression . . . . .	38
3.3.2	T-tests . . . . .	38
<b>4</b>	<b>Results</b>	<b>39</b>
4.1	2D strain rate tensor analysis . . . . .	39
4.1.1	Visualization . . . . .	39
4.1.2	Tensor field optimization . . . . .	39
4.1.3	Global strain rate and strain . . . . .	41
4.1.4	Regional strain rate and strain . . . . .	42
4.1.5	Eigenvector angle distribution . . . . .	44
4.1.6	MI progression . . . . .	45
4.2	3D strain rate tensor analysis . . . . .	47
4.2.1	Global strain rate and strain . . . . .	47
4.2.2	Regional strain rate and strain . . . . .	48
4.2.3	Eigenvector angle distribution . . . . .	49
4.2.4	MI progression . . . . .	53
<b>5</b>	<b>Discussion</b>	<b>55</b>
5.1	2D strain rate tensor analysis . . . . .	55
5.1.1	Tensor field visualization . . . . .	55
5.1.2	Tensor field optimization . . . . .	56
5.1.3	Global strain rate and strain . . . . .	56
5.1.4	Regional strain rate and strain . . . . .	58
5.1.5	Eigenvector angle distribution . . . . .	59
5.2	3D strain rate tensor analysis . . . . .	60
5.2.1	Global strain rate and strain . . . . .	60
5.2.2	Regional strain rate and strain . . . . .	61
5.2.3	Eigenvector angle distributions . . . . .	62
5.3	Statistical considerations . . . . .	63
5.4	Other limitations and suggestions for future work . . . . .	64
<b>6</b>	<b>Conclusion</b>	<b>67</b>
	<b>Bibliography</b>	<b>73</b>

# Abbreviations

<b>HF</b>	Heart Failure
<b>LV</b>	Left Ventricle
<b>MRI</b>	Magnetic Resonance Imaging
<b>TPM</b>	Tissue Phase Mapping
<b>SV</b>	Stroke Volume
<b>EDV</b>	End-Diastolic Volume
<b>EF</b>	Ejection Fraction
<b>STE</b>	Speckle Tracking Echocardiography
<b>CMR</b>	Cardiovascular Magnetic Resonance
<b>CMR-FT</b>	CMR Feature Tracking
<b>PC-MRI</b>	Phase Contrast MRI
<b>ECC</b>	Eddy Current Compensation
<b>MI</b>	Myocardial Infarction
<b>SHAX</b>	Short Axis
<b>RF</b>	Radio Frequency
<b>Tx</b>	Transmitter Coil
<b>Rx</b>	Receiver Coil
<b>FID</b>	Free Induction Decay
<b>FT</b>	Fourier Transform
<b>GRE</b>	Gradient Echo

<b>TR</b>	Repetition Time
<b>TE</b>	Echo Time
<b>VENC</b>	Velocity Encoding
<b>LA</b>	Left Atrium
<b>RA</b>	Right Atrium
<b>RV</b>	Right Ventricle
<b>LGE</b>	Late Gadolinium Enhancement
<b>T<sub>es</sub></b>	Time point of end systole
<b>T<sub>ed</sub></b>	Time point of end diastole
<b>SE</b>	Standard Error
<b>IVR</b>	Isovolumetric Relaxation
<b>TDE</b>	Tissue Doppler Echocardiography

Abbreviations of all parameter names used in the statistical analysis can be found in section 3.2.11.

# Chapter 1

## Introduction

Heart failure (HF) is a life-threatening disease that affects more than 64 million people worldwide, and attempts to decrease its social and economic burden have become a major priority in global public health (1). Despite available treatment options, morbidity remains high, the diagnosis is increasing in prevalence with an aging population and the healthcare expenditure is projected to increase dramatically (2). HF significantly affects quality of life by impairing social and mental health (3). Despite being a widely researched topic, many aspects of the disease remains unknown.

HF is characterized by a reduction in the heart's ability to pump a sufficient amount blood to the body (4). This can be due to decreased blood supply to certain parts of the heart muscle tissue (myocardium) leading to areas of necrotic infarct tissue that cannot contribute to mechanical pumping work. This can lead to a myocardial infarction (MI), also referred to as a "heart attack" (5). A parameter that can measure reduced myocardial function is the ejection fraction (EF), which describes the ability of the left ventricle (LV) to deform relative to its maximum volume: the end-diastolic volume (EDV). EF is defined as the ratio between the stroke volume (SV) and the EDV, where the SV is the difference between the EDV and the smallest LV volume during the cardiac cycle (6).

While a decrease in EF can be an accurate indicator of global reduction in myocardial function by revealing reduced deformability, this parameter is not sensitive to regional changes and tends to be unable to show significant reduction in function before the late stages of the disease (7). An alternative parameter is "strain", which is a measurement of deformation of an object relative to its initial length (8). It has been shown that regional strain analysis of the LV can be an early non-invasive indicator of myocardial dysfunction by quantifying the amount of deformation (contracting and stretching) in different areas of the LV myocardium (9). This kind of analysis studies strain or strain rate along radial, circumferential and longitudinal axes as defined by LV geometry (10). Myocardial motion is complex and three-dimensional, however, and attempting to quantitatively study LV dynamics unrestricted by these geometric conventions has not been done quantitatively before and could reveal a new understanding of regional dysfunction.

The established methods of regional LV strain analysis can be done using several imaging modalities. Speckle tracking echocardiography (STE) uses naturally occurring speckle patterns in the myocardium seen in ultrasound scans to assess tissue deformation (11). Cardiovascular magnetic resonance (CMR) also plays a large role in regional LV strain analysis. The CMR "tagging" method selectively magnetizes the myocardium in a grid shape at the start of the heart cycle, and follows the relative motion of the grid lines over time to quantify strain (12). CMR feature tracking (CMR-FT) is a post-processing method that tracks the motion of shapes and textures in image sequences from any cine CMR acquisition to measure deformation (13). These methods allow for regional strain measurements that can be used as a supplement to LV EF to determine earlier if and where a patient is developing cardiac diseases, such as HF, and to more confidently determine if they would benefit from treatment (14).

The methods mentioned above have all been used successfully in research and clinical applications, but all of the strain and strain rate data were presented in the context of conventional LV geometry. An alternative CMR method has been shown to be capable of producing discrete measurements of deformation magnitude and direction on voxel-scale through the application of strain rate tensors on time dependent velocity fields from phase contrast MRI (PC-MRI), although this method has never been applied on hearts with MI or in quantitative deformation analysis of the LV (15). Applying this method to high resolution PC-MRI data could reveal complex 3D LV dynamics related to dysfunction that have not previously been possible to measure with the established methods.

**Aim:** The aim of this thesis is to apply strain rate tensor analysis on PC-MRI data of rat hearts to study the effects of MI on regional LV dysfunction after infarct, which has never been done before. To do this we will first prove that this method is a viable tool to measure cardiac deformation parameters by comparing global strain rate and strain measurements to literature. Different LV segmentation models will be used to look at regional variation in 2D cross-sectional and 3D whole-LV data. We will also make use of the strain rate tensor's unique properties to study the direction of strain rate in 2D and 3D and, for the first time, attempt to parameterize this in a way that relates to myocardial function. We will also study how the functional parameters in the hearts develop up to 6 weeks post-infarct compared to a healthy control group. Using this analysis framework, we will attempt to gain new insight into the dynamics of how myocardial dysfunction develops as the infarcted regions grow.

# Chapter 2

## Theory

This chapter introduces some fundamental MR physics, heart physiology and the mathematics of strain rate tensor calculation. This will be the theoretical foundation for the work done in this thesis and the discussion of our findings. In later chapters we will describe the methods that will be used, and how they are developed and implemented from the theory.

### 2.1 MR theory overview

In this section we will establish a basic theoretical foundation of the physics behind MRI, based on the compendium "Physics of MR imaging" from the FYS4740 course at the University of Oslo (16). All topics covered in this chapter can be read about in greater detail in this compendium.

#### 2.1.1 The spin

The most prominent atom in the human body is the hydrogen, found in water molecules and many others. The nucleus of a hydrogen atom is a single proton, and for the sake of simplicity we will imagine the human body as a heterogeneous collection of protons where different tissues have different densities.

In an MR image, a voxel contains signals that are generated from the protons within it. To understand how this signal is produced and measured, it is useful to think of the protons as spinning magnetic dipoles. More precisely, we say that these dipoles "precess" around the static  $B_0$ -field from the MRI magnet at the Larmor frequency:

$$\omega_0 = \gamma B_0, \quad (2.1)$$

which is proportional to the  $B_0$  field strength, where  $\gamma$  is the gyromagnetic ratio defined by the material or tissue. We refer to these dipoles as "spins". Other nuclei with an odd number amount of protons also have a spin property, but hydrogen has a higher  $\gamma$ . This

makes it easier to detect, which further supports our simplification that living tissue is a collection of protons.

When an object is placed within the magnet it does not initially produce an interpretable signal. At this point in time, each spin in a voxel precess either parallel or anti-parallel with the  $\vec{B}_0$  field direction. Opposite direction spins cancel out, and we end up with a vector sum pointing parallel, which represents the net magnetization vector  $\vec{M}$  as illustrated in Figure 2.1. As long as  $\vec{M}$  points parallel to the field, we consider it to be in an equilibrium position. To generate an MR signal, we need to disturb this rest state.

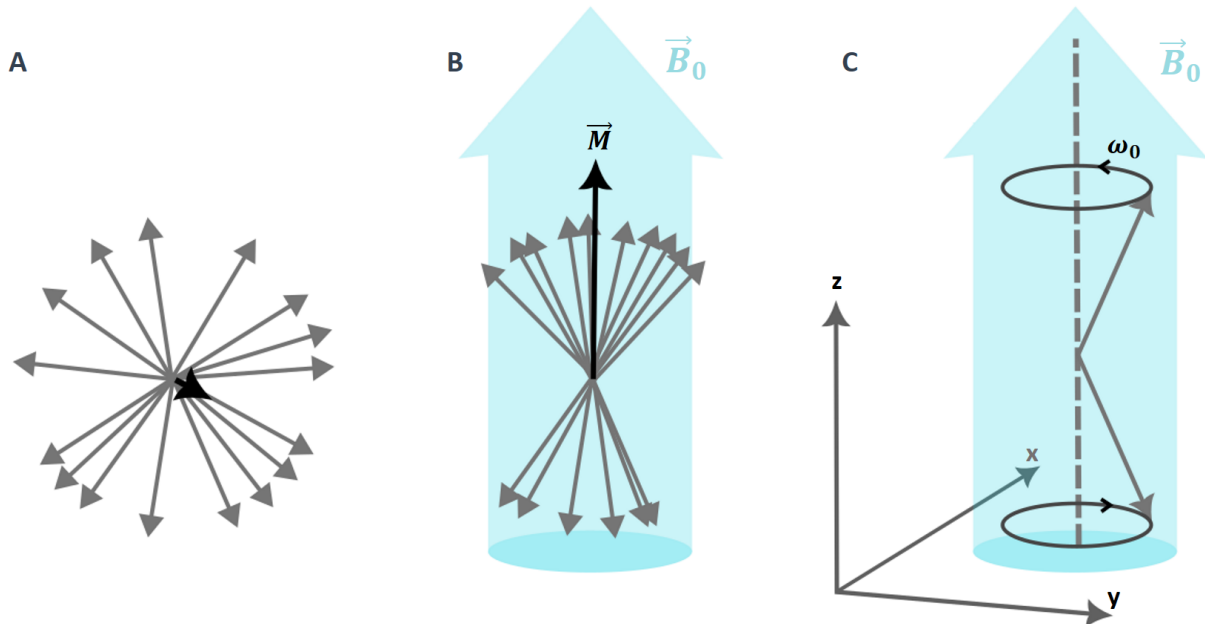


*Figure 2.1: A: A group of spins (gray vectors) pointing in random directions, with no meaningful vector sum. B: The same spins with a magnetic field  $\vec{B}_0$  applied, creating a parallel net magnetization vector  $\vec{M}$  shown here in its equilibrium position. C: Component parallel and anti-parallel spins precessing around  $\vec{B}_0$  at the Larmor frequency  $\omega_0$ .*

## 2.1.2 RF pulse

Using an orthogonal second field  $\vec{B}_1$ , generated by a radio frequency (RF) pulse, to knock  $\vec{M}$  out of its equilibrium down towards the transverse plane (at a flip angle  $\alpha$ ) is what leads us to the signal we need. The RF field alternates directions at a rate of  $\omega_0$  to resonate with the spins and effectively move  $\vec{M}$  without having to overpower the strong  $\vec{B}_0$  field. As  $\vec{M}$  is moved down at some angle and its composite spins precess in phase, what separates signal from different tissues is how it recovers back to the rest state via two types of "relaxation".  $T1$  relaxation is measured by the time it takes for  $\vec{M}$  to become parallel to  $\vec{B}_0$  again, and  $T2$  relaxation depends on the time it takes for the composite spins to move out of phase with each other again. An MR image can be  $T1$  or  $T2$  weighted, depending on the anatomy and type of tissue we are interested in. Figure 2.2 demonstrates how the precession of  $\vec{M}$  in the transverse plane induces a current in a magnetically sensitive receiver coil ( $Rx$ ). Because of the strong  $B_0$  field,

the receiver coils can only measure signal from the transverse plane perpendicular to  $B_0$ .

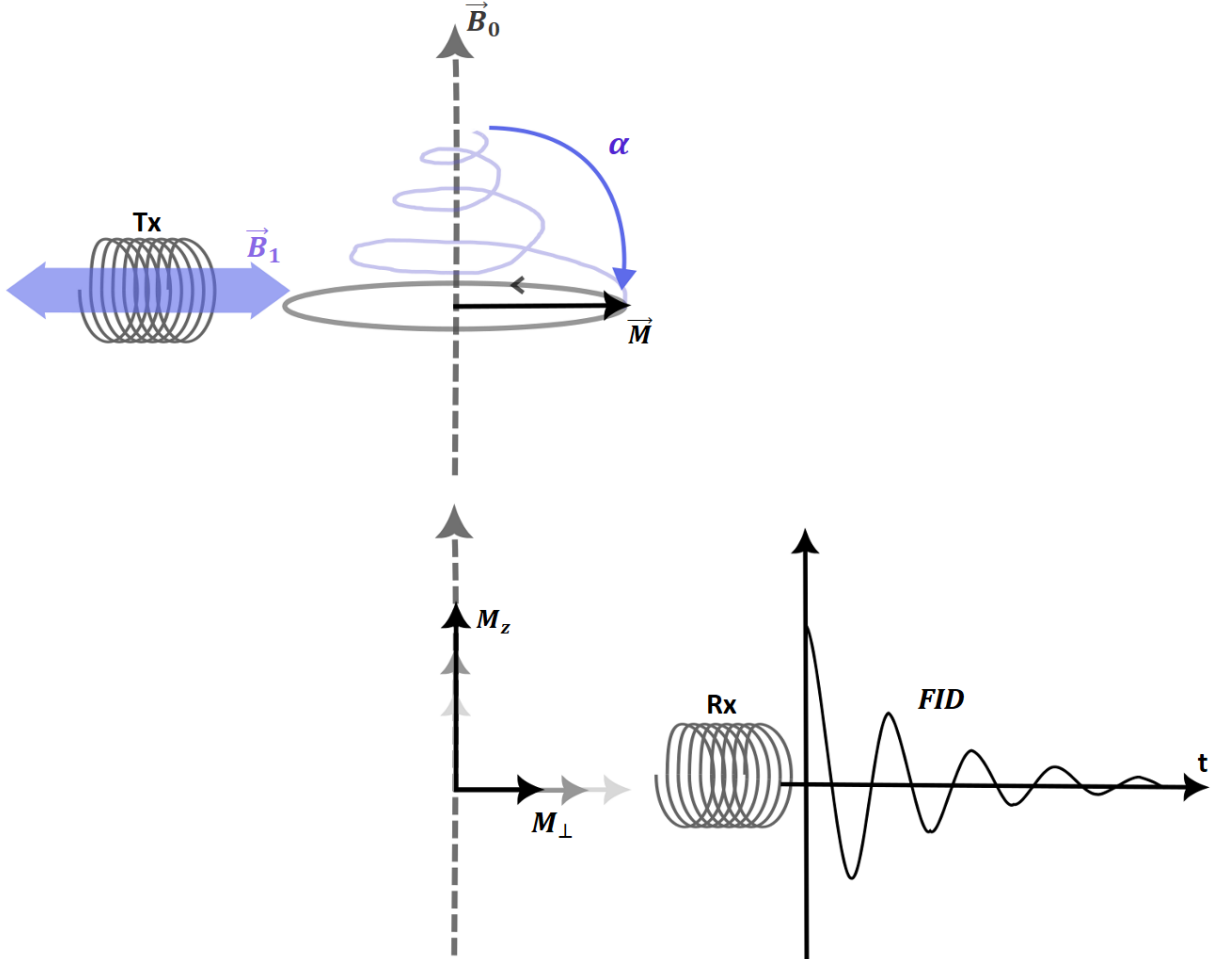


*Figure 2.2: A transmitter coil (Tx) generates RF pulses that produce a  $\vec{B}_1$  field that alternates at the  $\omega_0$  to move  $\vec{M}$  out of its equilibrium position at some flip angle  $\alpha$ . Then, as the longitudinal component  $M_z$  recovers and the transverse component  $M_{\perp}$  decays as the precessing spins move out of phase, the receiver coil (Rx) measures the induced current from the RF signal over time (FID).*

From Figure 2.2 we also see that the measured transverse signal, the Free Induction Decay (*FID*), starts at the highest magnitude at the moment  $\vec{M}$  is knocked into the transverse plane. It then oscillates at the Larmor frequency  $\omega_0$  of the measured sample while gradually decaying over time as the spins (that  $\vec{M}$  represents) move out of phase with each other. The "dephasing" of  $M_{\perp}$  and the vertical recovery of  $M_z$  does not happen at the same time, which is why T1- and T2-weighted images have different contrast relations between tissues. The measured frequency of the FID is an estimate of the Larmor frequency of the sample material, but in MRI acquisitions the signal will be more complex and represent many different frequencies.

### 2.1.3 Slice selection

To be able to distinguish MR signal frequencies at different positions  $z$  relative to isocenter, a position dependent Larmor frequency is introduced via a linear gradient

to slightly modulate the static  $B_0$  field:

$$\omega_0(z) = \gamma(B_0 + G_z \cdot z), \quad (2.2)$$

where  $G_z$  is the gradient strength and acts as the slope of the linear function. Without these z-gradients, the Larmor frequency would be the same across the entire sample after excitation and our receiver coils would measure signal from the entire sample. With the z-gradients active, we can selectively excite the sample by applying an RF pulse with a bandwidth  $\Delta\omega_0$  that excites a slice with thickness  $\Delta z$ . This is illustrated in Figure 2.3 with an LV as the sample.

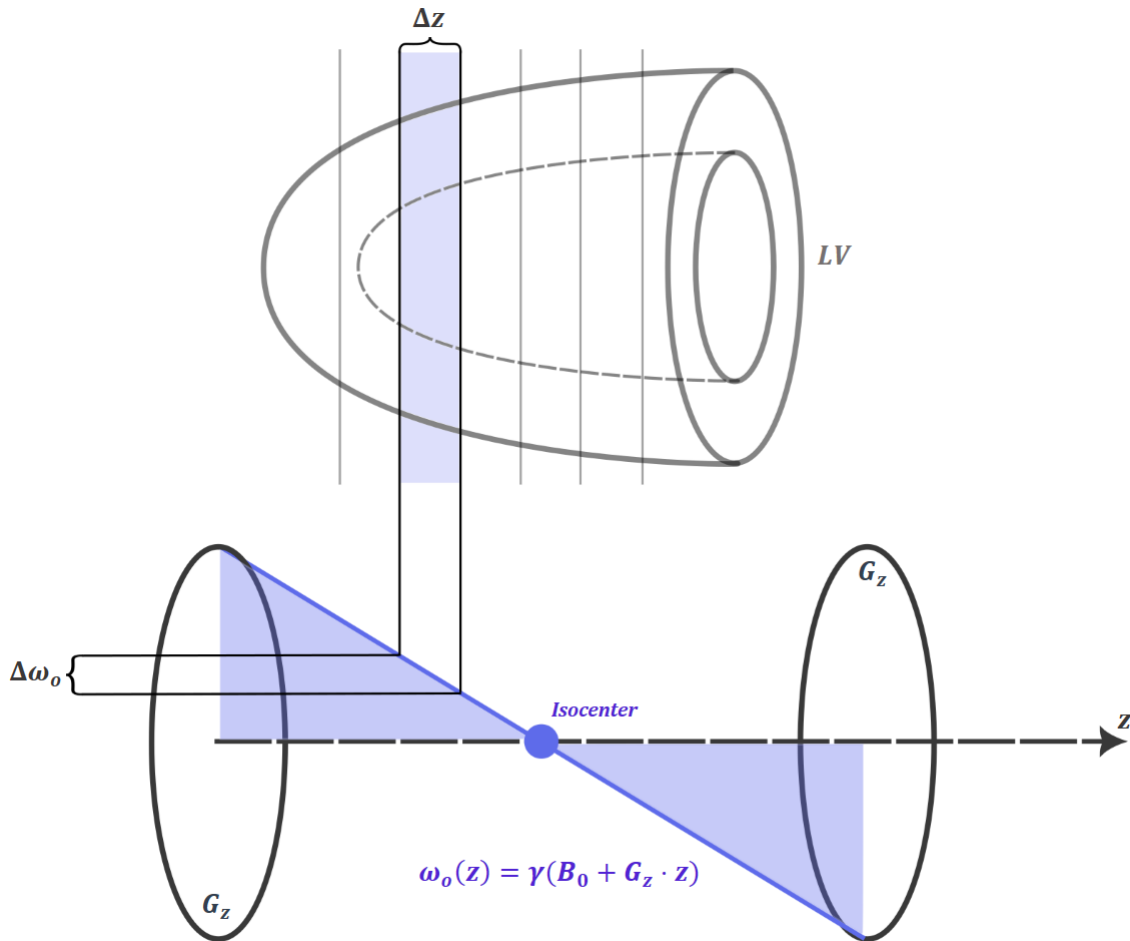


Figure 2.3: Two gradient coils ( $G_z$ ) of opposite polarity creating a linear variation of  $B_0$  along the  $z$ -direction, and  $\omega_0$  as defined in Equation 2.2. The RF bandwidth determines a range of Larmor frequencies  $\Delta\omega_0$  that it excites, determining the slice position from the isocenter and the slice thickness  $\Delta z$ . The isocenter ( $z = 0$ ) is defined, by convention, to be in the middle of the MRI magnet.

The profile of the selected slice is determined by the RF pulse design. A conventional choice is to use a sinc pulse. This function can be designed to contain a range of frequencies, which can be shown in a frequency spectra appearing like a block function (via Fourier transform), as seen in Figure 2.4. The width of this "block" corresponds to the bandwidth  $\Delta\omega_0$ , but thanks to the linear z-gradient it also represents the slice

(with thickness  $\Delta z$ ) along the z-axis with corresponding Larmor frequencies  $\omega_0(z)$ . The duration of the sinc pulse is an optimization issue, as a longer pulse more precisely represents the different frequencies and creates a better slice profile with no border artifacts.

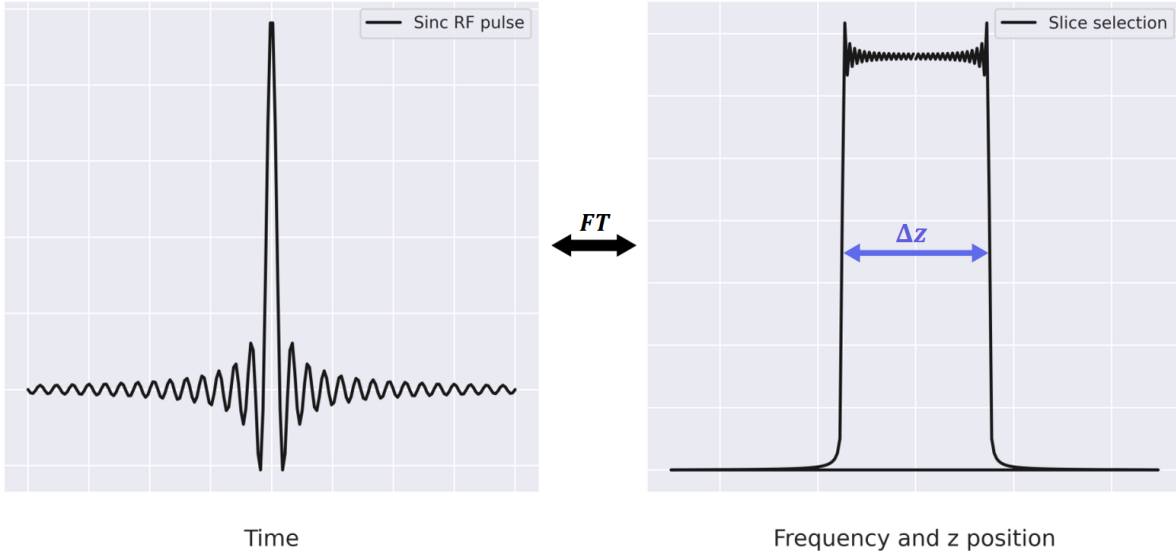


Figure 2.4: A sinc function RF pulse of some finite duration containing a range of frequencies, and a Fourier transform of that pulse representing the slice profile. This function both describes the signal from the composite frequencies in the sinc function (frequency spectra), but also the slice thickness  $\Delta z$  covering the corresponding range of Larmor frequencies  $\omega_0$  in the sample.

## 2.1.4 k-space

Now that we have used the z-gradients in combination with the RF pulse to selectively excite one slice in our sample, we need to apply gradients in the x- and y-direction to modulating the phase and frequency to generate signals that can be reconstructed into an MR image. By introducing linear variations in Larmor frequency (for every magnetization vector  $\vec{M}$  in every voxel) in the x and y directions, the MR signal amplitude measured from the slice will vary depending on the total phase agreement. Spins that are in phase will generate signals boosted by constructive interference, while a sample with spins completely out of phase will cancel each other's signals out due to destructive interference.

This kind of measurement is quite abstract and contains many parts, so we need an intuitive way of visualizing and storing this information to interpret it and also to reconstruct an image from the data. The acquired raw MR data can be represented by a "k-space" plot as seen in Figure 2.5, and be converted to an image via Fourier transform. The k-space distribution is essentially a frequency spectra of the entire signal, like we saw in Figure 2.4 for the sinc pulse, but with an extra dimension. The highest signal concentration is seen in and around  $k_x, k_y = 0$  where the spin phases are more similar and the signal is boosted by constructive interference.

The signal contents in the k-space are components of spatial frequencies. These fre-

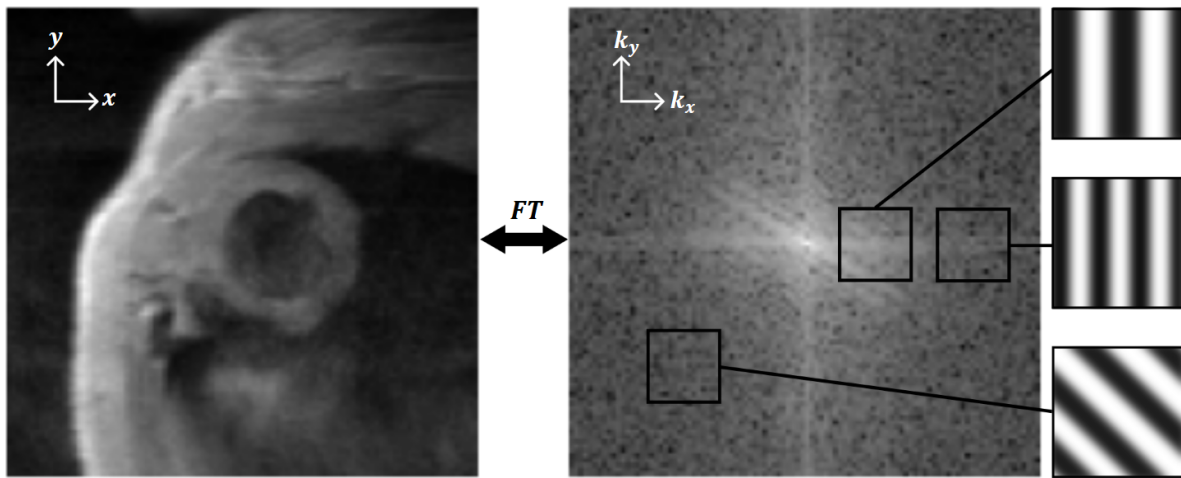


Figure 2.5: An image with pixel elements in  $x$  and  $y$  positions, and a corresponding  $k$ -space representation with the same dimensions calculated via Fourier transform. The zero frequency component ( $k_x, k_y = 0$ ) has been shifted to the middle of the image. Examples of spatial frequencies from the  $k$ -space distribution are marked and illustrated as line-pairs.

quencies can be represented as a sequence of black and white lines called "line-pairs". Figure 2.5 illustrates how the higher frequency components from the  $k$ -space distribution give thinner and more frequent lines, and that the spatial frequencies have an inherent spatial orientation depending on the  $k_x, k_y$  components. Low frequency signal (closer to the origin in the middle) correlates to image contrast and larger shapes in the image, while the high frequency information further from the origin contains the fine image details and sharp contours.

The  $k$ -space magnitude for each spatial frequency says something of its presence in the *entire* image, and does not represent some quality of a specific pixel coordinate in the reconstructed image. Instead, we can think of the image as a weighted sum of all the line-pairs, weighted by the magnitude of the corresponding spatial frequency.

## 2.1.5 Pulse sequences

So how do we sample all of this signal? To produce an image with high quality, we need to sample enough of the  $k$ -space to acquire both low- and high spatial frequency information. Acquisition time of the image is a limitation, however, so different pulse sequences have been developed for different uses that minimizes time spent but still samples a sufficient amount of  $k$ -space. These sequences are essentially a timeline detailing when the image sample is magnetized by an RF pulse and which gradient is active at which point.

For a constant gradient strength  $G_{x,y}$  and duration  $T$ , their product decides the points in  $k$ -space we can sample. We can think of using the gradients to "travel" through  $k$ -space in the  $k_x$  and  $k_y$  direction:

$$k_{x,y}(T) = \frac{\lambda}{2\pi} \int_0^T G_{x,y}(t) dt = \frac{\lambda}{2\pi} G_{x,y} T. \quad (2.3)$$

This tells us that to sample higher frequency signals we need to apply either stronger gradients or apply them for a longer duration. Figure 2.6 shows how a pulse sequence for a Gradient Echo (GRE) sequence for sampling one line in k-space looks like. Reading the timeline from left to right, we see that the z-gradient ( $G_z$ ) is first used to create the linear gradient as defined in Equation 2.2, which lets us apply an RF pulse to select and excite a slice at some flip angle  $\alpha$  where we want to acquire an image. Following this, we see that another z-gradient is applied with opposite polarity designed to refocus the phase dispersion in the z-direction after the RF pulse to prevent unnecessary signal loss.

Afterwards, the orientation of the k-space ( $k_x, k_y$ ) to sample one line in the frequency encoding direction is performed in 3 steps. In the first step we wish to move to the leftmost end of the line we are sampling, done by moving backwards in the  $k_x$  direction (negative  $G_x$  gradient) and upward or downward in the  $k_y$  direction depending on which readout line the sequence is instructing ( $G_y$  illustrated to have multiple possible directions in Figure 2.6). In step 2, the only active part of our sequence is the  $G_x$  gradient, which "moves" us from the left to the right in k-space while reading out signal. The "gradient echo" occurs when we cross  $k_x = 0$ , which is where the spins in our sample will be the most in phase and produce a more resonant output (this is why the k-space image has higher values along  $k_x$  and  $k_y$  and a peak in the middle). In step 3 we rewind back to the start point in the middle to prepare for the next repetition where a new line will be sampled. The x-gradient is identical to the one used in step 1, while the y-gradient has opposite polarity to move back in the phase direction.

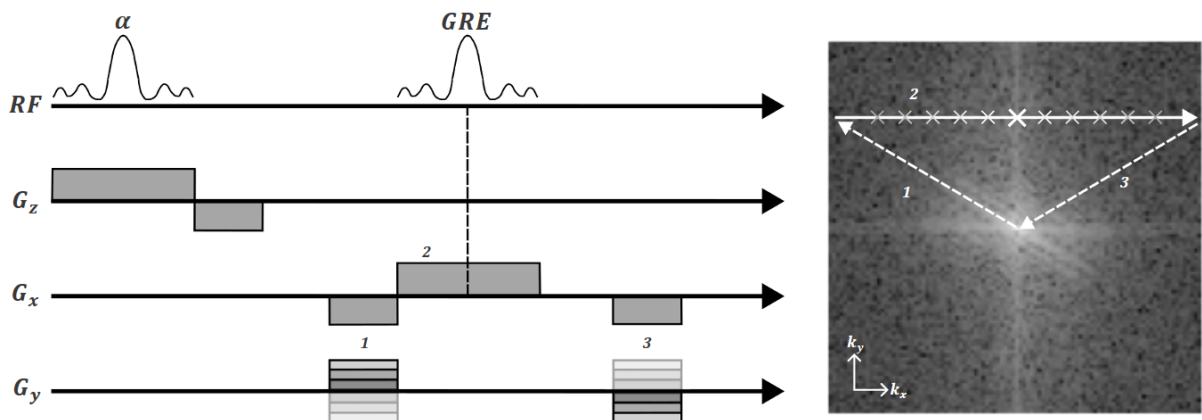


*Figure 2.6: A simple GRE pulse sequence diagram, with a k-space plot to demonstrate dephasing (step 1) and readout of one horizontal line along the frequency encoding direction  $k_x$  (step 2) and then rewinding back to  $k_x = 0, k_y = 0$  (step 3) before the next repetition. Timelines for the frequency encoding gradient ( $G_x$ ), the phase encoding gradient ( $G_y$ ) and the slice selecting gradient ( $G_z$ ) are illustrated. The gradient echo is illustrated at  $k_x = 0$  where all spins in the sample are in phase in the frequency encoding direction. The RF timeline visualizes the excitation RF pulse and the measured gradient echo at the readout section. A discrete amount of measurements are made during readout, marked with "X" in the diagram.*

To fully collect the spatial frequency information we need to produce an image, this sequence is repeated to sample the k-space along a series of horizontal lines. An RF pulse and the gradient sequence is required for each line. The time between each RF pulse is called the "repetition time" (TR) and the time from the RF pulse to the gradient echo is called the "echo time" (TE). These are important parameters in optimizing pulse sequences.

The figures presented in this chapter assume perfect gradients, as seen in Figure 2.6 where they are illustrated as perfectly square blocks that spontaneously activate and deactivate. In practice, the gradients require a slight time interval to reach the desired amplitude.

## 2.1.6 Motion encoded MRI

We have thus far assumed that all spins are stationary, but they can of course move during acquisition. Examples of this are the flow of blood, or the periodic motions of the heart. This section will discuss how pulse sequences can be designed to compensate for this motion, or alternatively, to measure signal specifically describing the motion. The latter is of course essential for the data we need in this thesis to describe the motion of the heart.

If a spin moves from an initial position  $x_0$  at an initial velocity  $v_0$  and initial acceleration  $a_0$  while a gradient  $G(t)$  is applied from time point  $t_1$  to  $t_2$ , it will accumulate additional phase as described by this function:

$$\begin{aligned}\Delta\phi_{t_1 \rightarrow t_2} &\approx \gamma \left( x_0 \int_{t_1}^{t_2} G(t) dt + v_0 \int_{t_1}^{t_2} G(t) t dt + \frac{a_0}{2} \int_{t_1}^{t_2} G(t) t^2 dt \right) \\ &= \gamma \left( x_0 m_0 + v_0 m_1 + \frac{a_0}{2} m_2 \right),\end{aligned}\quad (2.4)$$

where  $\gamma$  is the gyromagnetic ratio and  $m_0$ ,  $m_1$  and  $m_2$  are "gradient moments"; the gradient integrals related to position, velocity and acceleration that affect the spin. This equation assumes no higher order motion and assumes a rotating frame of reference with rotational frequency  $\omega_0$ , meaning that this equation only describes how the spins are affected by the gradients and not the constant  $B_0$  field.

Equation 2.4 now lets us predict how the phase of a spin is affected by position, velocity and acceleration separately. A common application of this is to design motion compensating gradients that ensure that the gradient moments associated with velocity and acceleration ( $m_1$ ,  $m_2$ ) are zero after the gradient sequence. This "gradient nulling" ensures that phase that was gained from the movement of the spin does not produce a distinguishable signal.

When designing a PC-MRI sequence, we do the opposite and design gradients that null the phase contribution from stationary spins ( $m_0$ ) but allow the other gradient moments

to contribute. This is done with a symmetric bipolar gradient with a positive and negative "lobe" as shown in Figure 2.7. Here we see that for a spin with no motion, the change in phase  $\Delta\phi$  is reverted by the end of the gradient. For spins with constant velocity and acceleration, their magnetic moments are non-zero after the gradient sequence. We can also tell from the figure that the phase incoherence is higher for constant acceleration, so the signal measured from spins with constant velocity would be stronger in this sequence.

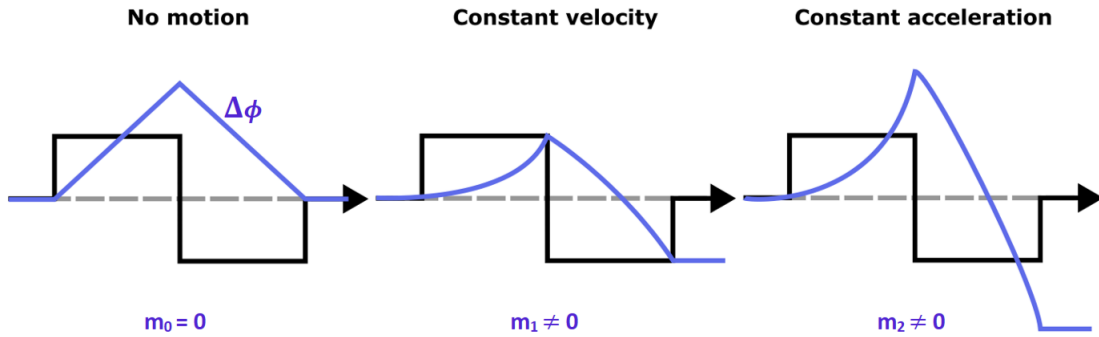


*Figure 2.7: The effect of a symmetric, bipolar gradient (black lines) on the gradient moments of spins with no motion in the lab frame, constant velocity and constant acceleration. This demonstrates motion encoding of the signal, where only the gradient moments  $m_1$  and  $m_2$  are non-zero.*

Difference in phase between spins can be expressed by the range  $\Delta\phi \in [-\pi, \pi]$ . This means that we will get an "aliasing" effect for  $\Delta\phi$  outside the range; if we for example have a spin with  $\Delta\phi = 1.2\pi$  it would loop around and register as  $-0.8\pi$ . To gain phase outside the range, spins would have to move with a high velocity, move through a strong gradient or move through a gradient that is applied for a long duration. These parameters introduce a limit to the minimum and maximum magnitude of velocity that a PC-MRI sequence can measure without aliasing occurring (8):

$$v_0 = \frac{\Delta\phi}{\gamma \cdot \Delta m_1}, \quad (2.5)$$

where  $\Delta m_1$  is the difference between  $m_1$  from two acquisitions that are identical except for opposite bipolar gradients. We remember that these gradient integral includes information about the gradient strength and duration. The minimum/maximun limits are calculated by setting  $\Delta\phi = \pm\pi$ . This limit is called the "VENC" (velocity encoding), and by changing the gradient strength and duration we can design a sequence that allows for specific peak velocities. If we are interested in imaging blood flow we need to allow for high velocities, while the movement of the heart muscle is comparatively slow.

In a PC-MRI acquisition we are interested in observing how internal geometry changes over time, and need both high spatial and temporal resolution. This requires fast and strong gradients, which introduces a source of noise to the data in the form of velocity offsets. One reason for this is that the  $B_0$  main magnetic field "resists" any change being made to it by the gradients by inducing opposing currents in the gradient coils,

as a consequence of Lenz' law. These "eddy currents" create spatial irregularities in the phase dispersion at a rate proportional to gradient strength, which introduces noise to the velocity fields (17). Different approaches to eddy current compensation (ECC) have been developed, and it is a widely discussed topic in PC-MRI optimization.

The PC-MRI application we are interested in is Tissue phase mapping (TPM), which is designed specifically for measuring myocardial motion (18). We will get into the details of the TPM acquisitions later in the methods chapter.

## 2.2 Heart physiology

To interpret the data we will be using and the results we get, it is essential to have a fundamental understanding of the heart. We will take a quick dive into anatomy, physiology as well as a quick look into how the heart deforms during the cardiac cycle and what these can tell us about regional myocardial function and HF.

### 2.2.1 Heart anatomy and the cardiac cycle

Mammal hearts have four chambers that hold and transport blood at different points in the cardiac cycle. The right atrium (RA) and right ventricle (RV) pump oxygen-poor blood to the lungs, and the left atrium (LA) and left ventricle (LV) pump oxygenated blood out into the body (19). The heart interior with labelled chambers is illustrated in Figure 2.8.

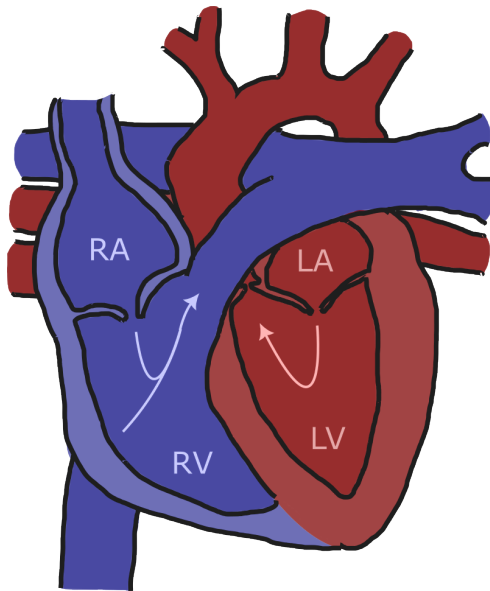


*Figure 2.8: Illustrated heart interior with labelled chambers, blue indicating de-oxygenated blood and red oxygenated. Direction of blood flow through the chambers indicated with arrows. Atria and ventricles are separated by pulmonary valves. The chamber walls are the myocardium.*

The chamber walls consist of muscle tissue called the "myocardium", which receives electrical signals that determine heart rate by triggering contracting motions that causes

the chambers to pump blood. These contracting and relaxing motions make the atrioventricular valves open and close periodically each cycle to regulate blood flow from the atria to the ventricles (19). The LV is the largest of the chambers and has the responsibility of pumping blood out into the entire body, which is the most important function of the heart. It has the thickest chamber walls and is relatively symmetrical and cone shaped. These simple geometric traits make it optimal for geometrical modelling and analysis.

Going through the various phases of the cardiac cycle, we know when and how the LV myocardium should contract and relax in detail (20). The phase of the the cardiac cycle where the LV contracts is called the "systole". While contracting, the LV myocardium thickens in the radial direction and shortens in the circumferential direction to shrink the chamber volume and pump the blood contents out into the body. The wall thickens and the circumference and height is shortened as illustrated in Figure 2.9. At the start of the diastolic phase, the muscle tissue relaxes and the LV moves back to its initial dimensions, marking the beginning of a new cardiac cycle.

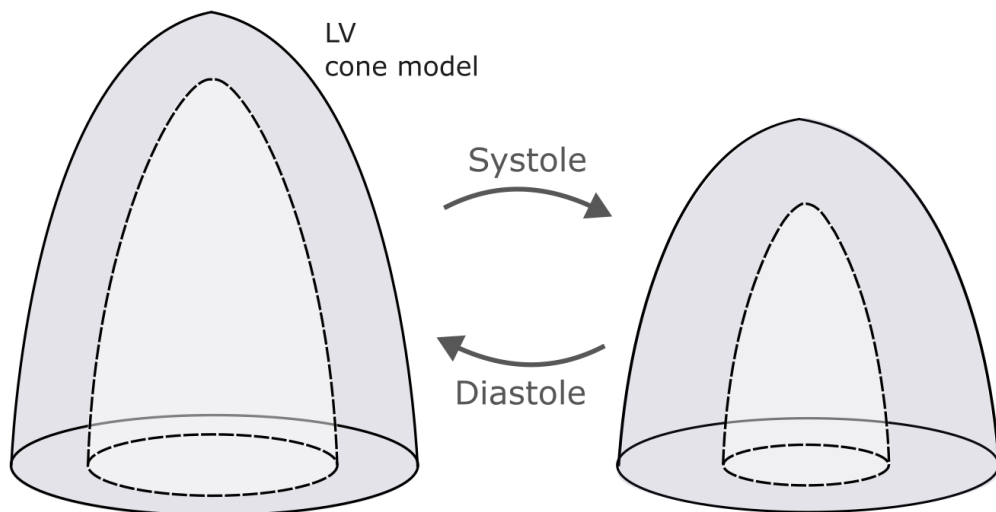


*Figure 2.9: Illustration of the LV simplified as a cone, demonstrating how the myocardium thickens radially as well as reducing its circumference and length when contracting during systole to minimize the interior LV chamber volume. Relaxing the muscle during the diastole returns the LV to its initial dimensions and the beginning of the cardiac cycle.*

## 2.2.2 Myocardial infarction

Reduced blood flow to the myocardium, due to blockage of the atria delivering blood to the muscle tissue or other reasons, can result in a myocardial infarction (MI). The tissue that lacks blood can get permanently damaged or die, even if blood flow is restored later. This can reduce or in the worst case completely disrupt the blood flow from the heart chambers to the rest of the body (5).

Infarcted tissue can be detected in CMR images via Late Gadolinium Enhancement (LGE), as demonstrated in Figure 2.10. Gadolinium contrast accumulates in infarcted

tissue due to slow washout compared to the functional myocardium, creating a highlighting effect by causing a shortening of T1-decay. The highlight is therefore visible in T1 weighted images (21). The figure also demonstrates that the brighter section of the LV is thinner, which is another way we can identify infarction.

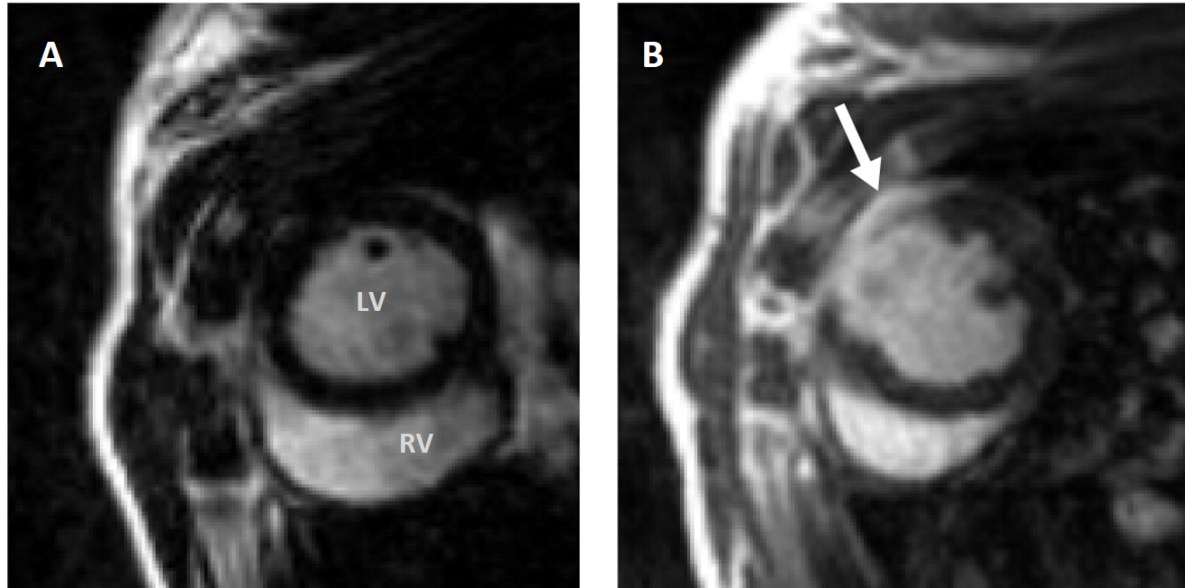


*Figure 2.10: A: Sample LGE image of a Sham heart, with black LV myocardium that indicates viable muscle tissue. B: Sample LGE image of an MI heart, with highlighted infarct tissue in the LV myocardium.*

Another known characteristic of the infarct tissue that results from MI is that it becomes "stiff" and loses its ability to actively (22). The heart responds to this loss of function by adjusting its mechanical properties to maintain the blood pumping capabilities of its chambers, which relates to a process called "cardiac remodelling". Despite being an attempt by the body to regain function and control, the effects of cardiac remodelling themselves can cause hurtful symptoms and are clear indicators of myocardial dysfunction (23). These details about the mechanical dysfunction of the myocardium can be revealed by analysis of regional LV deformation, which is where myocardial strain as a functional parameter comes in.

## 2.3 Myocardial strain and strain rate

The simple, one-dimensional definition of strain is that it is a measurement of the relative deformation  $\Delta L$  of the initial length  $L$  of an object:

$$\varepsilon = \frac{\Delta L}{L}. \quad (2.6)$$

This is the Lagrangian, or "material", definition of strain (8) and is illustrated in Figure 2.11 with a cylinder that is stretched and compressed by a force  $\vec{F}$  as examples of positive and negative value strain. Strain values are expressed as a percentage % change

from an initial length. What is also apparent in this figure is that the cylinders don't just deform vertically despite being affected by a vertical force, but they also deform horizontally. This illustrates the deformation of an incompressible material, which we assume muscle tissue is (24), meaning that it needs to deform in this way to conserve its mass. It should not, for example, expand in all directions or be compressed in all directions. This principle of conservation of mass in multi-dimensional deformation will be relevant again later, as we are specifically interested in deformation in two- and three-dimensional velocity fields. Strain *rate* refers to the rate of which the deformations happens, expressed with the unit  $s^{-1}$ .

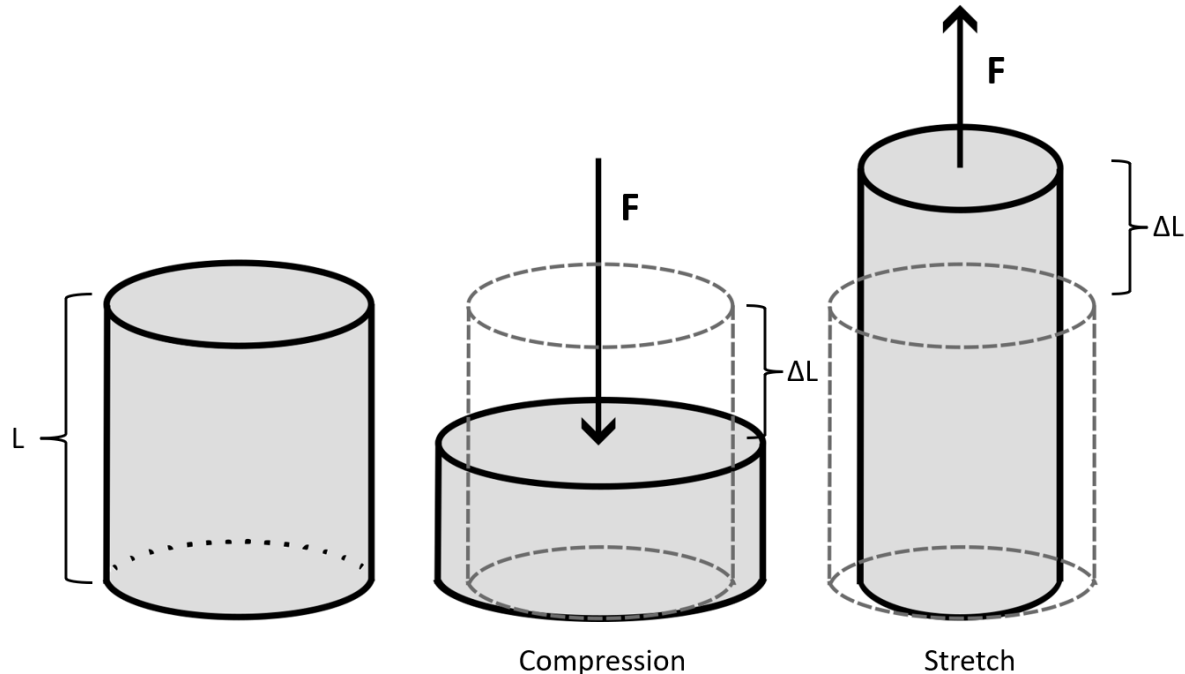


*Figure 2.11: Demonstration of the one-dimensional strain  $\varepsilon$  of a cylinder of initial length  $L$ , made of an incompressible material. When the cylinder is compressed (negative  $\Delta L$ ) by a vertical force  $\vec{F}$  it is affected by negative strain in that direction, when it is stretched (positive  $\Delta L$ ) it is affected by positive strain. The horizontal deformation of the cylinder hints at strain in two/three dimensions and conservation of mass in an incompressible material.*

(about the other methods of strain measurements?) We introduced some established imaging methods within CMR and echocardiography that are used to measure myocardial strain. The algorithms used to read out the strain information from these methods ... (25)

Figure 2.12 illustrates two different ways of calculating strain from TPM velocity fields in the myocardium. Using numerical integration to simulate the path of a point in the muscle tissue throughout the cardiac cycle, you can calculate displacement from an initial position over time. Spatial derivation of the displacement gives strain over time (8).

The other alternative, the method used in this thesis, involves first applying spatial derivation to the velocity field to calculate strain rate, and then integrate in time to get

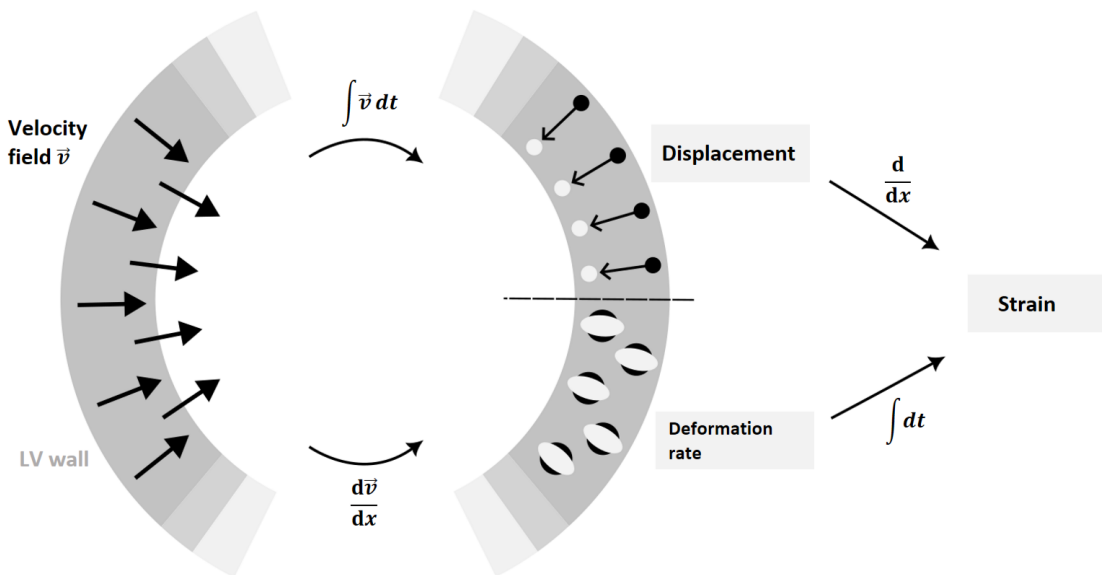


*Figure 2.12: Illustration of two different methods of calculating strain from a velocity field, exemplified in LV segments here with a velocity field describing movement of the myocardium toward the LV center. Motion tracking by integrating velocity data in time ( $\int \vec{v} dt$ ) describes displacement of points from an initial position. Spatial velocity gradients ( $d\vec{v}/dx$ ) describes deformation rate in the velocity field, illustrated as circles being deformed (stretched and compressed) into elliptic shapes.*

strain. Spatial variation in velocities, how the tissue in one voxel moves in relation to its neighbors, describes local deformation. A mathematical method of calculating strain rate tensors from PC-MRI velocity data has been established, which we will refer to as the "Selskog method" based on the first author of the study (15). This method will be the mathematical cornerstone of our analysis, and the essential tensor equations will be introduced in the following paragraphs.

The strain rate tensor is calculated using gradients of all velocity components in all spatial axes in the relevant system of analysis. The n-dimensional velocity gradient tensor ( $n \times n$  Jacobian) is calculated like this:

$$L_{ij} = \frac{\partial u_i}{\partial x_j}, \quad (2.7)$$

where  $u_i$ ,  $i = 1, \dots, n$  are the velocity components in the  $x_j$  direction  $j = 1, \dots, n$ . If we calculate such a gradient tensor  $L_{ij}$  at some position in an n-dimensional velocity field, it essentially contains all gradient information relevant to this position. Or in other words; it tells us something about local variation in velocity along all spatial axes and all velocity components.

From the velocity gradient tensor  $L_{ij}$ , the strain rate tensor can be calculated like this:

$$D_{ij} = \frac{1}{2} \left( \frac{\partial u_i}{\partial x_j} + \frac{\partial u_j}{\partial x_i} \right) = \frac{1}{2} (L_{ij} + L_{ij}^T). \quad (2.8)$$

The eigenvalues  $\lambda_i$  and eigenvectors  $\vec{v}_i$  of  $D_{ij}$  are the principal values and the principal directions of strain-rate in the myocardium, as shown in Figure 2.13 for two and three dimensions. The sign of the eigenvalue distinguishes between stretching (positive) and compression (negative) in the direction of the corresponding eigenvector.

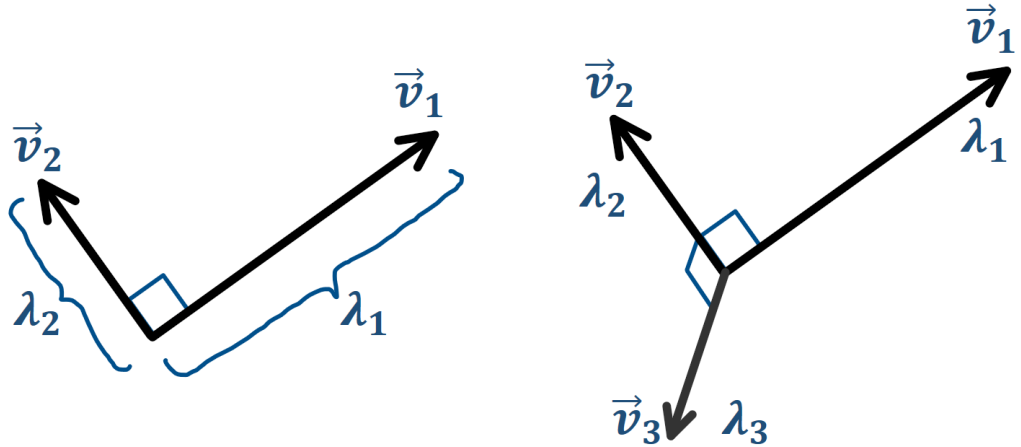


Figure 2.13: Orthogonal eigenvectors  $\vec{v}_i$  for a two-dimensional and three-dimensional strain rate tensor  $D_{ij}$  ( $n = 2, n = 3$ ), where the vector magnitudes are represented by eigenvalues  $|\lambda_i|$ .

The invariant  $I$  represents the total magnitude of strain rate in an  $n$ -dimensional strain rate tensor, irrespective of direction:

$$I = \sum_{i=1}^n \lambda_i^2. \quad (2.9)$$



# **Chapter 3**

## **Material and Methods**

The different methods used in the thesis are described in this chapter. Section 3.1 covers the TPM data that was produced and provided by the MR group at IEMR for use in my analysis. My own contributions are described in the two following sections. Section 3.2 goes into detail of how I implemented established theory into an original Python framework that produces tensor fields from TPM data that describe the deformation of the myocardium, and produces plots and measurements of functional parameters. Section 3.3 describes how the framework was applied to a larger scale statistical analysis of regional LV dysfunction, and the statistical methods used. Additionally, some of the TPM datasets were segmented personally by me, using a MATLAB script borrowed from the MR group, in order to have more available data for the analysis. A supplementary GitHub repository contains all Python scripts developed for this thesis: [https://github.com/lassetotl/Thesis\\_CMRIEMR](https://github.com/lassetotl/Thesis_CMRIEMR).

### **3.1 Data overview**

Here we present a short overview of the TPM data that this thesis is based on. All data used in the thesis was produced previously by the MR group at IEMR in 2017-2018 in their "LCZ" study, and the group has also used a similar MI rat model in a study before (26). In this study, the rats were operated and scanned in a similar way to how the LCZ data were produced. Because of this, the following overview is presented in a similarly to how it is presented in the study.

#### **3.1.1 Rat MI model**

As a part of the larger "LCZ-study" performed at IEMR, male Wistar-Hannover rats ( $\approx 300$  g) that were approximately 6 weeks old were anesthetized (96% O<sub>2</sub>, and 4% isoflurane) and ventilated by endotracheal intubation using a Zoovent ventilator. Of the rats included in our analysis, LV MI was induced in 7 of them by proximal ligation of the left coronary artery during maintained anesthesia (98% O<sub>2</sub>, and 1.5-2.5% isoflurane). The placement of the ligation was deliberately varied to achieve variable infarct sizes. A Sham-operated control group consisting of 6 rats underwent the same proce-

dure with the exception of ligation. All experimental protocols were approved by the Norwegian National Animal Research Authority and performed in accordance with the European Directive 2010/63/EU and institutional guidelines (ID 3284).

### 3.1.2 MRI Acquisition

In time intervals after operation (1, 3, 10, 21 and 42 days), MRI experiments were performed on a 9.4T magnetic resonance system (Agilent Technologies, Inc) using hardware dedicated to rat cardiac imaging. From our selected group, we chose 23 MI datasets and 27 Sham datasets. For analysis requiring single slices, no exclusions were made. For analysis requiring all slices of the LV, some datasets were excluded due to missing slices or slices with distorted velocity fields that could not be interpreted by the MATLAB segmentation script (20 MI and 21 Sham datasets remaining in this case).

Anesthesia was induced in a chamber using a mixture of O<sub>2</sub> and  $\approx$  4.0% isoflurane and maintained during acquisition in freely breathing animals using O<sub>2</sub> and  $\approx$  1.5% isoflurane. Throughout the examination, ECG, respiration, and body temperature were monitored, the latter maintained at 37.0°C by heated air. LV short-axis (SHAX) imaging planes were identified from untriggered scout images, and all subsequent acquisitions triggered at the peak of the R wave and gated for respiratory motion. In all data sets, the temporal resolution was equal to the repetition time.

The TPM MR sequence used an RF-spoiled black blood gradient echo cine sequence using 9-point velocity-encoding (27) and rotating field of view (28). Several SHAX slices were acquired to cover the entire LV. All slices were parallel and shared a common center normal. The TPM time series also covered >100% of the heart cycle. Imaging parameters were echo time TE=2.22 to 2.26 ms, repetition time TR=2.93 to 3.21 ms, field of view FOV=50x50 mm, matrix=128x128, slice thickness  $\Delta z$ =1.5 mm, flip angle=7°, VENC=13.9 cm/s, signal averaging=2x using rotating field of view (28), total acquisition time=45 to 50 minutes.

In each TPM slice, the myocardium was segmented using a semiautomatic method that requires the user to delineate the endo- and epicardium at end systole and end diastole. The masks were then automatically propagated throughout the cardiac cycle based on the underlying velocity fields. The myocardial masks were divided into 36 equal sectors defined by the LV center. The sectors that were determined to include infarcted tissue during segmenting, based on LGE MRI images, are noted in the metadata of each dataset to localize fibrosis in the analysis.

## 3.2 Strain rate tensor analysis framework

This section discusses the process of how our Python framework uses the SHAX velocity fields from the TPM data to calculate strain rate tensors in the myocardium, visualize them and analyse LV strain rate and strain globally and regionally in the radial, circumferential and longitudinal directions using 2D and 3D strain rate tensors. The framework will also be able to use the tensors to assess the direction of strain rate unrestricted by the conventional axes in heart geometry.

### 3.2.1 LV segmentation models

To be able to perform regional deformation analysis of the LV, we need to establish models that divide our MRI data into segments that can be measured separately to study variation between them. Figure 3.1A shows a segmentation model where the LV is divided to study regional variation within a single basal slice. The details of how the slice is segmented is discussed later in section 3.2.8.

Figure 3.1B shows a second segmentation model consisting of a series of slices covering most of the LV, divided into a basal and apical half. It has been shown that the effects of cardiovascular disease can affect LV mechanics differently at different levels (10). The intention with our model is to also look at three-dimensional regional variation of our measured parameters. If the processed heart data contains an odd number of slices, we have chosen to include the middle slice in both the basal and apical half.

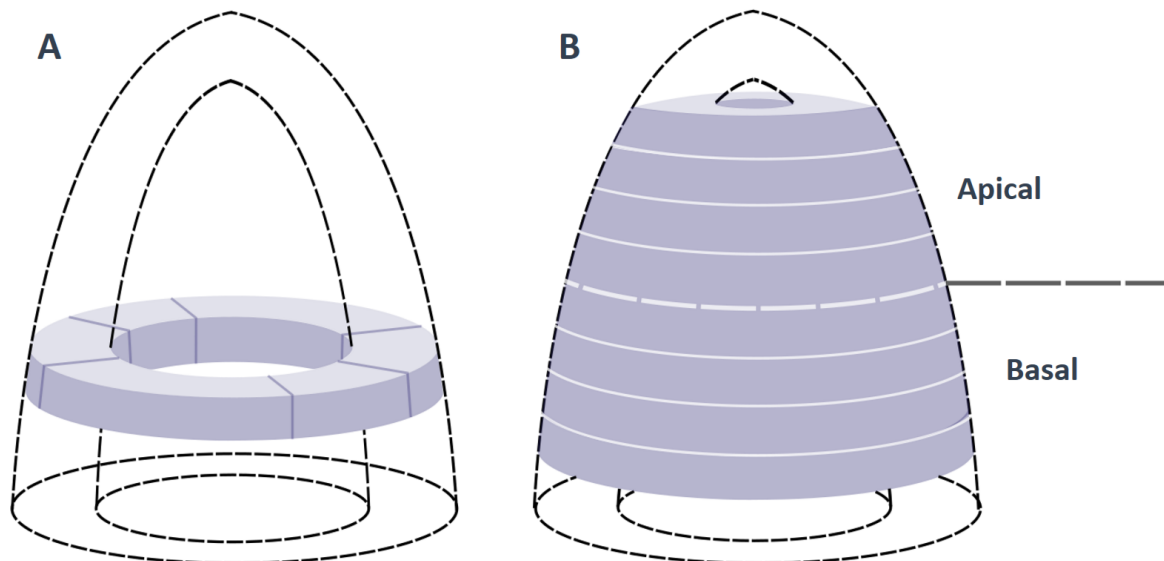


*Figure 3.1: The LV segmentation models used in this thesis. A: Model that studies regional variation within one basal slice by segmenting it into separate sections. B: Model that studies regional variation in a series of slices that covers most of the LV. The stack is split in the middle into an apical and a basal half.*

The "slices" in these models are in practice masks of the voxels in the TPM scans that contain the LV myocardium, producing quite circular shapes for images in the SHAX plane. These masks cover the LV myocardium, which contains velocity fields describing the muscle tissue motion we will analyze.

For our LV models we assume cylindrical geometry (29). This affects how the LV geometry and the principal directions of motion are defined. In conventional analysis of myocardial strain, measurements are made in three directions: the radial direction describing deformation perpendicular to the LV wall, the circumferential direction (perpendicular to radial direction within the xy-plane) describing deformation along the circumference and the longitudinal direction (perpendicular to xy-plane) describing deformation along the LV height. The definitions of these parameters in a cylindrical LV model are illustrated in Figure 3.2. Also demonstrated in this figure is that whenever

we refer to an "LV center", we refer to a local center within the relevant LV slice and never the center of the entire sequence of slices.

We will come back to the specific definitions of these axes later in this chapter when discussing implementation and interpretation of the strain rate tensors, but first we need to establish how the tensors are produced.

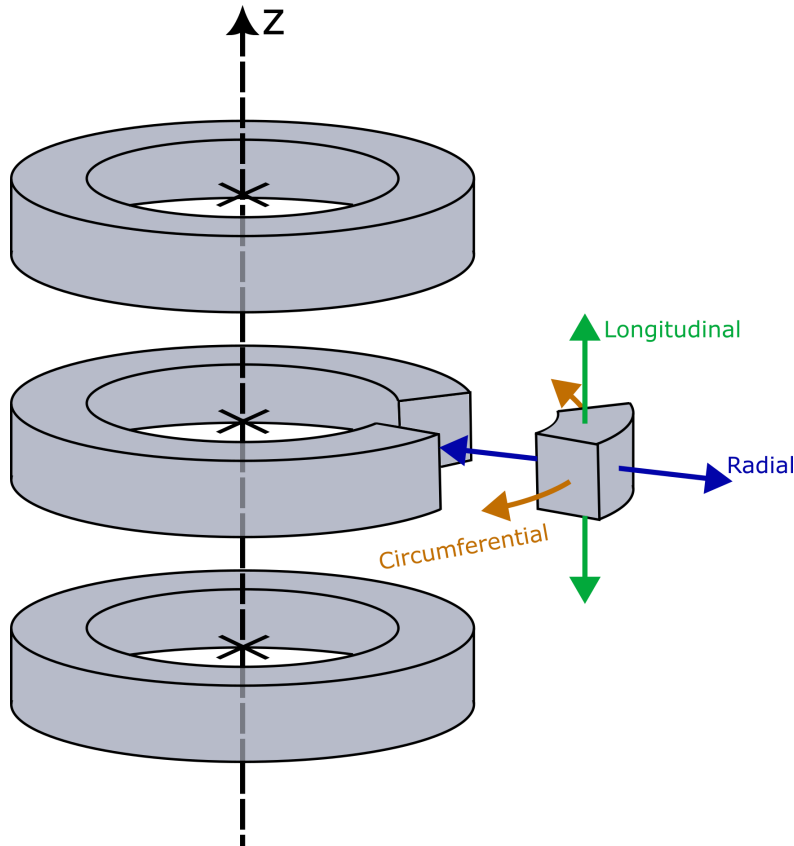


*Figure 3.2: Definition of radial, circumferential and longitudinal axes in a slice element in a cylindrical LV model consisting of slices arranged along the longitudinal axis. The radial direction is defined from the center of its corresponding LV slice (marked with "X"), the other axes are perpendicular. Each donut-shaped slice represents masks in the SHAX xy-plane containing LV myocardium.*

### 3.2.2 The velocity field

The TPM data is stored as a large MATLAB structure containing many different fields and parameters, which is imported to Python as a large dictionary structure.

Relevant to the framework we are developing, we have time dependent velocity fields representing cardiac motion, magnitude fields that represent proton density and relaxation dynamics. The structure also contains a binary mask matrix, designed during processing, with the same dimensions as the image with value 0 in voxels determined to be outside the myocardium and value 1 inside. Relevant static parameters are infarct sectors for MI hearts with visible infarction, slice position  $pss0$  relative to the gantry isocenter and the time points at end systole  $T_{es}$  and end diastole  $T_{ed}$ .

For our analysis, only tissue in the LV is relevant and we have to exclude noisy signal

from the movement of blood. This can be achieved by applying the binary mask. The velocity field inside the myocardium is also affected by noise, so we need to smooth the data to compensate for this. For this we can apply the following smoothing function to our velocity field (15):

$$u_{i,smooth} = \frac{(u_i \cdot c) * g}{c * g}, \quad (3.1)$$

where  $u_i$  is a velocity field for a spatial component  $i$ , and  $g$  is a 3D Gaussian function with a standard deviation  $\sigma = 2$ . Convolution is denoted with a "\*". The "c" is defined as a "certainty" matrix, calculated by normalizing the magnitude field to have values in the range  $c_k \in [0, 1]$  for a voxel  $k$ . The intention with the certainty values is to suppress velocity signal from the blood, as it produces lower magnitude values than soft tissue, before smoothing with the Gaussian application function. The "black blood" sequence used to acquire the TPM data further ensures that voxels with blood signal give low certainty values and lesser effect on gradient calculations later.

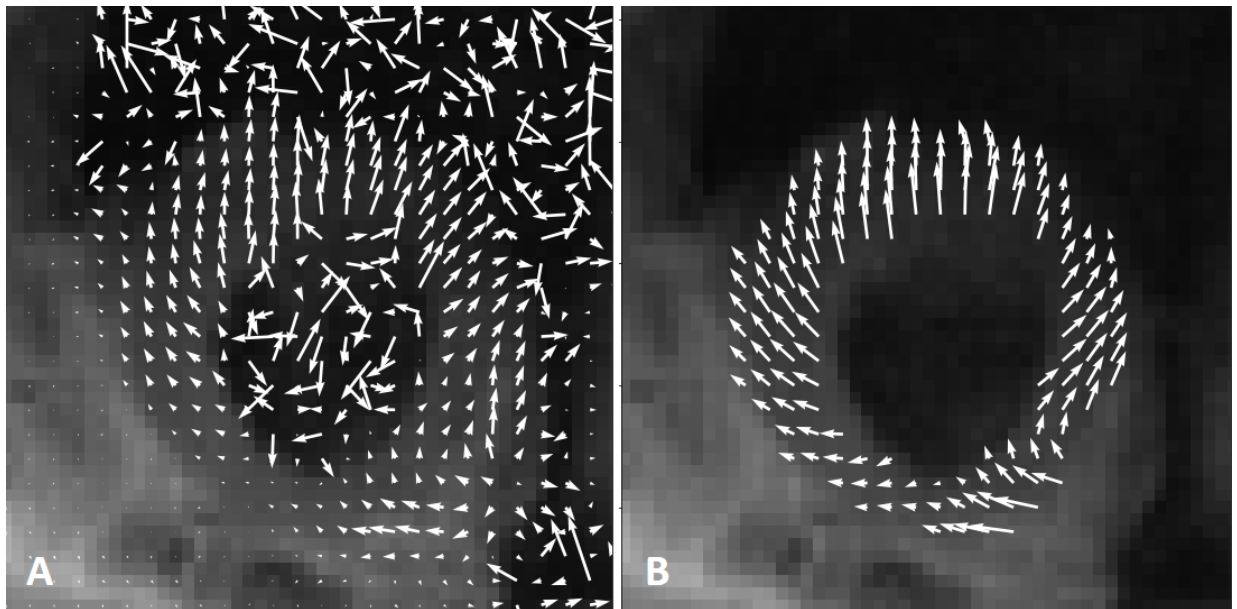


Figure 3.3: **A:** Velocity field  $\vec{u}$  in a 2D SHAX slice in early diastole, including noisy signal in the blood. Magnitude plot in the background. Vectors are plotted with a spacing of one voxel. **B:** The same field at the same time but with Equation 3.1 applied to velocity components  $u_x$  and  $u_y$  and a binary myocardium mask applied.

The effect of smoothing the velocity field and then applying the mask is demonstrated in Figure 3.3. Seeing the effect of the mask is obvious, but notice how the velocity field within the myocardium also becomes more uniform in magnitude than in the initial data as well.

### 3.2.3 Numeric implementation of Selskog method

With the velocity fields from our TPM data we can calculate strain rate tensors in every voxel at every time point via the Selskog method discussed in Section 2.3. This includes smoothing of the velocity fields prior to any calculations to limit the effect of noise on gradient calculations. A numerical implementation of the velocity gradient, weighted by certainty values to suppress blood signal, is defined like this (15):

$$\frac{\Delta u_k}{\Delta x} = \frac{c_{k+1}(u_{k+1} - u_k) + c_{k-1}(u_k - u_{k-1})}{\Delta x(c_{k+1} + c_{k-1})}, \quad (3.2)$$

where  $\Delta x$  is the image resolution in the direction of the gradient and  $u_k$  and  $c_k$  are the velocity and certainty in a voxel  $k$ . To calculate the strain rate tensor  $D_{ij}$  (Equation 2.8) in voxel  $k$  in a cartesian 3D velocity field, we need this  $3 \times 3$  gradient tensor  $L_{ij}$  via Equation 2.7:

$$L_{ij} = \begin{bmatrix} \frac{\Delta v_x}{\Delta x} & \frac{\Delta v_x}{\Delta y} & \frac{\Delta v_x}{\Delta z} \\ \frac{\Delta v_y}{\Delta x} & \frac{\Delta v_y}{\Delta y} & \frac{\Delta v_y}{\Delta z} \\ \frac{\Delta v_z}{\Delta x} & \frac{\Delta v_z}{\Delta y} & \frac{\Delta v_z}{\Delta z} \end{bmatrix}, \quad (3.3)$$

where the x- and y-directions are in the SHAX plane and the z-direction is orthogonal and out of plane (longitudinal direction). For a  $2 \times 2$  gradient tensor from a 2D field, we simply get:

$$L_{ij} = \begin{bmatrix} \frac{\Delta v_x}{\Delta x} & \frac{\Delta v_x}{\Delta y} \\ \frac{\Delta v_y}{\Delta x} & \frac{\Delta v_y}{\Delta y} \end{bmatrix}. \quad (3.4)$$

To get correct gradient values we need to take into account the voxel dimensions in the TPM data, which is especially important in 3D because  $\Delta x = \Delta y \neq \Delta z$ . From the metadata we find that the slice thickness is  $\Delta z = 1.5mm$ , while the in-plane voxel resolution is  $\Delta x = \Delta y \approx 0.35mm$ .

When we apply masks to the velocity fields we exclude voxels that are outside the myocardium, but the mask borders may still be an issue when calculating gradients. When the strain rate tensor is calculated in a voxel, the gradients require velocity values in adjacent voxels in the gradient direction (as seen in Equation 3.2). If the voxel is positioned right at the edge, one of its neighbors could be outside the mask and distort the gradient value because it contains noisy signal from the blood.

Noise contamination is supposedly compensated for when using Equation 3.1 to smooth the velocity field, but we can also choose to exclude the outermost voxels by performing a "binary erosion" of the mask to avoid the issue altogether. This shaves off a layer of voxels on the inside and outside edges and ensures that all in-plane gradient

calculations are performed completely within the mask. This is demonstrated in Figure 3.4.

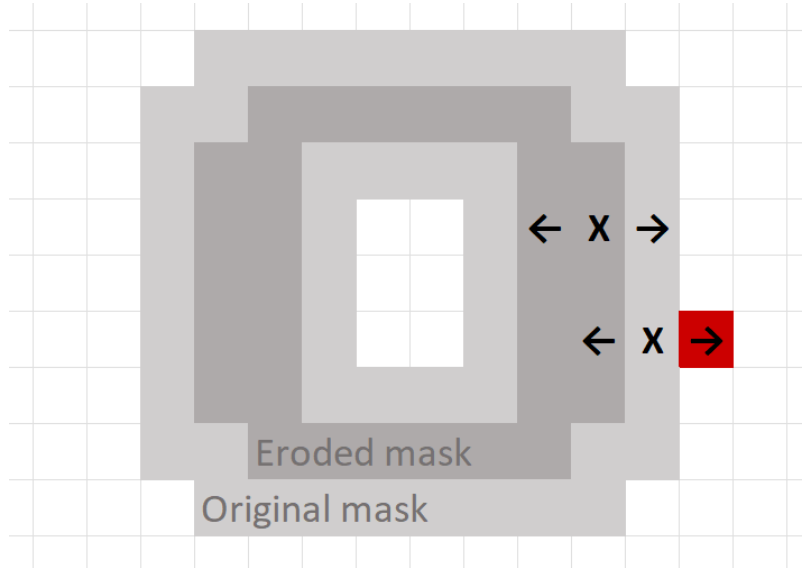


*Figure 3.4: A demonstration of binary erosion. For any sampled voxel ("X") in the eroded mask, it will always have neighbors inside the original mask.*

This could, however, mean that we sacrifice data along the epi- and endocardium that is valuable in LV deformation analysis, especially longitudinal strain (30). We will investigate if the smoothing function sufficiently counters border artifacts, and apply binary erosion if not to more directly prevent blood signal contamination.

Blood signal is especially an issue when calculating gradients in the z-direction. In this case the gradients require velocity values in the slices above and below, and as the radius of the LV masks vary in different positions we hit a lot of zeroes outside the masks. We solve this by applying a "Nearest Neighbor" function, where the framework finds the nearest non-zero value (from the slice where we hit a zero) and uses that instead. This leads it to find velocity data in the myocardium nearby.

### 3.2.4 Ellipsoid tensor visualization

We now have the tools to calculate strain rate tensors in each voxel of the myocardium for every frame over a full heart cycle, using smoothed velocity fields. To interpret these tensors, it is useful to visualize them in a way that intuitively communicates their direction and magnitude of strain rate.

The eigenvectors of the tensor are always orthogonal to each other, and we can use them to span the half-axes of an ellipsoid, or in the two-dimensional case: simply an ellipse (15). The ellipse shape is intended to deform according to the strain rate direction and magnitude that corresponds to its half-axes, meaning that it should expand along the axis where we have stretching (positive eigenvalues) and contract along the axis with compression (negative eigenvalues) or have a roughly spherical shape when the magnitude is around zero.

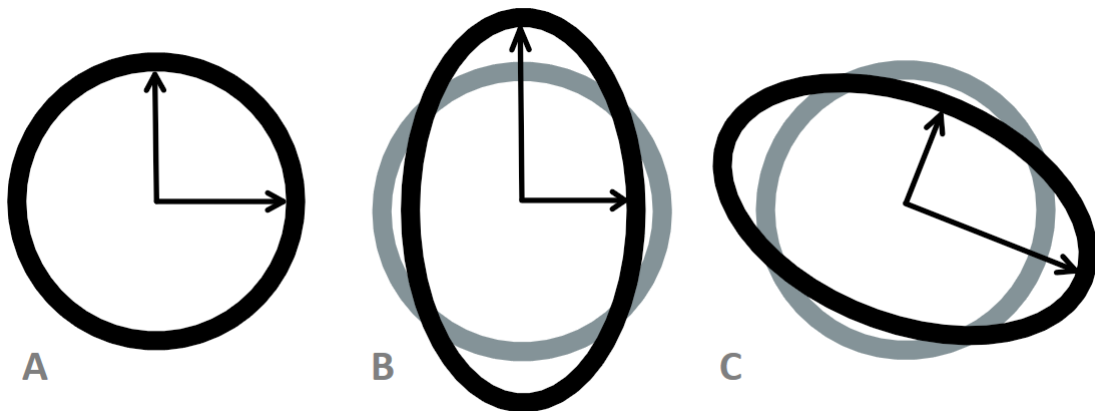


*Figure 3.5: Ellipses spanned by eigenvectors of various directions, vector lengths modulated by eigenvalues. A: magnitudes around zero; no deformation gives a circular shape. B, C: Stretch and compression give elliptic shapes.*

A circular shape could also represent a tensor that either expands or contracts equally along both half-axes. We expect, however, to see compression along one eigenvector and expansion along the other for the majority of 2D strain rate tensors due to the assumption of the heart tissue being incompressible and assuming conservation of mass.

To visualize the tensors as these ellipses, we transform the magnitudes to force the eigenvalues to be positive definite (31). In other words, all positive and negative eigenvalues are transformed to some positive value relative to the unit circle radius of 1. We have chosen to use the function  $w(\lambda_i) = \tanh(\lambda_i) + 1$  where  $\lambda_i$  is some eigenvalue. This transforms the half-axes with positive eigenvalues to have lengths in the range  $w \in (1.0, 2.0)$ , the negative values to have values in the range  $w \in (0.0, 1.0)$  and ensures that  $w(\lambda_i = 0) = 1$ . Letting the eigenvector pairs with transformed lengths  $w(\lambda_i)$  span ellipses gives us the desired visuals in Figure 3.5.

Keep in mind that this function is only applied as a *visual* tool for the ellipse plotting, and not in the quantitative analysis. This means that the constants above are somewhat arbitrary and could be scaled later for visibility, but the point is that it produces the correct ellipse proportions and normalizes the scale to make the low magnitude tensors clearly visible. The same principle goes for 3D strain rate tensors too, but with an ellipsoid spanned by three orthogonal eigenvectors.

To more effectively communicate the regional variation in strain rate direction and magnitude visually, we can choose different parameters to assign to a color range and to the opacity of the ellipses. One such parameter, from assessing the direction of some tensor in the myocardium, is the angle  $\theta_i$  of the eigenvectors relative to radial direction as defined in Figure 3.6.

Here we also demonstrate that the alignment of the ellipse relative to the radial and circumferential (tangential) axes determines strain rate direction. In other words, if you flip any of the eigenvectors 180° they still correctly describe the direction. Because the LV moves and deforms from its initial position and shape, we need to calculate the LV center position for every frame to ensure that this geometric model is consistent.

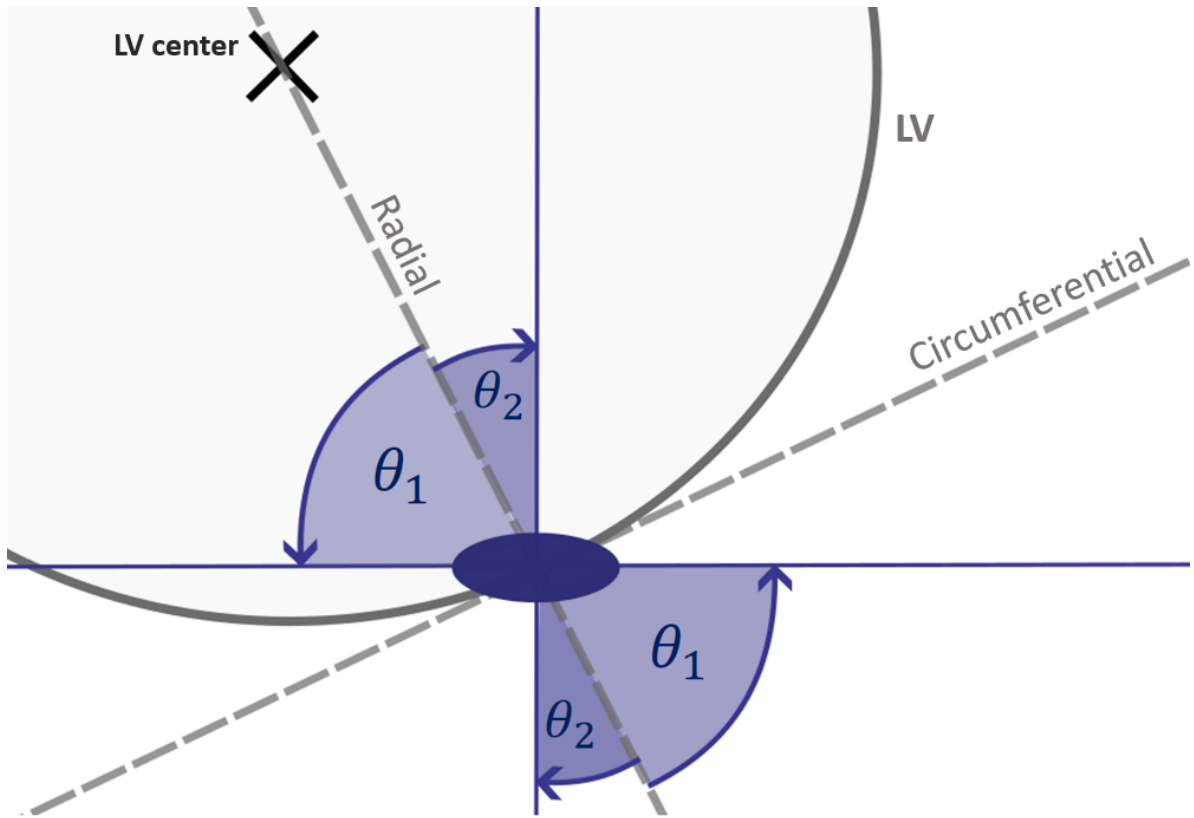


Figure 3.6: Diagram of an ellipse positioned in a coordinate system with radial and circumferential axes (dashed lines) defined by LV geometry and ellipse position. The ellipse half-axes, representing the tensor eigenvectors  $\vec{v}_1$  and  $\vec{v}_2$ , are oriented with angles  $\theta_1$  and  $\theta_2$  with respect to the radial axis.

This means that all possible ellipse alignments in xy-space can be described by the range of a single angle  $\theta_1 \in [0, 90]^\circ$ , where  $0^\circ$  represents a completely radial alignment and  $90^\circ$  a circumferential alignment.  $\theta_2$  is always orthogonal to  $\theta_1$  in the xy-plane for 2D strain rate tensors. We will map the angle of each tensor's most positive strain rate (stretch) to a color scale with this range to get a visual of directional homogeneity when plotting the ellipses. The opacity will be assigned to the Invariant  $I$  via Equation 2.9, representing total strain rate magnitude, which will create a 'dimming' effect in voxels with low-magnitude strain rate values that can be used to clearly reveal areas of myocardial dysfunction along the LV.

### 3.2.5 Eigenvector decomposition

The angles  $\theta_i$  will not only be used for visual analysis, but will also be used to gather quantitative information. Vector decomposition, using the eigenvector angles  $\theta_i$  and eigenvalues  $\lambda_i$  as vector length, can be used to find the radial and circumferential components  $r_i$  and  $c_i$  of the strain rate in each voxel. These components are simple to find using the trigonometric formulas for right triangles, which we can construct with the eigenvalue  $\lambda_i$  as the hypotenuse and  $r_i$  and  $c_i$  as the catheti. This is shown in Figure 3.7.

For a slice at some time-point in our MR recording we generally have hundreds of

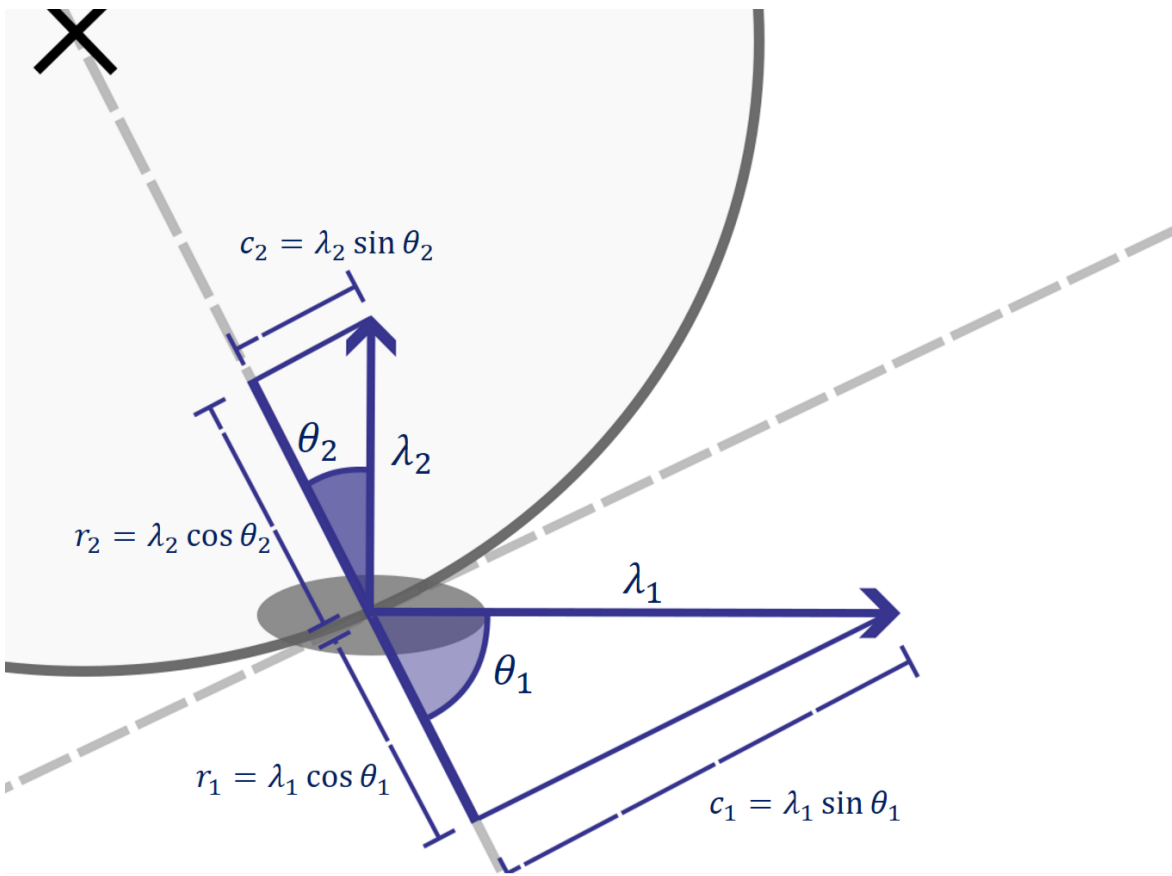


Figure 3.7: The eigenvectors represented by the ellipse in Figure 3.6 in the same coordinate system. Radial and circumferential components  $r_i$  and  $c_i$  are defined by corresponding  $\theta_i$  and  $\lambda_i$ .

voxels in the LV to sample, so we need some way of organizing the data we collect from the tensors in each of these. When using 2D strain rate tensors to analyze the voxels in the LV mask we are interested in their weighted average sum of radial and circumferential strain rate where the radial and circumferential components  $r_i$  and  $c_i$  of one tensor are calculated as shown in Figure 3.7. The weighted average sums of these components represent the global radial and circumferential strain rate for this LV slice.

### 3.2.6 Global LV strain rate

When plotting the global radial and circumferential strain rate for all of the time-points of velocity data in a slice from the LV base, we expect to see curves describing the deformation throughout the cardiac cycle as described in section 2.2.1. Whether we get a positive or negative peak depends on the sums of positive and negative eigenvalues  $\lambda_i$  modulated by the trigonometric functions defined by strain rate angles  $\theta_i$ .

To get correct peak values, we need to make sure that the units are scaled correctly throughout the calculation process. Firstly, we need to keep count of the amount of tensors generated within the LV slice at any time point as the myocardium mask changes its shape and size throughout the cardiac cycle. Dividing the strain rate sum for this frame by this amount is how we get a weighted average measurement and also prevent larger LV cross-sections from giving a higher signal because it has more voxels in the

mask. Secondly, the units of the velocity components are  $cm/s$ , and we want strain rate measured in the unit  $s^{-1}$  which means all spatial and temporal variables should be converted to  $cm$  and  $s$ .

Previously, we have smoothed the velocity field in the SHAX xy-plane, but we have not yet smoothed our data in the time dimension. We expect the initial curves to be noisy because of this. To solve this we simply apply a running average smoothing function on the strain rate curves. The running average function convolves the curve with a kernel of length  $N = 2, 4, 6\dots$  with elements  $1/N$ . For  $N = 4$  a datapoint is transformed to the average of itself and its 4 surrounding points within the kernel, and higher kernel sizes increases the amount of smoothing.

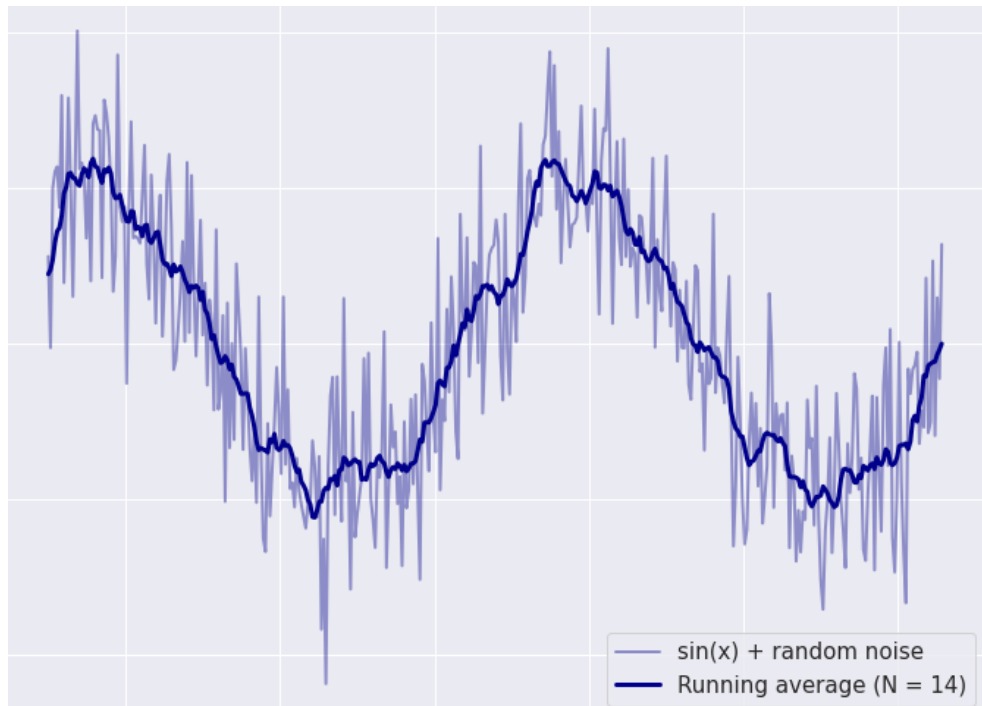


Figure 3.8: Sine signal with random noise and a curve showing the same signal smoothed by running average function using  $N = 14$ .

Figure 3.8 shows a simple example of the smoothing application of the running average function on a noisy sine wave. In this example we see that the smoothed curve represents an 'underlying' sine curve clearer and has more distinct peaks and valleys, but it is also worth noting that this function essentially acts as a low-pass filter on the signal. This means that the highest signal peaks are reduced after smoothing, and we should keep in mind that higher kernel sizes  $N$  give both more smoothing and lower peaks. To minimize the chance of reducing the peak values of our 'underlying' signal, we will attempt to find a balance by finding the lowest  $N$  that gives readable and coherent curves with distinct peaks. Based on this condition we chose a kernel size of  $N = 4$ .

Based on our physiology overview in section 2.2.1, we expect the radial strain rate curve to have a positive peak in systole ("GRSRs") as the myocardium wall thickens and a negative peak in diastole ("GRSRd") as it relaxes. The circumferential peak directions we expect to be opposite ("GCSR<sub>s</sub>" negative and "GCSR<sub>d</sub>" positive) as the

circumference shortens and then expands, but lower magnitude than the radial peaks (32). The "diastolic" strain rate peaks (with " $d$ " subscript) are equivalent to what is commonly referred to as "early diastolic" strain rate peak (" $SRe$ ") in literature (32).

### 3.2.7 Global LV strain

From theory section 2.3 we know that we can find strain from time-integrated strain rate. In our framework we use cumulative trapezoidal numerical integration to produce strain curves from our measured strain rate data. Specifically, we use the "cumulative\_trapezoid()" function from the "scipy.integrate" module. The units will be %, representing relative deformation from the initial time-point.

Despite previously smoothing the strain rate data, the strain curves can still be affected by noise. Velocity offset in PC-MRI due to gradient eddy-currents can be a source of background noise that can accumulate during integration. This effect, in the context of cyclic motion, has been investigated in detail in a study by Pelc et al. (33).

In this study, they modelled time-dependent integrated noise to represent how the accumulated noise increases all the way to the end of a recorded time sequence. They also demonstrate that integrating both forward and backward along the timeline and using a linear combination of them both lets us minimize noise at the beginning and end of the acquisition, as shown with the combined curve in Figure 3.9B.

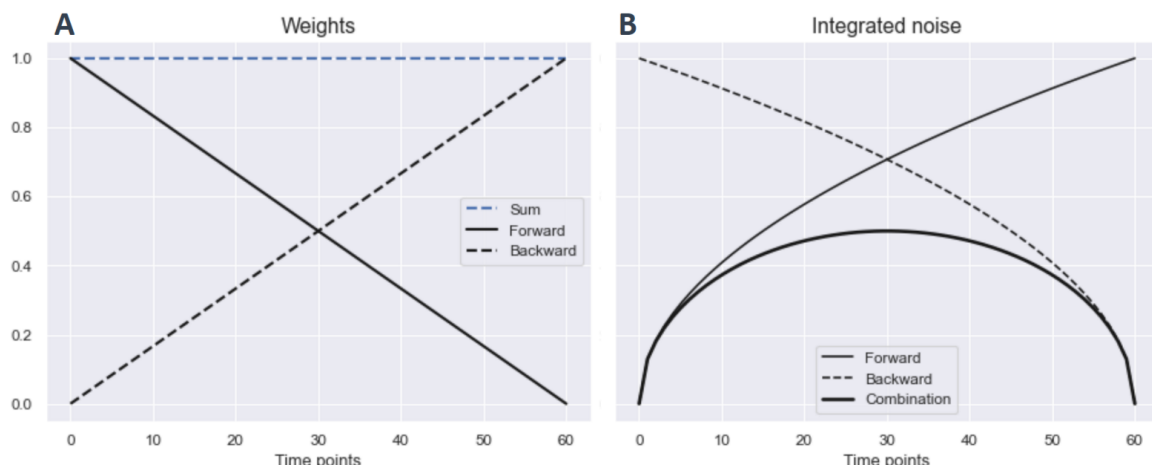


*Figure 3.9: A: Linear weights designed to gradually cancel out signal at time points where integrated noise is higher. Their sum is included to illustrate that the signal is not damped or amplified by the combination. B: Mathematical models of accumulated noise from forward and backward integration, inspired by a figure from Pelc et al. (33). The combined curve illustrates minimization of accumulated noise at both ends achieved with the linear weights.*

The study also suggests the application of linear weights to the forward and backward integrated curves (33), shown in Figure 3.9A. The sum of these weights always equals 1 to ensure that the signal is not reduced or amplified at any point, but they prioritize the integrated curve with the least accumulated noise at each time point. Both curves will be weighted equally in the middle, where accumulated noise is expected to be the same.

These principles and models will be applied in our framework. For strain curves calculated with forward integration  $S_f$  and backward integration  $S_b$  the following linear weights will be produced:

$$w_f = (T_{ed} - t)/T_{ed}, \quad w_b = t/T_{ed}, \quad (3.5)$$

where  $T_{ed}$  is the end diastolic time point in the relevant acquisition. The combined strain signal that we will use in the analysis can now be produced through linear combination:

$$S = w_f S_f + w_b S_b. \quad (3.6)$$

We expect each strain curve to have a singular peak around the end of systole, beginning of diastole. Based on our physiology overview in section 2.2.1, we expect the radial strain curve to have a positive peak ("GRS") that represents wall thickening and the circumferential strain curve to have a negative peak ("GCS") representing circumference shortening.

### 3.2.8 Regional strain rate and strain

To perform regional strain rate and strain analysis, we want to divide the LV into sections that can be analyzed separately to assess strain homogeneity. From the TPM data structure we can find time-dependent sector maps for each slice with the same dimensions as the image and velocity matrices that assign every voxel to one of 36 sectors as shown in Figure 3.10A. Infarcted hearts will also include infarct sectors in the metadata designed during processing. In the case of the figure, the metadata would contain a tuple "(1, 10)" representing an infarct sector range from 1 to 10.

For the infarcted hearts, we want the infarcted sectors (as determined by LGE images) to be part of one group. The remaining LV will be split into six and distributed to three groups based on proximity to the infarct sectors: adjacent, medial, remote (34). This is shown in Figure 3.10B. If the remaining sector amount is not divisible by 6 we round down to the closest number and assign the remaining sectors to the remote group.

The Sham control group will of course not have infarct sectors, and some in the MI group as well if there was no visible infarct in the MRI LGE images. In these cases, we choose an infarct sector range approximately where we find infarction in the MI hearts and rename the groups to "Group 1" and so on. For this use we have chosen to define Group 1 by the range [4, 13] which ensures that the four groups approximately cover the same amount of sectors.

When calculating strain curves for all four LV sectors we expect to see an increase in dyssynchrony between them in the MI group. This will be parameterised as Systolic Dyssynchrony Index (SDI); the standard deviation between the time points of the regional strain peaks as a percentage of the whole cardiac cycle duration to be able

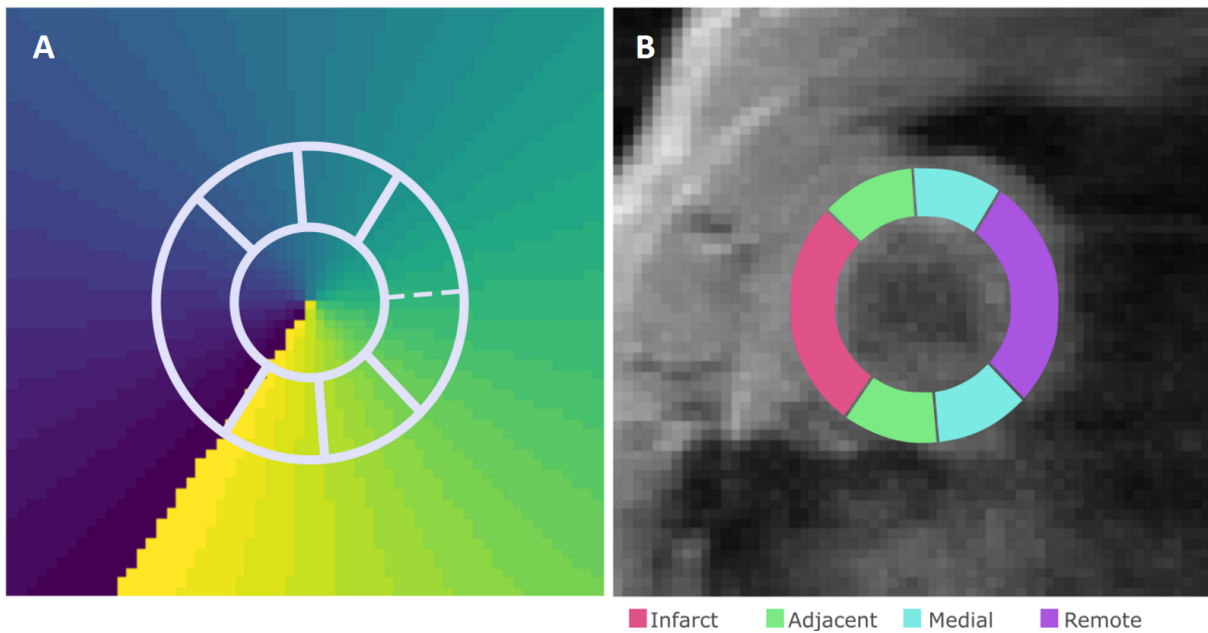


*Figure 3.10: A: Sector map plotted as a clockwise color scale from sector 1 to 36, divided by isotropic lines from the LV center. Different LV sections are outlined where the largest (from sector 1 to 10) represents the infarct sectors of this heart. The rest is divided into 6 equal parts. B: The same sector groups color coded based on infarct proximity.*

to compare measurements between rats with different heart rates (35). Higher values represent a higher level of dyssynchrony between the LV segments. In this thesis we will distinguish between SDI measured from radial and circumferential strain curves as "RSDI" and "CSDI".

We can now perform strain and strain rate analyses like we did for the whole LV but with each of these groups separately, which lets us observe regional variation between the different sections of the LV.

### 3.2.9 Eigenvector angle distributions

The analysis described thus far relies on the vector decomposition of strain rate tensor eigenvectors and eigenvalues in the radial and circumferential direction in our LV model, which is conventional in LV strain analysis. However, a unique property of our tensor framework is that we can look at strain rate magnitude and direction for every individual voxel in the image that contains myocardium.

We will attempt to make use of this by plotting distributions of eigenvector angles in the range  $\theta_i \in [0, 90]^\circ$  relative to the radial axis over the cardiac cycle duration. We will divide the vectors into two groups based on whether they describe stretch or compression. The intent with this kind of analysis is to study how the myocardium is organized as it deforms during the cardiac cycle, regardless of the magnitude of strain rate and unrestrained by conventional LV geometry, and see if angle distribution characteristics correlate to infarct progression.

To the extent of our knowledge, this kind of analysis has not been performed before to

assess heart function. This means that we need to observe these distributions for sham and MI hearts and attempt to interpret them and see if there are quantifiable differences we can establish as a parameter that reflects myocardial function. This will be discussed further in section 4.1.5.

### 3.2.10 Framework adjustments for 3D analysis

We can expand our framework to include 3D strain rate tensors, which lets us perform strain analysis out of the SHAX xy-plane. This requires the introduction of the longitudinal axis and another directional parameter  $\phi$ , as defined in Figure 3.11. We choose a cylindrical coordinate system in our 3D model, meaning that we define the longitudinal direction to always be in the z-direction and that the LV center is always defined in-plane for any slice along the LV.

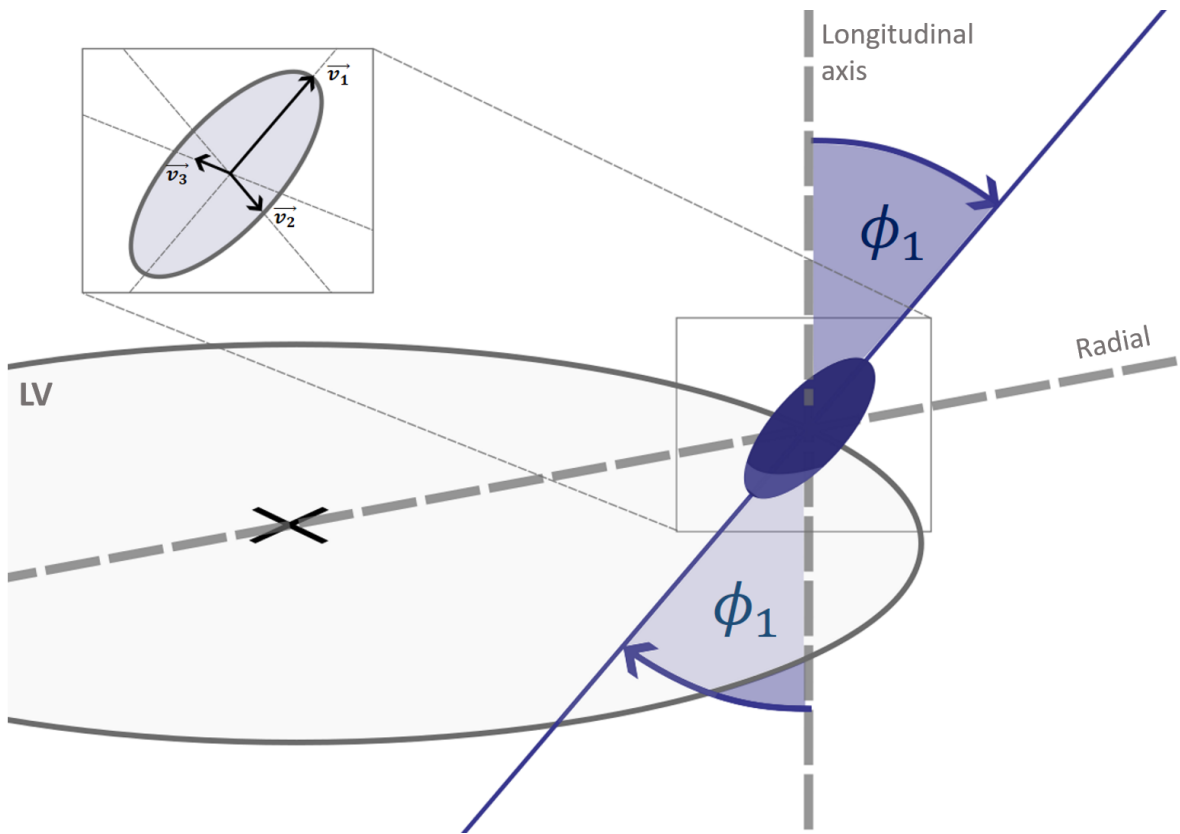


Figure 3.11: 3D strain rate tensor ellipsoid placed in LV coordinate system, where its most positive eigenvector  $\vec{v}_1$  has an angle  $\phi_1$  relative to the longitudinal axis.

The depicted ellipsoid in Figure 3.11 is spanned by three orthogonal eigenvector and eigenvalue pairs as established in Theory section 2.3 that can point in any directions in 3D space, unlike the 2D tensors confined in the xy-space. We choose to describe these directions using  $(\theta, \phi)$ -coordinates, where  $\theta$  relative to radial axis is defined as before and is found from in-plane projections of each eigenvector.

The in-plane angle  $\theta$  can be used like before to obtain radial and circumferential components of strain rate, but now we can also find the longitudinal component simply as

$l_i = \lambda_i \cos\phi_i$ . When using the 3D tensors, the framework will also collect directional parameters with  $\phi$  values in the range  $\phi \in [0, 90]^\circ$  to study how the distributions change over the cardiac cycle, where  $\phi = 0^\circ$  is completely out-of-plane and  $\phi = 90^\circ$  is completely in-plane.

The longitudinal strain and strain rate curves are expected to behave similarly to their circumferential counterpart with regards to shape and magnitude (negative peak "*GLS*", negative "*GRSRs*" and positive "*GRSRd*"), but in this case describing longitudinal shortening (32).

### 3.2.11 Parameter summary

Finally the framework needs to measure and store a selection of the curve parameters described throughout this chapter, and this selection will be summarized here. The parameters we will collect for the in-plane 2D strain rate tensor analysis of the basal-slice LV model are:

*Condition* - (1 = MI, 0 = Sham)

*Time* [days] - Time after operation

*GRS* [%] - Global Radial Strain peak

*GCS* [%] - Global Circumferential Strain peak

*GRSRs* [ $s^{-1}$ ] - Systolic Global Radial Strain Rate peak

*GRSRd* [ $s^{-1}$ ] - Diastolic Global Radial Strain Rate peak

*GCSRs* [ $s^{-1}$ ] - Systolic Global Circumferential Strain Rate peak

*GCSRd* [ $s^{-1}$ ] - Diastolic Global Circumferential Strain Rate peak

*RSDI* [%] - Radial Systolic Delay Index

*CSDI* [%] - Circumferential Systolic Delay Index

$\theta_{ss}$  [°] - In-plane Systolic Stretch angle

$\theta_{sd}$  [°] - In-plane Diastolic Stretch angle

$\theta_{cs}$  [°] - In-plane Systolic Compression angle

$\theta_{cd}$  [°] - In-plane Diastolic Compression angle

The stretch and compression parameter definitions are original to this thesis, and were determined after studying angular distributions of Sham and MI hearts. They represent the mean direction of stretch and compression at the time the angle distributions are the most concentrated. We will discuss our design of these parameters and their definitions

in more detail in section 4.1.5 in relation to these plots.

For analysis using 3D strain rate tensors using the whole-LV segmentation model, additional parameters will be collected to describe motion out of the SHAX plane:

$GLS [\%]$  - Global Longitudinal Strain peak

$GLSRs [s^{-1}]$  - Systolic Global Longitudinal Strain Rate peak

$GLSRd [s^{-1}]$  - Diastolic Global Longitudinal Strain Rate peak

$\phi_{ss} [^\circ]$  - Through-plane Systolic Stretch angle

$\phi_{sd} [^\circ]$  - Through-plane Diastolic Stretch angle

$\phi_{cs} [^\circ]$  - Through-plane Systolic Compression angle

$\phi_{cd} [^\circ]$  - Through-plane Diastolic Compression angle

where "global" in this case refers to a weighted average sum of peak values across all LV slices used.

We will also look at the difference between the in-plane angle distribution parameters measured in the basal and apical half of the LV, to investigate if heterogeneity in strain rate direction across slices can be linked to myocardial dysfunction. From visually studying angle distribution heterogeneity in the whole LV model, we determined to look at this specifically during systole. This choice will be discussed later in section 4.2.3 in relation to plots that visualize regional variation between levels. These measurements will be denoted with as  $\Delta\theta_{ss}$  and  $\Delta\theta_{cs}$ .

We will use the Pandas module in a Python script to organize all of the parameters measured during analysis for each dataset and save it as a "dataframe" structure, which lets us intuitively group measurements to suit our statistical models.

### 3.3 Statistical analysis

Our complete strain rate tensor framework has the ability to assess 2D strain rate in a single slice LV model and 3D strain rate in a whole-LV model, and now we can apply it in a broader statistical analysis to attempt to identify regional myocardial dysfunction and study how it develops over time. We will apply our Python framework to all datasets of rat hearts and collect characteristic curve parameters that represent myocardial function of the LV and see how these change over days after operation. We will divide Sham and MI hearts into respective groups, with Sham acting as control group, and compare them. Strain and strain rate measurements will be compared to other studies on LV dysfunction in rat hearts as a way to prove the viability of the numerical implementation of the Selskog method.

We plan to structure our statistical analysis in a way that lets us see if the infarcted

hearts show trends over time that deviate from the control group, and could indicate the effects myocardial dysfunction. The following sections will cover the statistical methods we are planning to use, and how they will be applied.

### 3.3.1 Linear regression

When plotting the measurements as a function of days after operation, and grouping them by Sham and MI, we will get scatter plot distributions that can reveal differences between the groups. We are interested in mean values for each group, but also to quantify how they change over time and whether or not this change is significant. For this we will use linear regression to estimate a regression line  $y(t)$ :

$$y(t) = t\beta_1 + \beta_0, \quad (3.7)$$

where  $\beta_0$  is the y-axis intercept of the linear fit,  $\beta_1$  is the slope value and  $t$  is time in days after operation. Using the "linregress()" function for least squares linear regression from the `scipy.stats` module to calculate these values, we also get a p-value ( $p \in [0, 1]$ ) that relates to  $\beta_1$ . A lower value indicates that the linear fit model is more confident in the  $\beta_1$  value and indicates that there is systematic correlation between the measurements and time. By convention, we are going to assume that  $p < 0.05$  disproves the null hypothesis (in this case, the null hypothesis is that a parameter does not change over time) and indicates statistical significance (36).

95 percentile confidence intervals will be plotted along with the linear fits as a visual error estimate, representing an area that the regression model is confident that will contain 95% of regression lines from repeated measurements. We will also calculate the 95% confidence interval specifically for the slope value from the standard error  $SE$  of the slope which we get as an output from `linregress()`. This estimate, assuming a normal distribution of possible slope values, can be calculated as  $\pm 1.96 \cdot SE$  because the interval  $(-1.96, 1.96)$  contains the inner 95% of the distribution (37).

### 3.3.2 T-tests

Another method we will use to assess whether the Sham and MI groups develop differently after operation is by performing T-tests. Unlike the linear regression, where we will use all measured data, we will now only look at the data the last time point for each rat heart. We will refer to this as the chronic stage for the MI hearts, and their measurements will be compared to Sham hearts at the last time point. When we refer to "day 40+", it refers to the fact that there is some variation between the different rats in the timing of their last day of MR acquisition due to scheduling, from 40 to 45 days after operation. Mean values for both groups at these time points, with p-values calculated from independent two-sample T-tests (`ttest_ind()` from `scipy.stats`), will give us insight into whether the Sham and MI hearts have developed differently physiologically. If these differences are statistically significant ( $p < 0.05$ ), we can assume that this is due to myocardial dysfunction in the MI group.

# Chapter 4

## Results

This chapter presents the results produced by our Python analysis framework. We have produced plots of strain rate, strain, and eigenvector angle distributions from the cardiac cycles of Sham and MI rat hearts. We have collected curve parameters that were used in statistical analysis to attempt to detect reduction in myocardial function and link it to MI progression.

We have separated the results into two sections, one regarding 2D strain rate tensor analysis of the basal-slice LV model, and one using 3D strain rate tensors on the whole-LV model. This gives us two stages of analysis complexity and two ways of looking at regional variation of the deformation parameters.

### 4.1 2D strain rate tensor analysis

Results in this section were acquired from analyzing in-plane motion in a single basal LV slice using 2D strain rate tensors.

#### 4.1.1 Visualization

Figure 4.1 demonstrates the ellipse plot framework in action at two different time points in the cardiac cycle for a Sham heart, showing 2D strain rate tensors represented within the mask. The voxels are sampled in a grid with spacing of one voxel between each element for the sake of visibility. For quantitative results, however, we always utilize all of the voxels within the myocardium mask. The ellipse opacity corresponds to the invariant  $I = \lambda_1^2 + \lambda_2^2$  from Equation 2.9 to give another visual reference for the strain rate magnitude in each tensor.

#### 4.1.2 Tensor field optimization

We have also used our ellipse plotting tool to visually evaluate the effectiveness of the velocity smoothing function (Equation 3.1) by looking for border artifacts in plots with

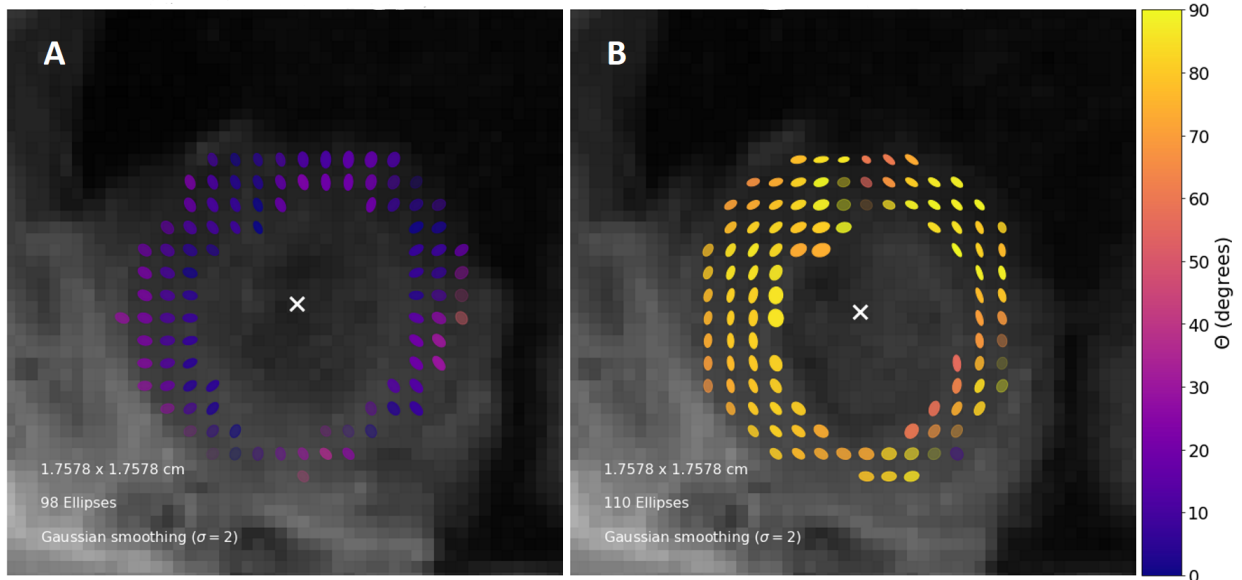


*Figure 4.1: Ellipse plots of a Sham heart with color scale defined by the direction of most positive eigenvalue relative to the radial direction from the LV center (marked 'X'). **A:** Mid systole, with the myocardium experiencing stretching in the radial direction and compression in the circumferential direction. **B:** Early diastole, stretch along the circumferential direction and compression in the radial.*

tensors sampled in all masked voxels of a Sham heart. Equivalent example plots using an eroded mask, and one excluding tensors with only positive or negative eigenvalues, were also produced for the sake of comparison in Figure 4.2. In the figure, it is apparent that exclusion removes ellipses at the mask borders at the endo- and epicardium that are abnormally small or large, which could be caused by border artifacts in the velocity gradient. Erosion appears to exclude some of these and more, while keeping some of the ellipses that were removed via exclusion. The eroded LV mask is noticeably thinner than its counterparts, having removed the inner and outer layer of voxels.

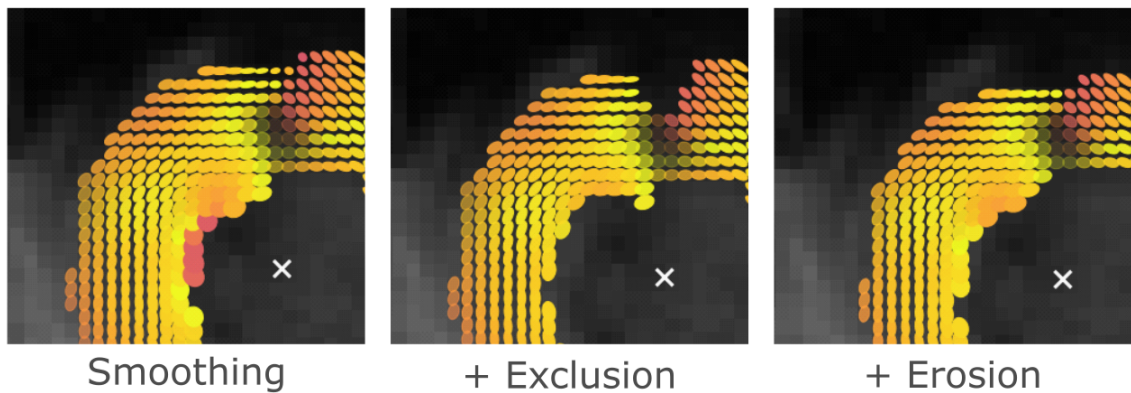


*Figure 4.2: Details of strain rate tensor fields at the same time point as shown in Figure 4.1B, but sampling every voxel within mask. The leftmost tensor field was calculated from a velocity field smoothed by Equation 3.1, with no further correction. Effects of correction via exclusion and erosion, separately, in addition to smoothing are demonstrated as well.*

### 4.1.3 Global strain rate and strain

Figure 4.3 demonstrates an example of measured radial and circumferential strain rate curves over one cardiac cycle, as well as their corresponding strain curves calculated using forward and backward integration over time as described in section 3.2.7. Systolic and diastolic global strain rate peak measurements (as established in section 3.2.11) are marked, as well as peak global strain values. This plot demonstrates the inconsistency of the late diastolic strain rate peaks, where it in this case is visible in the radial measurement but not in the circumferential. This is the reason for focusing on the early diastolic strain rate peaks (SRe) for analysis.

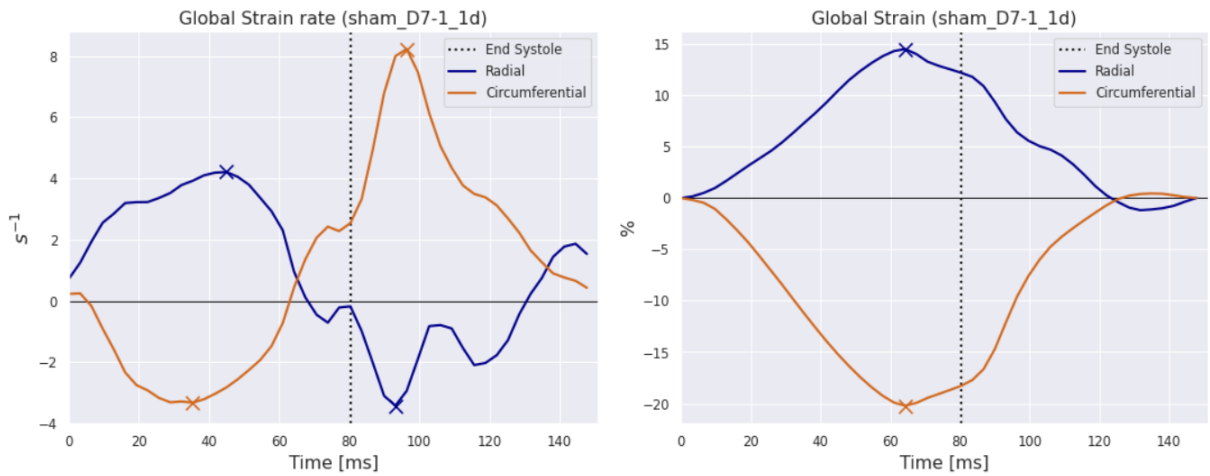


Figure 4.3: Global strain rate and strain curves from a single basal LV slice in a Sham heart at 1 day after surgery. Collected peak points are plotted as "X".

Mean measurements of these global peak parameters have been collected and are presented in Table 4.1 for the Sham and MI groups in the chronic stage of the disease (40+ days after infarct and operation). We observe that the global circumferential strain (GCS), and strain rate systolic and diastolic peaks (GCSR<sub>s</sub>, GCSR<sub>d</sub>) show a significant reduction in mean values between the groups, while no significant differences are observed in the radial peak measurements.

	<i>Sham</i>	<i>MI</i>	<i>p</i>
<i>GRS [%]</i>	$19.79 \pm 3.30$	$16.95 \pm 6.13$	.333
<i>GCS [%]</i>	$-19.82 \pm 3.03$	$-13.58 \pm 3.89$	.009
<i>GRSR<sub>s</sub> [s<sup>-1</sup>]</i>	$5.54 \pm 0.77$	$4.59 \pm 1.31$	.150
<i>GRSR<sub>d</sub> [s<sup>-1</sup>]</i>	$-6.33 \pm 1.42$	$-7.01 \pm 2.46$	.565
<i>GCSR<sub>s</sub> [s<sup>-1</sup>]</i>	$-4.42 \pm 0.83$	$-2.98 \pm 0.93$	.014
<i>GCSR<sub>d</sub> [s<sup>-1</sup>]</i>	$6.47 \pm 1.00$	$5.05 \pm 1.61$	.089

Table 4.1: Mean measurements (mean  $\pm$  std) of global strain rate and strain at the last day of MR acquisition, chronic stage for the MI group, for Sham ( $n = 6$ ) and MI ( $n = 7$ ). P-values are based on independent two sample T-tests between the the Sham and MI groups.

#### 4.1.4 Regional strain rate and strain

Figure 4.4 shows examples of ellipse and strain plots for a Sham and MI heart where the LV has been divided into groups to look at regional variation. Peak values on the strain curves that are collected for later statistical analysis are marked. Ellipse opacity is still modulated by strain rate magnitude, and reveals lower values in the infarct tissue in the red group. Visually comparing the circumferential peaks in the figure we can also see that the dyssynchrony in peak time between sectors appears to larger in the MI heart compared to in the Sham heart where they appear more synchronous.

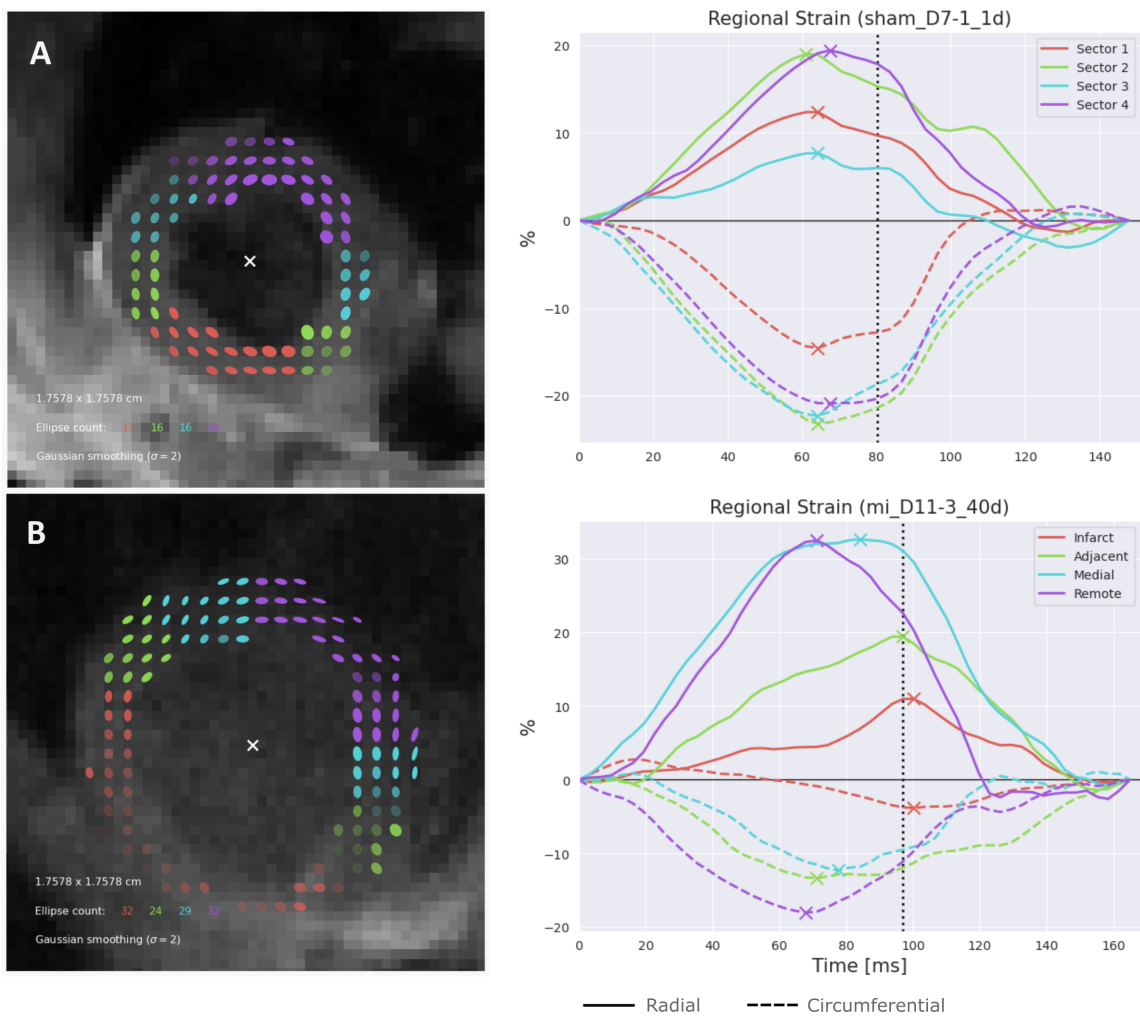


*Figure 4.4: Regional strain analysis of a representative Sham and MI heart, featuring strain rate tensor ellipse plots at early diastole and strain plots with color coding based on group. The end systole time point is marked with a dotted vertical line, and the curve peaks are marked with an "X". A: Sham heart with arbitrary, numerated sectors. B: MI heart 40 days after infarction, groups based on infarct sector and proximity.*

Figure 4.5 looks at regional strain for all hearts at the chronic stage, visualized using bar plots representing mean values and with error bars representing standard deviation. The individual measurements from each sector are plotted as scatter points. The sectors are color coded in the same way as seen in Figure 4.4. The brackets mark significance as determined from two-sample T-tests between the infarct sector (or "Sector

1" for Sham hearts) and the other sectors. From this plot we observed that GCS reveals significant difference between the infarct compared to the medial sectors, as well as infarct compared to remote, in the MI group. This indicates a significant reduction in circumferential strain in the infarcted tissue. A significant difference in GRS was also observed between Sector 1 and 4 in the Sham group.

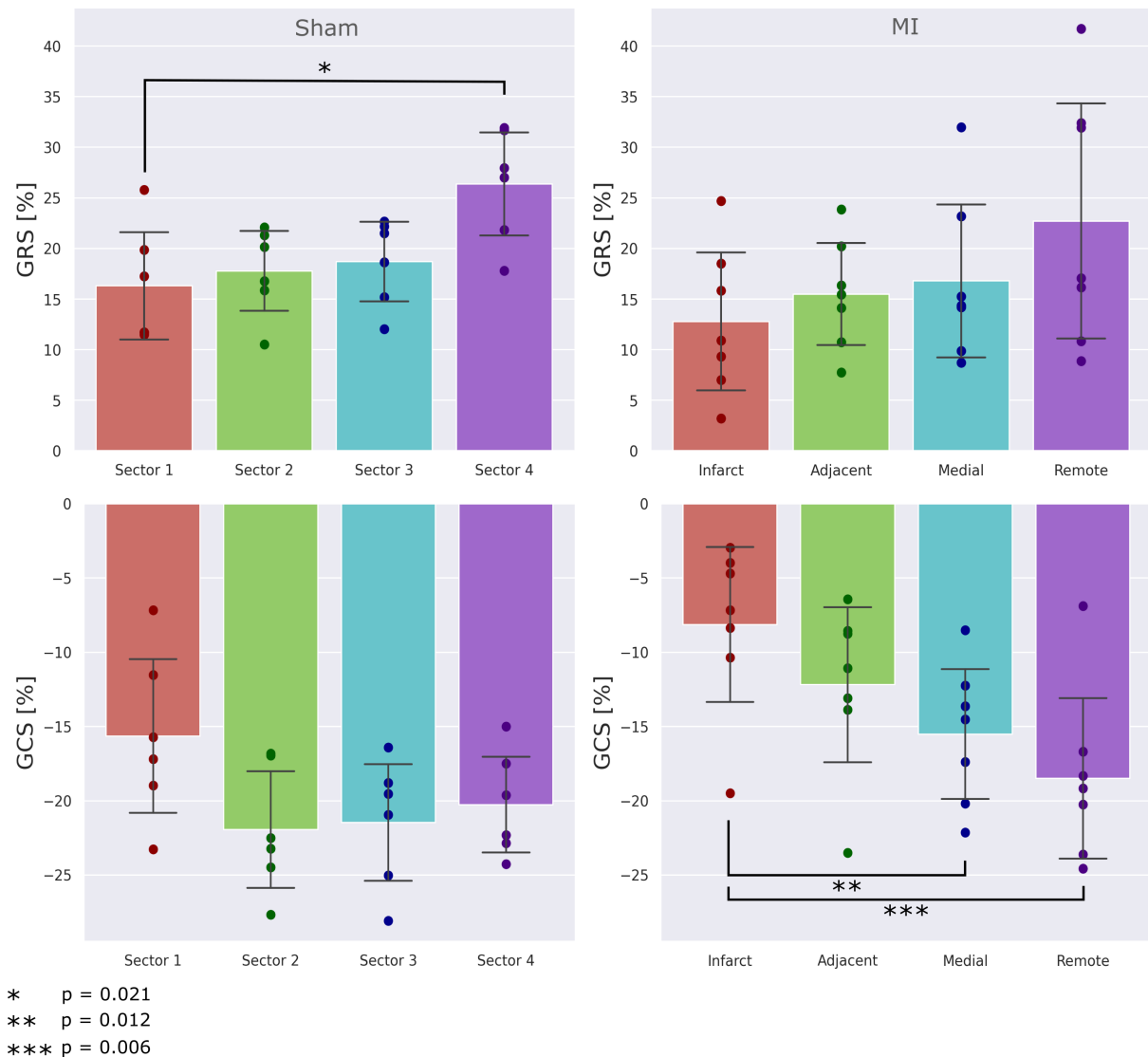


Figure 4.5: Regional variation of GRS and GCS shown with barplots of measurements from the four LV sectors in chronic stage MI hearts ( $n = 7$ ) and Sham ( $n = 6$ ) for control. The error bars represent standard deviation and the p-values are calculated via independent two-sample T-tests comparing each sector with the infarct sector, or "Sector 1" for Sham hearts. Statistical significance is marked with brackets.

Table 4.2 contains a comparison of mean measurements of dyssynchrony parameters in the chronic stage. We observed that both RSDI and CSDI were significantly higher in the MI hearts, indicating that they had a higher degree of dyssynchrony between the four sectors.

	<i>Sham</i>	<i>MI</i>	<i>p</i>
<i>RSDI</i> [%]	$3.81 \pm 2.15$	$7.09 \pm 2.61$	.033
<i>CSDI</i> [%]	$2.83 \pm 3.30$	$7.01 \pm 3.31$	.044

Table 4.2: Mean measurements (mean  $\pm$  std) of dyssynchrony in radial and circumferential strain at the last day after operation for Sham ( $n = 6$ ) and MI ( $n = 7$ ).  $p$ -values are based on two sample t-tests between the two groups.

### 4.1.5 Eigenvector angle distribution

Figure 4.6 shows examples of how the  $\theta$  angle distributions for a Sham and a late stage MI heart can look like, grouped based on whether they describe the direction of stretch or compression, change over the cardiac cycle. Considering that this kind of strain rate angle distribution plot is original, we will take a moment to describe it extensively here.

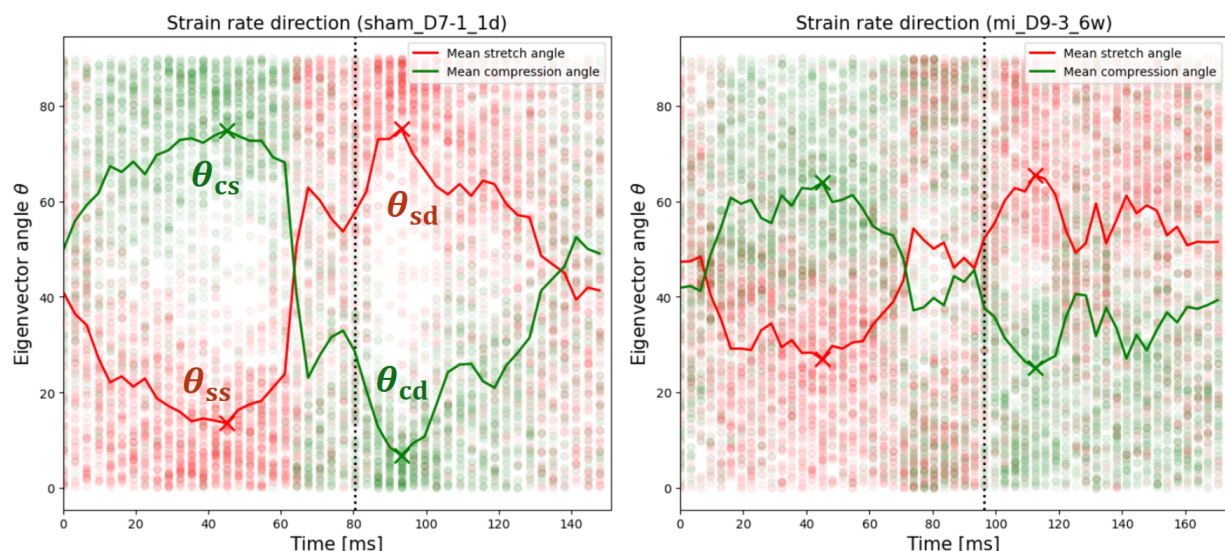


Figure 4.6: Distributions of tensor angles grouped by stretch (red) and compression (green) for a Sham (left) and MI (right) heart. Average angle for each time point represented by curves of corresponding color. Curve peaks and minima in systole and diastole are marked ("X"). Time point of end systole is marked with a dotted line.

The angle data are plotted over time, where we see that the scatter points describing direction of stretch and compression concentrate in opposite ends of the y-axis in systole and swap sides in diastole. During systole, compression angles concentrate toward  $\theta = 90^\circ$  and stretch concentrates toward  $\theta = 0^\circ$  relative to the radial axis. In other words, more compression happens in the circumferential direction and more stretching is happening in the radial direction during systole. The opposite can be seen during diastole.

The curves with colors corresponding to the distributions represent the mean angle at every time point, and appear cyclic with distinct peaks and minima. It also appears as if these curves are almost mirrored around  $\theta = 45^\circ$ , an angle that points equally in the radial and circumferential direction. This is a consequence of every 2D tensor having two orthogonal eigenvectors in the SHAX plane, where most of them contain

one vector describing stretch and one describing compression. The mean angle curves also show peaks during isovolumetric relaxation (IVR), right before the time point of end systole.

The red and green distributions of the MI heart do not appear to be as distinct as in the Sham plot, where we see areas of white between them. Distributions like this appear to have curve peaks closer to  $\theta = 45^\circ$  as they are less concentrated in the top and bottom of the y-axis and appear to 'blend' more into each other.

Based on these visual observations of the angle distributions, we chose to attempt to use the peaks marked in Figure 4.6 as functional parameters where the peak values represent myocardial function. These are named as shown in the figure and their abbreviations are listed in section 3.3.

	<i>Sham</i>	<i>MI</i>	<i>p</i>
$\theta_{ss}$ [°]	$14.07 \pm 2.24$	$21.72 \pm 6.04$	.014
$\theta_{sd}$ [°]	$73.85 \pm 3.15$	$69.03 \pm 6.09$	.110
$\theta_{cs}$ [°]	$74.80 \pm 3.08$	$68.59 \pm 4.72$	.019
$\theta_{cd}$ [°]	$13.38 \pm 2.49$	$19.75 \pm 6.39$	.043

*Table 4.3: Mean measurements (mean  $\pm$  std) of in-plane angle distribution parameters at the last day after operation for Sham ( $n = 6$ ) and MI ( $n = 7$ ). P-values are based on independent two sample t-tests between the two groups.*

Mean measurements of the angle distribution parameters were collected from the Sham and MI data at the chronic MI stage; the last day of MR acquisition for each animal. These measurements are presented in Table 4.3. Here we observe that there is a significant difference between the groups in three out of four of the  $\theta$  peak parameters, with the systolic parameters showing the lowest p-values. The values show what we also observed from the representative distributions in Figure 4.6; that the peaks of the MI hearts are closer to  $\theta = 45^\circ$ , which indicates a more heterogeneous distribution of angles.

#### 4.1.6 MI progression

In this section we will show the results of the larger scale statistical analysis that we designed to describe how the different parameters progress over time in the Sham and MI groups.

Figure 4.7 shows the linear regression analysis for a selection of parameters that were scored as significant (borderline significant in the case of  $\theta_{sd}$ ) indicating confident slope values and significant change over time in days.

The information presented in these plots are also summarized for all parameters established in section 3.2.11. Table 4.4, which shows a summary of all slope values from linear regression of the measurements of both groups with p-values corresponding to slope value. The confidence interval each slope value is included as an error estimate.

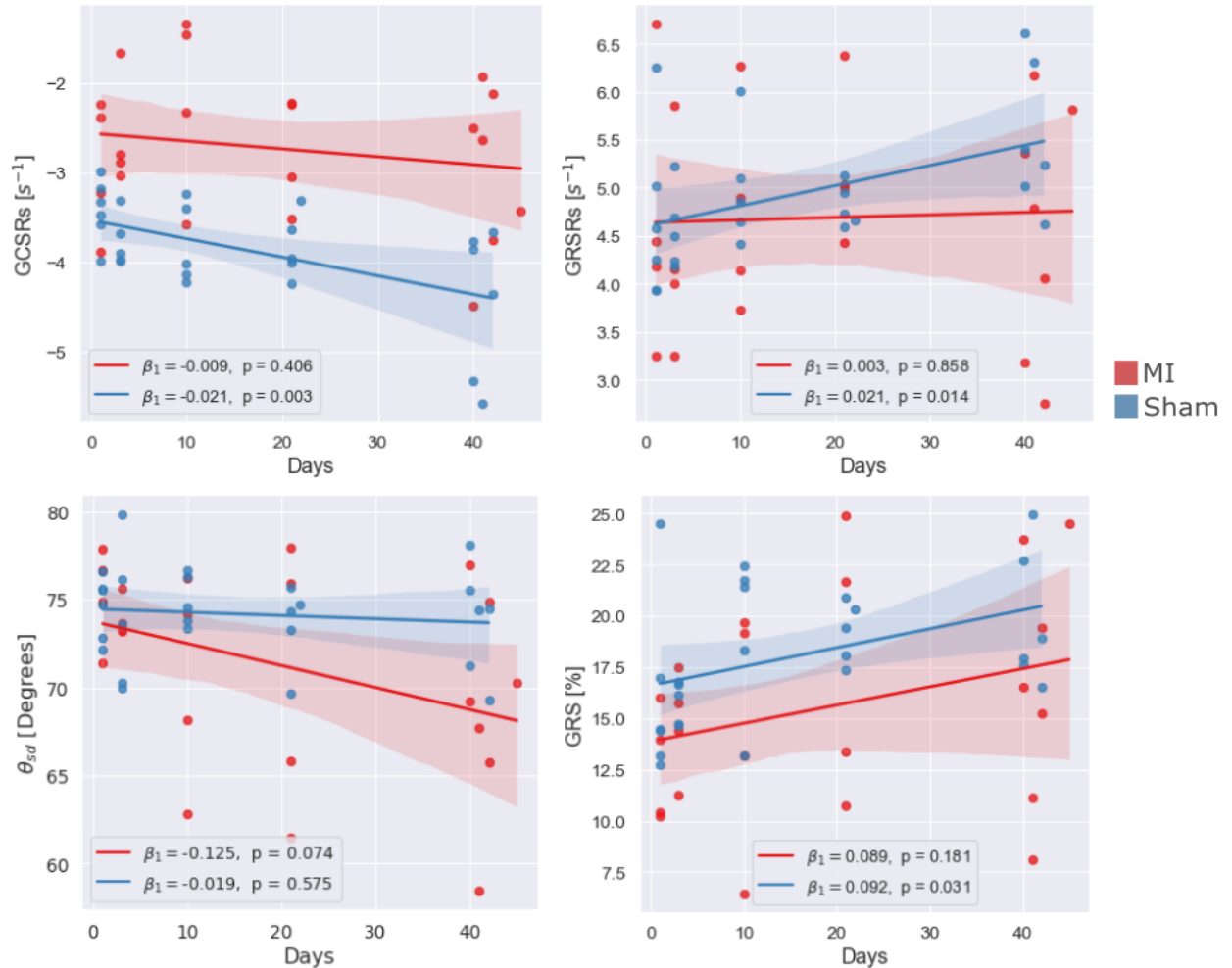


Figure 4.7: Scatter plots of a selection of measured parameters as a function of days and grouped by Sham ( $n = 27$ , blue) and MI ( $n = 23$ , red). Slope values  $\beta_1$  from linear regression and corresponding  $p$ -values in legend, with 95% confidence intervals in the plot.

	Sham		MI	
	$\beta_1$	$p$	$\beta_1$	$p$
GRS [%]	$0.092 \pm 0.079$	.031	$0.089 \pm 0.126$	.181
GCS [%]	$-0.033 \pm 0.055$	.255	$-0.010 \pm 0.094$	.835
GRSRs [s <sup>-1</sup> ]	$0.021 \pm 0.016$	.014	$0.003 \pm 0.029$	.858
GRSRd [s <sup>-1</sup> ]	$-0.013 \pm 0.033$	.453	$0.014 \pm 0.052$	.597
GCSRd [s <sup>-1</sup> ]	$-0.021 \pm 0.012$	.003	$-0.009 \pm 0.020$	.406
GCSRd [s <sup>-1</sup> ]	$-0.017 \pm 0.027$	.230	$-0.029 \pm 0.038$	.145
RSDI [%]	$-0.051 \pm 0.061$	.118	$-0.041 \pm 0.127$	.534
CSDI [%]	$0.005 \pm 0.053$	.845	$0.041 \pm 0.097$	.412
$\theta_{ss}$ [°]	$-0.045 \pm 0.051$	.093	$-0.001 \pm 0.151$	.988
$\theta_{sd}$ [°]	$-0.019 \pm 0.065$	.575	$-0.125 \pm 0.131$	.074
$\theta_{cs}$ [°]	$0.031 \pm 0.061$	.322	$-0.007 \pm 0.138$	.924
$\theta_{cd}$ [°]	$0.055 \pm 0.055$	.062	$0.131 \pm 0.126$	.054

Table 4.4: Slope values ( $\beta_1$ ), representing change per day, from linear regression of Sham ( $n = 27$ ) and MI ( $n = 23$ ) data, with 95% confidence interval of the slope value as error estimate ( $\beta_1 \pm ci$ ).  $p$ -values correspond to slope estimate from linregression function.

## 4.2 3D strain rate tensor analysis

The results in this section were acquired from analyzing 3D motion in the whole LV segmentation model (see Figure 3.1 for a reminder) using 3D strain rate tensors. Global measurements for all LV slices, as well as regional analysis between a basal and apical half, were performed.

### 4.2.1 Global strain rate and strain

Figure 4.8 demonstrates global strain and strain measurements along radial, circumferential and longitudinal directions for the whole-LV segmentation model of one Sham heart. The curves, and thus the global peak values collected like before, represent a mean of all curves in the sequence of slices of this LV.

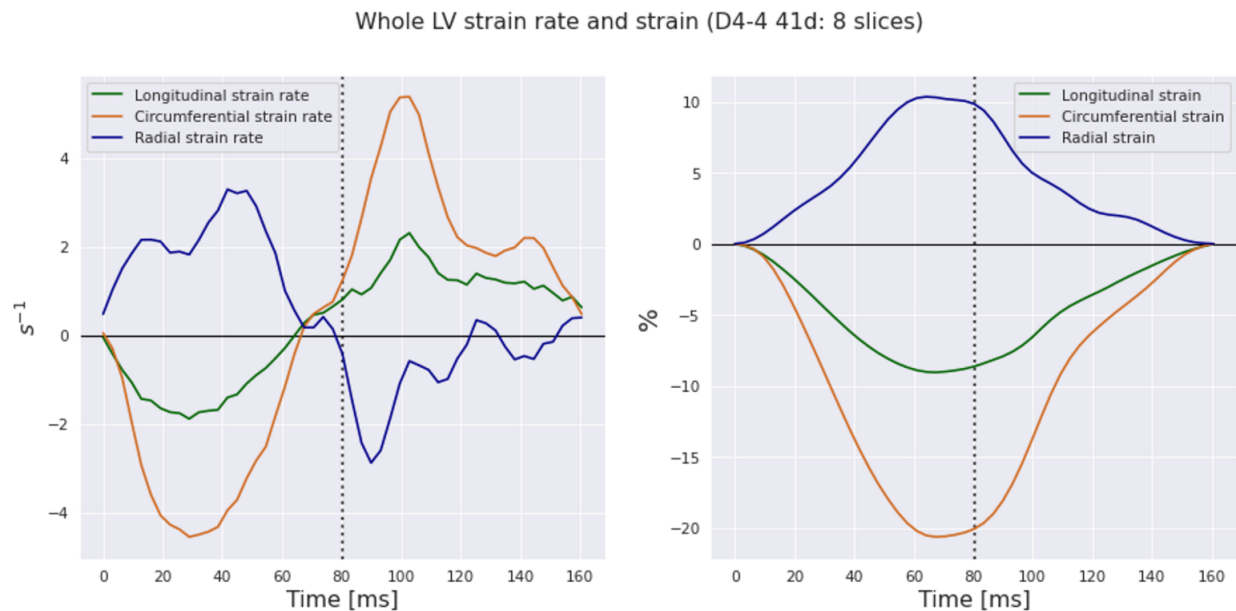


*Figure 4.8: Global strain rate and strain curves for a Sham LV along the radial, circumferential and longitudinal axis. Time point of end systole marked with a dotted line.*

Mean measurements of the global peak parameters in the chronic stage of MI hearts, with Sham control, are presented in Table 4.5. Here we observe significant reduction in magnitude of GCS and GCSRd (like in our 2D analysis) and also in GRSRs. Compared with corresponding measurements, the longitudinal strain rate and strain peak parameters have the highest p-values, showing no significant differences between Sham and MI hearts.

	<i>Sham</i>	<i>MI</i>	<i>p</i>
<i>GRS</i> [%]	$13.57 \pm 2.07$	$9.59 \pm 4.26$	.106
<i>GCS</i> [%]	$-19.50 \pm 1.18$	$-13.35 \pm 3.47$	.007
<i>GLS</i> [%]	$-6.82 \pm 1.49$	$-5.80 \pm 1.36$	.322
<i>GRSRs</i> [ $s^{-1}$ ]	$3.91 \pm 0.52$	$2.69 \pm 0.61$	.014
<i>GRSRd</i> [ $s^{-1}$ ]	$-2.90 \pm 0.25$	$-2.97 \pm 1.89$	.936
<i>GCSR</i> [ $s^{-1}$ ]	$-4.08 \pm 0.44$	$-3.11 \pm 0.93$	.078
<i>GCSRd</i> [ $s^{-1}$ ]	$5.25 \pm 0.29$	$3.89 \pm 0.90$	.014
<i>GLSR</i> [ $s^{-1}$ ]	$-1.58 \pm 0.39$	$-1.46 \pm 0.47$	.671
<i>GLSRd</i> [ $s^{-1}$ ]	$1.93 \pm 0.53$	$1.59 \pm 0.25$	.291

Table 4.5: Mean measurements (mean  $\pm$  std) of global strain and strain rate parameters at the last day after operation for 3D Sham ( $n = 5$ ) and MI ( $n = 4$ ) data. P-values are based on two sample t-tests between the two groups.

## 4.2.2 Regional strain rate and strain

Figure 4.9 shows color-plots describing regional variation across all slices of a Sham heart. Each row in each stack represents the global strain rate or strain curve for that slice, as seen previously in Figure 4.3. The top rows for each component (radial, circumferential and longitudinal) contain the slices closest to the apex (A) of the LV and the bottom rows contain the slices furthest down the base (B).

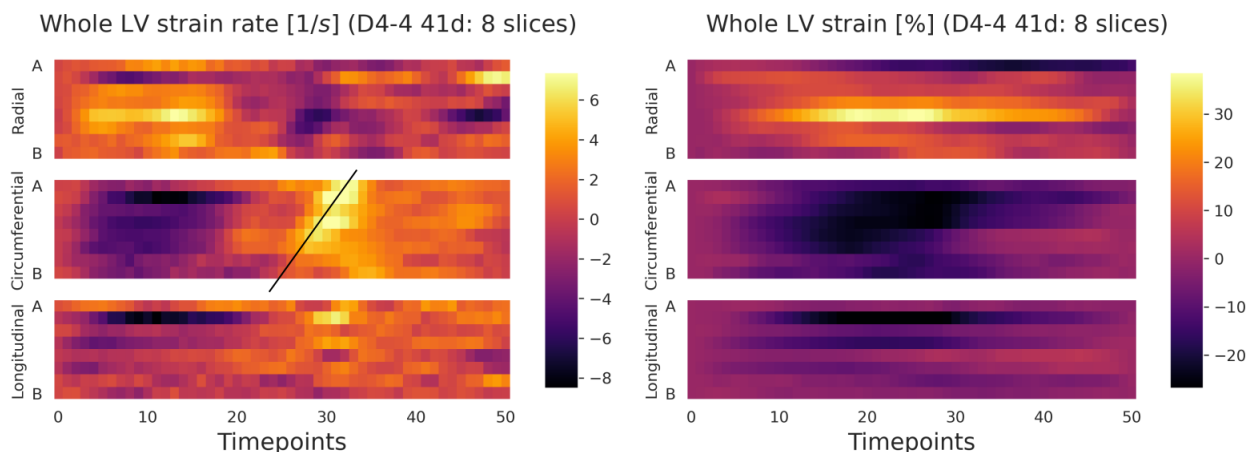


Figure 4.9: Stacks of strain rate and strain curves for one cardiac cycle in a Sham heart, arranged by position along the LV from base (B) to apex (A), assorted by radial, circumferential and longitudinal components. The diagonal line indicates the delay of SRe peaks from base to apex.

From looking at these plots, it appears that circumferential strain rate and strain curves are the most consistent across all slices based on the smoother color plot with more uniform peak values. From the circumferential strain rate stack we also observe a gradual delay in the SRe peaks during relaxation moving from base to apex, indicated with a diagonal line. Comparatively, the radial and longitudinal color plots are more uneven and have less uniform peak values.

### 4.2.3 Eigenvector angle distribution

Examples of angle distribution plots for  $\theta$  and  $\phi$  from two LV slices of a Sham heart are shown in Figure 4.10, where the basal slice is the one we have used previously in the 2D analysis. These plots now describe the average angles of stretch and compression out of the SHAX plane as well with the additional  $\phi$  plots. In Figure 4.11 we have stacked these average angle curves from each LV slice in order from base (B) to apex (A), in the same Sham heart. The mean curves at the bottom represent the mean strain rate direction across all slices, and  $\theta$  peak parameters will be collected from these like we have done before for a single slice. The corresponding  $\phi$  curves, representing average direction of stretch and compression relative to the longitudinal axis, also appears to have distinct systolic and diastolic peaks that will be measured ( $\phi_{ss}$ ,  $\phi_{sd}$ ,  $\phi_{cs}$ ,  $\phi_{cd}$ ).

We have also used these stacks of mean angle curves (for  $\theta$  specifically) to study regional variation between the apical and basal halves of the LV. In Figure 4.12 we have plotted lines that show how the stacks are divided, and the bottom plots now show mean angle curves for the basal and apical slices separately. The previously mentioned, original parameters  $\Delta\theta_{ss}$  and  $\Delta\theta_{cs}$  were measured as the difference between the apical and basal systolic stretch and compression peaks, in an attempt to use higher values (representing angle heterogeneity) as indicators of dysfunction. In these plots we observed that the basal/apical mean angle curves in Sham hearts appeared to agree fairly well with each other during systole, which was the reason we were interested in measuring the  $\Delta\theta$  parameters and use deviation from this agreement as a an indicator of regional dysfunction.

Table 4.6 shows mean measurements from the whole-LV mean angle curves for Sham and MI in the chronic stage. The  $\theta$  peak parameters now appear to show a higher degree of heterogeneity in both the Sham and MI groups compared to what we saw using 2D strain rate tensors, and none of them show significant differences. The  $\theta$  parameters show no significant difference between Sham and MI. The only measurements showing significance are the  $\Delta\theta_{ss}$  and  $\Delta\theta_{cs}$ , showing a higher basal/apical difference in the MI group.

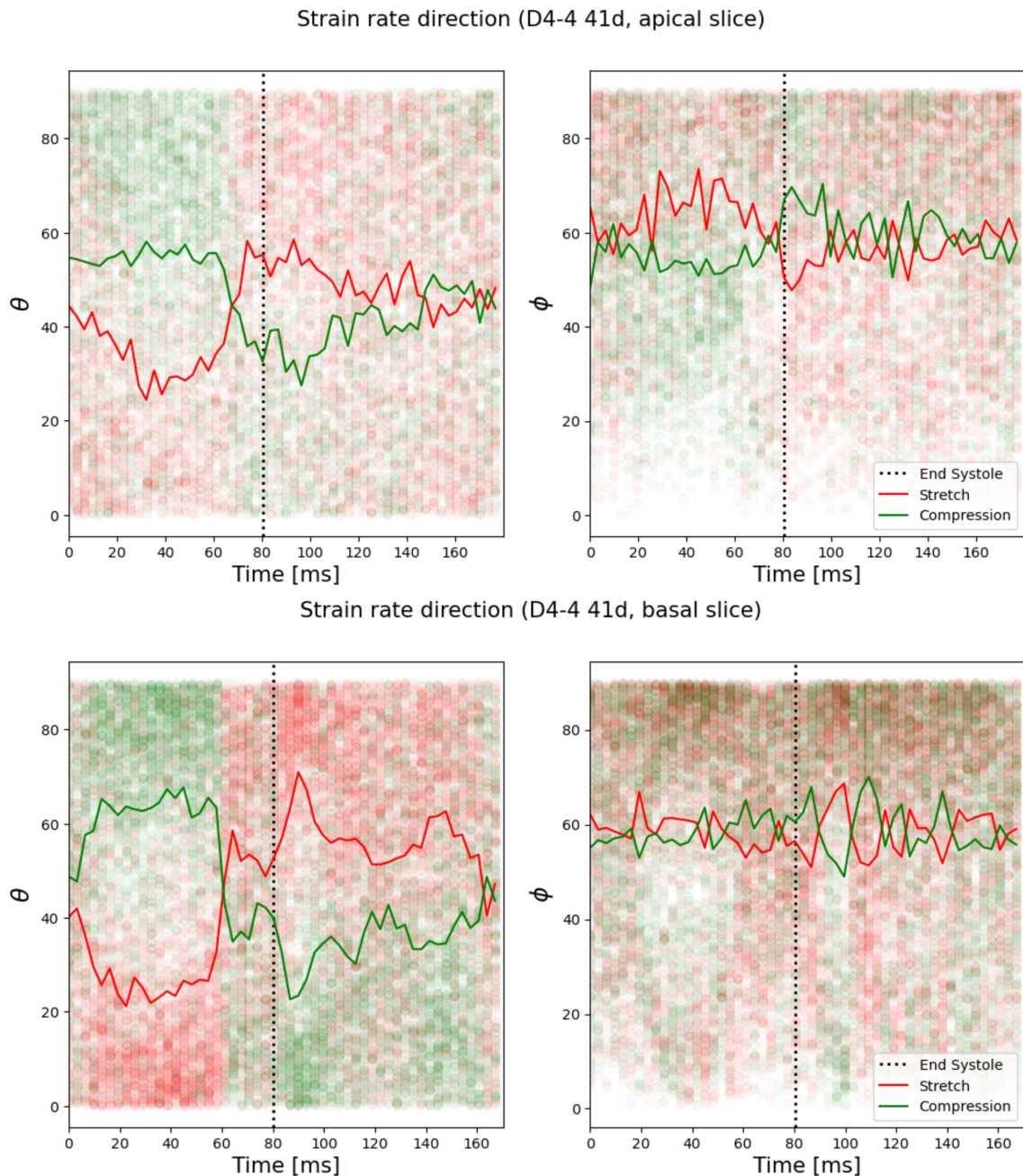
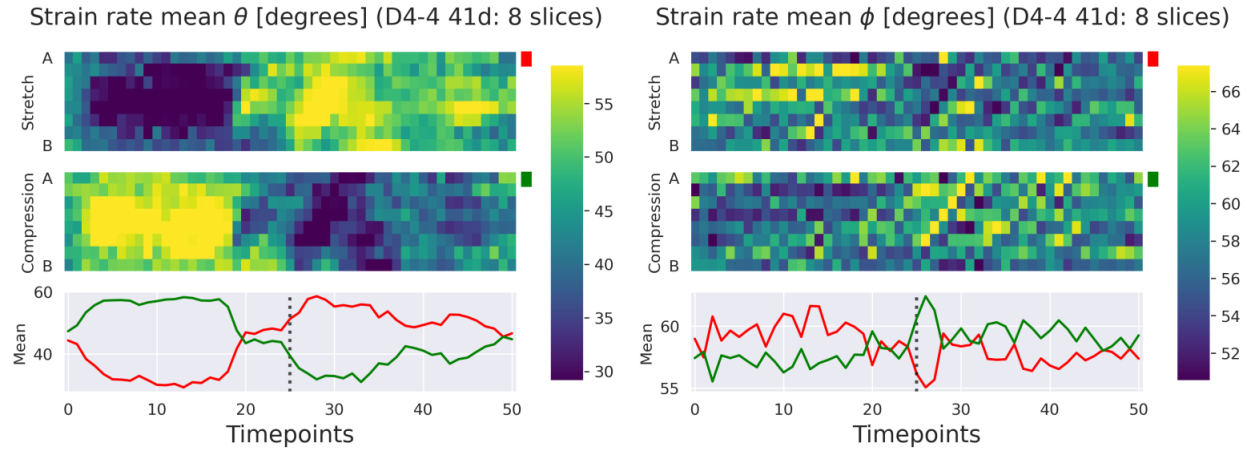
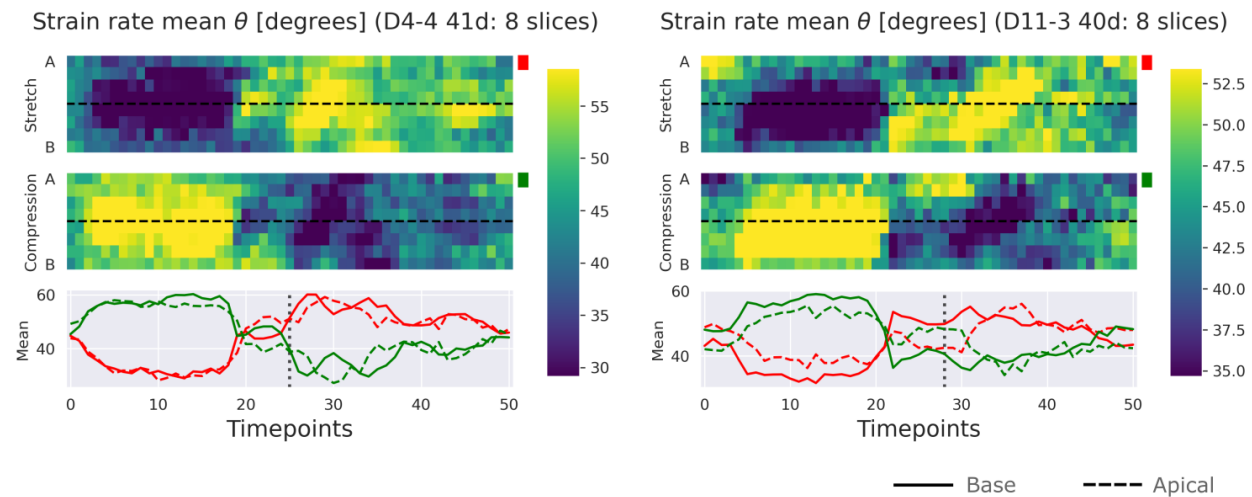


Figure 4.10: Eigenvector angle ( $\theta$ ,  $\phi$ ) distributions from an apical slice and a basal slice over the same cardiac cycle. Mean angle curves in colors corresponding to their distribution.



*Figure 4.11: Stacks of mean angle ( $\theta$ ,  $\phi$ ) curves from all slices for a Sham LV, in order from base (B) to apex (A), over the cardiac cycle. The topmost stack describes direction of stretch, the middle describing compression, and the bottom plot showing the mean stretch and compression angle from all slices. Time point of end systole is marked with a dotted line.*



*Figure 4.12: Stacks of mean in-plane angle  $\theta$  curves from all slices for a Sham heart (left) and MI heart (right) in the chronic stage, in order from base (B) to apex (A), over the cardiac cycle. The stacks are split in the middle to divide them into a basal and apical half. Mean curves are split into representing the basal half (whole red and green lines) and the apical half (dashed red and green lines).*

	<i>Sham</i>	<i>MI</i>	<i>p</i>
$\theta_{ss}$ [°]	$28.93 \pm 1.23$	$32.70 \pm 4.82$	.131
$\theta_{sd}$ [°]	$57.96 \pm 1.52$	$57.30 \pm 5.35$	.798
$\theta_{cs}$ [°]	$60.19 \pm 1.30$	$57.02 \pm 3.33$	.088
$\theta_{cd}$ [°]	$29.94 \pm 1.75$	$32.71 \pm 4.89$	.272
$\Delta\theta_{ss}$ [°]	$0.55 \pm 0.61$	$3.23 \pm 1.92$	.020
$\Delta\theta_{cs}$ [°]	$1.08 \pm 0.36$	$2.57 \pm 1.09$	.023
$\phi_{ss}$ [°]	$62.08 \pm 0.85$	$61.84 \pm 1.50$	.763
$\phi_{sd}$ [°]	$55.69 \pm 0.74$	$56.09 \pm 1.00$	.521
$\phi_{cs}$ [°]	$55.25 \pm 0.83$	$55.26 \pm 1.05$	.982
$\phi_{cd}$ [°]	$61.95 \pm 1.01$	$61.12 \pm 0.86$	.235

Table 4.6: Mean measurements (mean  $\pm$  std) of angle distribution parameters at the last day after operation for 3D Sham ( $n = 5$ ) and MI ( $n = 4$ ) data. P-values are based on two sample t-tests between the two groups.

#### 4.2.4 MI progression

Figure 4.13 shows scatter plots with linear fits for a selection of parameters from Table 4.7 based on statistical significant change over time, or borderline statistical significance in the case of the  $\Delta\theta_{ss}$  parameter.

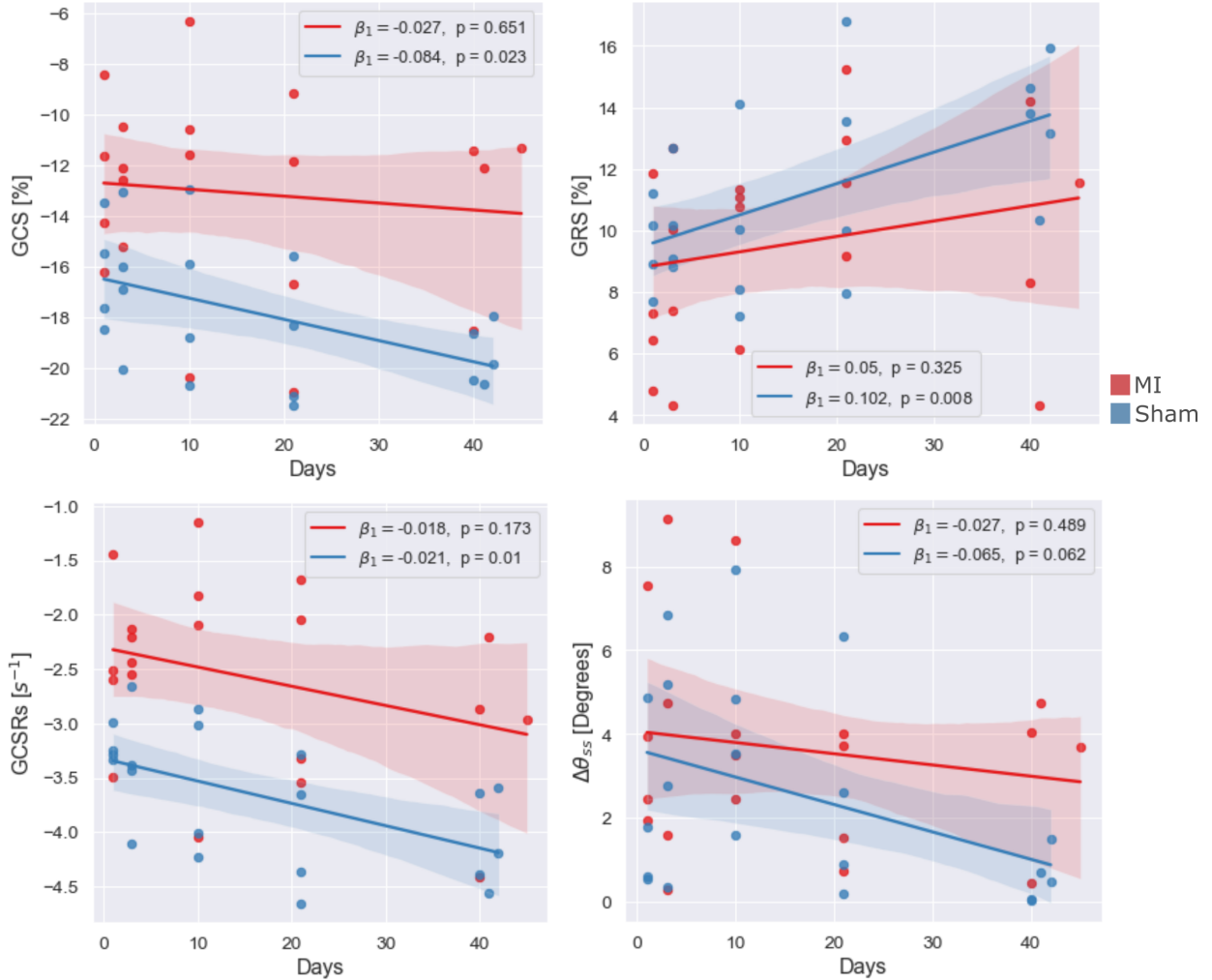


Figure 4.13: Scatter plots of a selection of measured parameters as a function of days and grouped by Sham ( $n = 21$ , blue) and MI ( $n = 20$ , red), from the 3D whole-LV analysis. Slope values  $\beta_1$  from linear regression and corresponding  $p$ -values in legend, with 95% confidence intervals in the plot.

	Sham		MI	
	$\beta_1$	p	$\beta_1$	p
$GRS [\%]$	$0.102 \pm 0.067$	.008	$0.05 \pm 0.097$	.325
$GCS [\%]$	$-0.084 \pm 0.066$	.023	$-0.027 \pm 0.116$	.651
$GLS [\%]$	$-0.028 \pm 0.047$	.264	$-0.039 \pm 0.063$	.234
$GRSRs [s^{-1}]$	$0.019 \pm 0.018$	.048	$0.009 \pm 0.017$	.298
$GRSRd [s^{-1}]$	$-0.023 \pm 0.015$	.010	$-0.013 \pm 0.031$	.404
$GCSRd [s^{-1}]$	$-0.021 \pm 0.014$	.010	$-0.018 \pm 0.024$	.173
$GCSRd [s^{-1}]$	$0.008 \pm 0.024$	.544	$-0.012 \pm 0.032$	.460
$GLSRs [s^{-1}]$	$-0.006 \pm 0.012$	.361	$-0.012 \pm 0.013$	.095
$GLSRd [s^{-1}]$	$0.003 \pm 0.014$	.721	$0.003 \pm 0.014$	.721
$\theta_{ss} [^\circ]$	$-0.033 \pm 0.056$	.263	$-0.029 \pm 0.099$	.570
$\theta_{sd} [^\circ]$	$0.011 \pm 0.051$	.672	$0.005 \pm 0.088$	.915
$\theta_{cs} [^\circ]$	$0.037 \pm 0.043$	.104	$0.019 \pm 0.066$	.580
$\theta_{cd} [^\circ]$	$0.002 \pm 0.066$	.959	$0.016 \pm 0.095$	.749
$\Delta\theta_{ss} [^\circ]$	$-0.065 \pm 0.065$	.062	$-0.027 \pm 0.074$	.489
$\Delta\theta_{cs} [^\circ]$	$-0.041 \pm 0.057$	.175	$-0.028 \pm 0.068$	.433
$\phi_{ss} [^\circ]$	$0.015 \pm 0.023$	.225	$0.013 \pm 0.034$	.468
$\phi_{sd} [^\circ]$	$-0.014 \pm 0.020$	.190	$0.007 \pm 0.024$	.559
$\phi_{cs} [^\circ]$	$0.001 \pm 0.018$	.896	$-0.007 \pm 0.025$	.594
$\phi_{cd} [^\circ]$	$0.011 \pm 0.030$	.471	$-0.003 \pm 0.025$	.819

Table 4.7: Slope values ( $\beta_1$ ) from linear regression of 3D Sham ( $n = 21$ ) and MI ( $n = 20$ ) data, with 95% confidence interval as error estimate ( $\beta_1 \pm ci$ ). p-values correspond to slope estimate from linregression function.

# Chapter 5

## Discussion

The aim of this thesis was to demonstrate that the Selskog method, involving the calculation of strain rate tensors from PC-MRI velocity data, is a viable tool to analyze regional LV dysfunction after infarct as well as investigating the implemented framework's further potential for new kinds of analysis. We have, for the first time, described myocardial dysfunction using strain rate angle distributions and found that MI hearts showed a higher heterogeneity, and we will now attempt to interpret and relate these observations to established literature. In this chapter, we will discuss the results from the 2D and 3D analysis and their physiological implications in detail and compare observations and measurements to similar studies.

### 5.1 2D strain rate tensor analysis

#### 5.1.1 Tensor field visualization

Our framework produces ellipse plots, as shown in Figure 4.1, that visualize strain rate tensors in the LV comparable to literature when it comes to their shape and orientation at various time points. During systole, the plot shows expansion in the radial direction and compression in the circumferential. In the diastole frame we see the opposite. This corresponds to what has been shown before (31), and validates that the tensor fields are calculated correctly. The plots also map ellipse color based on the direction of stretch, or the most positive eigenvalue. Even though the direction of strain rate appears relatively homogenous across the myocardium at these frames, we can also see some variation in hue. The distribution of strain rate directions will be discussed later.

In Figure 4.4 we display an alternative color scheme that distinguishes between the different LV groups used for regional analysis. Here, we also see clearly the reduced total strain rate in the infarction sector of the representative MI heart from the reduced ellipse opacity. The highest strain rate values appear to be in the medial and remote group in the MI heart which is visualized by ellipses that appear more "squeezed". From the corresponding strain curve peaks for each sectors, we see also visually see a clear reduction in the adjacent and infarct sectors. These plots and observations are

comparable to what was presented in the study that our segmentation model was based on, which was also performed on infarcted rat hearts (34).

Based on this we can say that our strain rate tensor visualization framework appears to produce tensor fields and ellipse plots as we intended, with tensor color palettes and opacity visually communicating regional variation in strain rate direction and magnitude, as well as use this to identify regional dysfunction in MI hearts.

### 5.1.2 Tensor field optimization

We used ellipse plots to visually assess the effectiveness of the velocity smoothing. Figure 4.2 illustrates the observed differences between the suggested methods. Exclusion appears to remove ellipses affected by border artifacts with precision. Erosion appears to remove the most intense artifacts while having a possibility of keeping some of them, depending on the quality of the LV mask, in addition of having a more consistent LV shape with no random sections missing.

In the end we decided to go for the simplest alternative and just apply smoothing, with no additional correction. This lets us keep more voxels of data, and we don't risk excluding tensors that may describe complex 3D motion out of plane that appear as if conservation of mass is broken in the 2D SHAX plane. This choice was also made with confidence in the theory established by Selskog et al. (15), in the segmented LV masks designed for the TPM data and the black blood MR sequence used to suppress noisy blood data during acquisition. As a last measure of comparison, we performed the entire statistical analysis using all three alternatives and all results were quite similar with regards to mean-, slope- and p-values. This implies that the corrections don't make a useful difference, and that we might as well choose to avoid the additional operations.

### 5.1.3 Global strain rate and strain

Figure 4.3 shows an example of a strain rate curve and a corresponding integrated strain curve for a Sham heart. From the strain rate plot we see radial expansion and circumferential contraction during systole and the opposite during diastole. Integrating gives a positive peak for the radial strain curve and a negative peak for the circumferential, indicating that the LV circumference contracts and that the LV wall thickness expands as the LV contracts. The radial strain curve also clearly displays a later diastolic peak, which has not been marked. Despite being used in clinical studies (38), our plots do not show the late diastolic strain rate peaks consistently and so we have chosen to focus only on systolic strain rate peak and early diastolic strain rate peak (SRe). This is likely due to mitral fusion, where the peaks are too close to be measured separately (39). Additionally, the strain rate curves appear to be able to pick up the slight peaks during IVR (40). These peaks are easily lost in data with low temporal resolution, so this is an indicator of the high temporal resolution of the TPM data we are using.

Mean measurements of global strain rate and strain parameters are presented in Table 4.1. We find that GCS, GCSR<sub>s</sub> and GCSR<sub>d</sub> in the Sham control group (40+ days after Sham operation) are comparable to literature applying PC-CMR techniques and speckle

tracking to the same rat MI-model that our analysis gets its data from (26)(34). "PC-CMR techniques" in this case refers to calculating strain via displacement, as discussed in section 2.3. These studies also observed lower GCS in the MI hearts than in Sham, which is replicated in our results.

Lower GRS is observed in the MI group compared to Sham, which we expected based on literature studying LV deformation in rat hearts (41). However, the mean magnitude of this parameter (19.79% in Sham at 40+ days) is not comparable as it is significantly lower, where GRS in literature has been found to have values around 25% and 40% in healthy myocardium in rats of similar weight and age to the rats in our MI model.

This surprisingly low GRS is interesting, considering that our global circumferential measurements come from the same trigonometric argument but with measurements comparable to literature and an ability to significantly distinguish between MI and Sham hearts. This could imply that the velocity gradients in our calculations more precisely describe circumferential motion compared with radial motion, which is not unheard of in other methods of strain assessment. A previous study has looked into and compared various methods and modalities used for myocardial strain analysis (25). They found that CMR Tagging produced GCS measurements that were comparable with the other methods, but GRS measurements that were significantly lower than all of the other methods. In general, GRS was found to be less accurate and precise in comparison with GCS. Another study with similar findings speculated that this could be due to the fact that the muscle fiber in the LV wall is oriented circumferentially and longitudinally, while no myocardial fibers are oriented radially (42).

Table 4.4 contains the results of the linear regression analysis, describing how the various functional parameters change over time post-infarct and comparing with the Sham group. We observe from the global parameters that systolic strain rate magnitudes in the Sham group increase significantly over time (GRSRs and GCSR slopes have p-values 0.014 and 0.003). This could be due to the fact that the rats were young during the TPM acquisitions, and that the healthy hearts were still developing and changing as well as recovering from the Sham operation. The MI hearts do not see such a systematic change over time, and their hearts may be struggling to keep up with the development of their healthy counterparts. This aging effect is important to keep in mind in later discussion when we use the Sham group as a control group.

In Figure 4.7 we see scatter plots with Sham and MI linear fits for a selection of parameters, including the systolic strain rate peaks mentioned in the last paragraph. These plots make it clearer that GRSRs is comparable between the groups at day 1, but that the Sham group improves over time and that the MI group remains stagnant. For GCSR there is an immediate difference at day 1 in addition to this gradual improvement. These plots also reveal that the confidence intervals for the MI and Sham groups overlap with the global radial parameters (GRSRs and GRS in this case), which could relate to the fact that our T-tests between mean measurement of these parameters found no significant difference between the groups.

### 5.1.4 Regional strain rate and strain

We can visually assess regional variation from the ellipse plots discussed previously, and quantitatively using strain curves grouped by sector. Figure 4.4A shows an ellipse plot of a Sham LV at early diastole, where we observe a relatively consistent ellipse opacity indicating a homogeneous distribution of strain rate magnitude during LV relaxation. The corresponding strain curves, especially for circumferential strain show similar peak values that appear to occur pretty much simultaneously which supports the visual observation. The radial strain curves appear to show more variation.

Figure 4.4B shows a similar ellipse and regional strain plot for an MI LV 40 days after infarct. Compared to the Sham heart, this ellipse plot clearly shows local dysfunction in the infarct tissue visually from the dimmed ellipse color and from the lower strain peaks in the infarct compared to the other sectors. We can also observe visually from the ellipse plot that the remote sector in the MI LV contains thinner and longer tensors than we see elsewhere which also indicates higher strain rate magnitude. This could be an effect of remodeling, where the tissue further from the infarct compensates for the loss of function.

Figure 4.5 shows us this regional dysfunction (reduced GCS and GRS in infarct) in the full group of chronic MI hearts in the form of box plots, where we show a significant difference in GCS between the infarct sector compared with the medial ( $p = 0.021$ ) and remote sector ( $p = 0.006$ ) as determined by independent two-sample T-tests. This local reduction is an expected result based on previous studies on regional dysfunction in rat hearts (34) (43).

For the GRS parameter, the only statistically significant comparison was in the Sham group between Sector 1 and 4. These sectors are placed the same way for all Sham hearts, as seen in Figure 4.4A, which means that Sector 1 represents measurements in the myocardium close to the thoracic wall (static tissue) while Sector 4 contains measurements in myocardium in the thoracic cavity. This may indicate that the tissue in Sector 4 was able to move more freely in the lab frame, while Sector 1 is adjacent to static tissue that might have reduced its velocity gradients somewhat, despite our smoothing functions. Considering that the strain rate tensors are calculated from velocity gradients that describe local variation of velocity and not absolute velocity values, this may not affect the tensors much after all. Another explanation could be that the pericardium (the outmost layer of the myocardium) gets compromised after Sham surgery and tethers to the chest in a way that restricts movement and deformation (44).

We also see that the standard deviation in GRS in the remote sector for the MI hearts appears increased compared with Sham, which may be an explanation to as why no significant differences are measured for GRS in the MI sectors despite reduced mean values.

Looking into this in our statistical analysis, we saw in Table 4.2 that CSDI and RSDI mean values are lower in the Sham group, meaning that dyssynchrony is higher in the MI group. These observations are supported by literature, where it has been shown that circumferential SDI estimates are lower and have less variance in healthy control

groups compared to hearts inflicted by cardiac disease (45). Physiologically, this delay could be caused by the fact that more infarct tissue is being pulled by its functional neighboring muscle tissue instead of actively deforming itself on time.

### 5.1.5 Eigenvector angle distribution

Strain rate angle distributions, as discussed previously in section 3.2.9, have never been produced before to assess myocardial dysfunction. This means that we cannot directly compare these results with previous studies, so for us to be able to interpret any systematic differences between the Sham and MI groups we need to see those results in the context of our other results.

The first observation we made from the distributions in Figure 4.6 is that the average angle of stretch and compression over time seem to complement the strain rate curves. Just like the strain rate curves, the average angles tell us that stretching happens more in the radial direction during systole and more in the circumferential direction in diastole, opposite for compression.

The angle distributions, however, make it clear that there is a range of directions even in the Sham hearts when the angle concentration is highest. This implies that the LV shortening and wall thickening do not happen completely in the radial and circumferential directions assumed by conventional LV geometry. We technically already observed and noted this when discussing the ellipse plots in Figure 4.1, where this heterogeneity can be seen from the ellipse color scale based on the same  $\theta$  range as the angle distributions.

We attempted to quantify angle heterogeneity from the peak values, and we see that the MI example plot in the figure has peaks closer to  $45^\circ$  and a more heterogeneous distribution. From Table 4.3 we observe that this is the case for all mean measurements of the  $\theta_{ss}$ ,  $\theta_{sd}$ ,  $\theta_{cs}$  and  $\theta_{cd}$  peak values of late stage MI compared with Sham. The comparisons of the systolic parameters  $\theta_{ss}$  and  $\theta_{cs}$  have the lowest p-values, which could mean that the angle distribution analysis is more sensitive to the contracting motions of the LV compared with relaxation.

From linear regression of these parameters we see no significant change over days, unless we count borderline significant change as seen in the MI group for the  $\theta_{sd}$  and  $\theta_{cd}$ . This could imply that the distributions during diastole is affected by MI and gradually become more heterogeneous as the infarct tissue grows. The linear fits for the  $\theta_{sd}$  measurements are included in Figure 4.4 and shows us that the Sham measurements appear to be stagnant in comparison, which implies that this parameter is unchanged by natural aging.

Assuming that increased angle distribution heterogeneity is an indicator of myocardial dysfunction, what is the physiological and mechanical interpretation of this? Our speculation is that this gives insight into the coordination of the myocardium, and relates to how responsive it is to electrical signals. It has been shown before that dyssynchrony can be related to myocardial dysfunction (11), and this was also observed in our own analysis via the CSDI and RSDI parameters. This could relate to our angle dis-

tributions, where dyssynchrony between different sections of the LV could cause it to respond at different times and makes the distributions less focused if the different sectors are at their most homogenic at different times. We also suspect that the strain rate tensors in the infarct tissue to have a wider range of angles, as they describe low magnitude deformation as a result of being pulled by healthier muscle tissue which is a less controlled movement than active, higher magnitude deformation.

These findings also put our strain rate measurements in a new light. The components of the vector decomposition used to measure strain rate were the eigenvalue and eigenvector of the strain rate tensor, representing the magnitude and *direction* of strain rate. We have now shown that the eigenvector angles themselves can be related to myocardial function, which illustrates that not only the magnitude of deformation but also the coordination of the myocardium on voxel scale are important factors in strain analysis. In addition, the fact that the mean curves in Figure 4.6 are roughly symmetric confirms that most 2D strain rate tensors in the LV describes stretch in one direction and compression in an orthogonal direction. The way we define  $\theta \in [0, 90]^\circ$  means that any angle  $\theta_2 = \theta_1 + 90^\circ$  in the range will be mirrored around  $45^\circ$ .

## 5.2 3D strain rate tensor analysis

### 5.2.1 Global strain rate and strain

Figure 4.8 shows an example of global strain rate and strain curves as measured using 3D strain rate tensors, where "global" in the whole-LV model refers to all of the LV covered by slices of MR data. The general curve shapes are as expected; radial and circumferential curves looking similar to the curves measured using 2D tensors (as seen in Figure 4.3), and the longitudinal curve peaks mimic the circumferential in shape and timing (32). The magnitudes for the radial and longitudinal measurements seen in this figure and from mean measurements presented in Table 4.5, however, are lower than expected from literature (41).

Similar to our previous discussion on deviation of GRS from 2D strain rate tensors, this could be an inherent consequence of the tensors calculations and the velocity gradients, but in this case we also suspect the assumption of a cylindrical segmentation model to affect the measurements. The assumption that radial deformation happens exclusively within the SHAX image plane, and that longitudinal deformation only happens perpendicular to it, might be accurate enough at the LV base but less so toward the apex as the LV wall bends inward, at which point it is no longer perpendicular to the SHAX plane. Figure 5.1 illustrates this point, as well as possibly showing how the circumferential component is still effective in this model as circumferential deformation by definition happens parallel to the SHAX plane either way.

The circumferential mean measurements are consistent with what we saw in the 2D analysis, but we can now also observe from the linear regression in Table 4.7 (and Figure 4.13) that GCS significantly increases in magnitude after Sham operation. This was not apparent from our analysis of 2D deformation in a basal slice, so this improvement

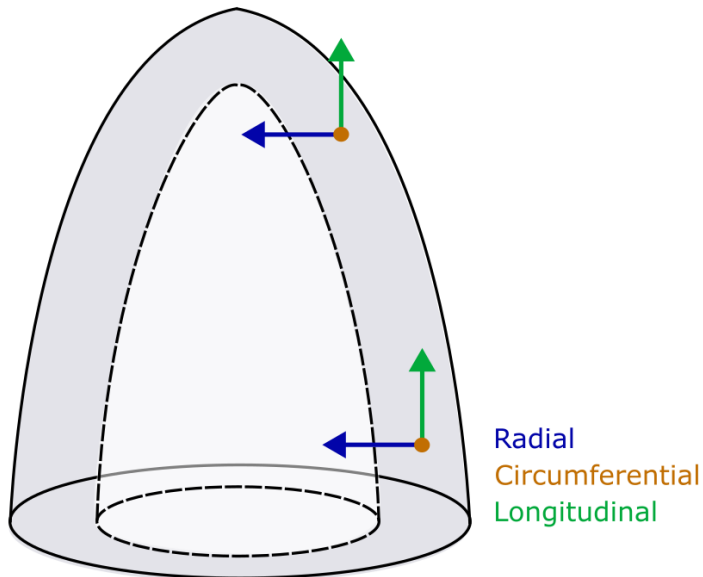


*Figure 5.1: Illustration of the principal strain directions in the whole-LV segmentation model at different levels, in relation to realistic and non-cylindrical chamber wall. The circumferential component is pointing directly out of the image, the radial components are parallel with the SHAX image plane while the longitudinal components are perpendicular.*

in GCS could be linked more strongly to the other slices. Again, we assume that this change could be a combination of natural aging in young rats and recovery from the Sham operations.

## 5.2.2 Regional strain rate and strain

From looking at color plots in Figure 4.9 of a Sham heart we can tell that the circumferential strain peak magnitude appears to be consistent across most of the slices, which could explain why the measurement for whole LV GCS is so consistent with our results from the single slice LV model. We also see that the color plots describing radial and longitudinal strain are not as consistent, with one slice in each clearly showing a higher magnitude peak. This could be an explanation for the low magnitude GRS and GLS measurements. This variation in uniformity across LV levels is not unheard of in established CMR methods. A previous study (46) has compared CMR-FT and CMR tagging performance from different vendors, and from comparing bullseye plots of regional strain it is clear that some of these methods also show heterogeneity in radial and longitudinal strain, whereas circumferential strain appears more consistently uniform.

An interesting observation from these color plots, which is most apparent in the circumferential strain rate stack, is that the diastolic strain rate peaks form a diagonal line. This line implies that after the contraction in the systole, the relaxation begins in the base and then gradually moves toward the apex. Something similar has been observed in the timing of mechanical waves in a range of LV levels measured from high temporal resolution patient data using Tissue Doppler echocardiography (TDE) in a study (47). The study also observes a similar timing in the contraction movement (base to apex), which is not replicated in our own findings.

### 5.2.3 Eigenvector angle distributions

In Figure 4.10 we see angle distribution plots describing the 3D direction of stretch and compression using the  $(\theta, \phi)$  coordinates in a Sham heart. The  $\theta$  plot in the basal slice looks quite similar to the angle distribution plot we saw in Figure 4.6, which suggests that the 2D and 3D strain rate tensors agree on the general in-plane strain rate direction in the LV base. In the apical slice the distributions are more heterogeneous but the general shape of the  $\theta$  curves are preserved.

The  $\phi$  plots do not appear to be as consistent, with the exception of the angles tending to lean more toward  $\phi = 90^\circ$  than  $\phi = 0^\circ$ . Or in other words, more in the SHAX than directly out of it. Other than this, we see in the apical slice that the mean through-plane angle  $\phi$  of stretch and compression have opposite peaks during systole. These tell us that more stretching is happening in-plane and that compression happens more out of plane, which is what we expect because of longitudinal shortening during systole. However, the  $\phi$  plot in the base is not this systematic.

Figure 4.11 shows us that the mean angle curves for in-plane deformation ( $\theta$ ) can be quite consistent across all the slices in a Sham heart, where we observe that the mean curve of stretch and compression look fairly similar to what we saw using 2D strain rate tensors in the LV base. The main difference in shape is that the IVR peak appears to be smoothed away due to variation between slices, but we can still see it as a distinct diagonal shape in the color plots similar to what we saw in Figure 4.9. From Table 4.6 we see that the mean measurements for the  $\theta$  peaks are less polarized (all peak values closer to  $45^\circ$ ) compared with our results from the 2D analysis and show no significant difference between Sham and chronic stage MI. This could be due to the fact that we are now collecting  $\theta$  as in-plane projections of the strain rate direction of eigenvectors that can point in any direction in 3D space, compared with the 2D tensors where the eigenvector pairs are always positioned completely in-plane and orthogonal to each other.

The equivalent stack plot for the  $\phi$  curves show us that the mean curve representing all LV slices is similar to the mean curves from the apical slice in Figure 4.10, with distinct peaks for stretch and compression. The stretch and compression color plots are more jagged and appear less uniform in systole and diastole compared with the  $\theta$  color plots, and result in mean curves that are less smooth. From Table 4.6 we see that the  $\phi$  peak parameters show little polarity between stretch and compression in systole and diastole (compared to  $\theta$ ) and no significant difference between Sham and chronic stage MI, and no significant change was observed from linear regression (Table 4.7).

The plots in Figure 4.12 are meant to compare angle distributions between the basal and apical half of the LV for a Sham and a chronic MI heart. From looking at these plots, it appeared like the mean curves during systole were quite similar in the Sham hearts as seen in the figure from the basal and apical mean curves overlapping. The MI hearts appeared to show some difference due to regional increases in heterogeneity. The diastolic mean curves were less consistent due to the relaxation delay that was discussed previously and can also be seen here. The decision to use the difference between the systolic peaks for stretch ( $\Delta\theta_{ss}$ ) and compression ( $\Delta\theta_{cs}$ ) as a measurement

of angle heterogeneity across the LV were based on this. Mean measurements in Table 4.6 reveal that the Sham group has significantly more uniform  $\theta$  distributions compared with the MI group, which demonstrates that this kind of parameter can identify regional dysfunction.

In Figure 4.13 we see the linear fit of the  $\Delta\theta_{ss}$  parameter for the entire study duration, and we see that the slope value for the Sham group is borderline significant. The linear fit describes this parameter as decreasing in value, implying that the LV angle distributions become more uniform over time for the healthy hearts. We once again attribute this improvement in function to the aging effect discussed before. From this scatter plot and the confidence interval for the Sham group, we can also observe that the variation between measurements appear larger at day 1 than at day 40. This could be due to different aging patterns or spontaneous reactions to the Sham operation before recovery. It has been shown in previous studies that myocardial organization and synchrony have improved on a cellular level over time for young, sham-operated mice (48) (49). Our findings could be connected to this.

### 5.3 Statistical considerations

When we make observations based on the statistical analysis we have designed we should keep in mind the possibility of reaching false conclusions, even with favorable p-values. A type-1 error ("false positive") refers to cases where statistical significance is declared where it is not actually true in the study population, and a type-2 error ("false negative") is when significance is rejected where it actually is true. The small sample size of our study makes it especially vulnerable to type-2 errors (50).

Throughout this chapter we discussed and interpreted results from measurements related to borderline significant p-values (slightly above 0.05) that did not meet our defined significance condition. Even though our model determines that the difference between two mean values is not statistically significant, it does *not* mean that there is a significant similarity between them and there could still be interesting observations to make from such measurements despite the model not being completely confident. The same point goes for the linear regression: if the p-value of a slope is determined to be insignificant, it does not imply that this parameter is significantly unchanged in time.

When we use a linear regression model, we make an assumption of a linear change over time even though the changes could be more complex in reality. However, we are limited by a small dataset. Because of this, we have decided that a simple linear regression model is appropriate and can still reveal interesting progression in our data, but it is important to remember that our model and the calculated p-values estimate how well the measurements fit in a linear model (not that there is significant change whatsoever) and that further investigation with larger datasets could reveal that other models are more accurate.

For the regional strain analysis, we used simple two-sample T-tests to compare the different sectors with the infarct sector. This choice was based on assumptions of how this area shows dysfunction stronger than the others, and it revealed significant differences

in our data. With grouped data like this, however, the option of using mixed models like ANOVA could have been explored. This way, the group differences in our data could have been analyzed unaffected by our prior expectations of specific sectors and we could have avoided using many separate T-tests in our analysis which increases the likelihood of getting false positives (51).

(correlation analysis between different functional parameters other than time could have been explored)

## 5.4 Other limitations and suggestions for future work

We discussed previously how our design for the 3D segmentation model may have affected how the three deformation axes are defined (Figure 5.1). This could be related to the fact that the through-plane angle of strain rate  $\phi$  showed no systematic, periodic movement like the in-plane angle  $\theta$ , and that the longitudinal and radial measurements were lower than expected and more heterogeneous across LV levels compared to the circumferential component (Figure 4.9). A suggestion for future development would be to try to substitute the cylindrical segmentation model with a more advanced model that takes the LV wall curvature into account, as illustrated in Figure 5.2.

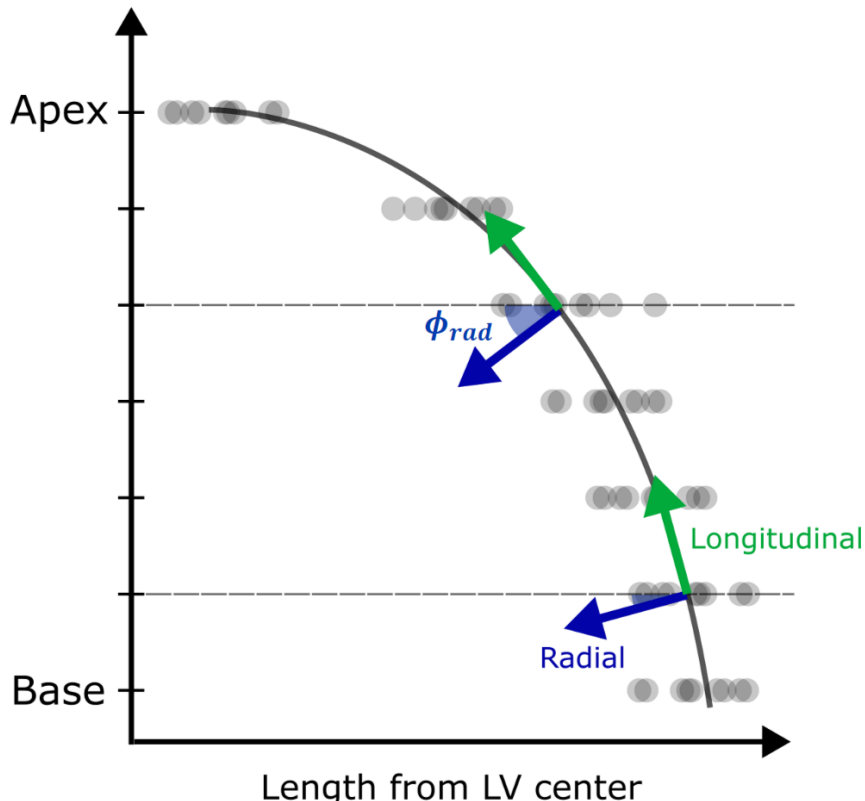


*Figure 5.2: Sketch of an alternative way to define the radial and longitudinal directions level-wise based on a curve fit of the LV shape. The scatter points would be sampled evenly from the LV mask. Each level would have a defined  $\phi_{rad}$  that points perpendicular to the curve at the given level, and the longitudinal direction would be perpendicular to  $\phi_{rad}$ . The circumferential direction would be defined from the in-plane angle  $\theta$  exactly like in the cylindrical model.*

Our 3D segmentation model was designed to study regional variation between whole slices, but the framework could easily have been applied to more complicated segmentation models like the 17-segment LV model that would allow us to make bullseye plots that are common in clinical software (10). Another extension to the framework could be to group strain rate tensors by myocardial layer to study regional transmural variation, as it has been shown previously that strain measurements from the endocardium has a higher magnitude than in the epicardium (25). It has also been shown that the orientation (helix angle) of myocardial fibers change transmurally (52). Based on this, looking at transmural variation of the through-plane angle  $\phi$  from our framework could potentially reveal more systematic patterns throughout the cardiac cycle that could be analyzed.

The development of the strain rate angle distribution analysis was original to this thesis, but could have room for improvement. The mean angle curves used to collect peak values from were used to represent angle uniformity across the LV and appeared to detect dysfunction in the way we intended, but a more direct approach may be more appropriate and could have been explored. One approach could be to quantify the standard deviation of the eigenvector angle distributions in each time point, plot a curve that shows how this value changes over time and using its minima and/or maxima as a way to parameterize myocardial function.

As mentioned previously, the datasets were stored as MATLAB structures and needed to be converted to be interpretable by Python. Due to MATLAB version differences when generating these datasets, the module used to convert single slices of data (using the `scipy.io` module) could not convert the datasets containing stacks of slices. An additional module (`h5py`) was used to convert these datasets to a similar Python structure, which required a significant amount of additional time to implement. Considering that some measurements (in circumferential direction mostly) were very similar in our 2D and 3D analysis, it seems like the data conversion was successful. A more efficient solution, however, would be to implement all of the 2D analysis tools into the 3D analysis class to have a single, flexible class.

In our analysis of 2D strain rate, the tensor plot function was very useful in assessing the tensor field uniformity and creating animations that clearly showed how the tensors react to myocardial motion. It was also very useful during the development of the framework as a troubleshooting tool that. A similar visual tool in the 3D framework is currently lacking, and could have been very useful in understanding the complex deformation motions of the LV throughout the cardiac cycle.

It has been shown that measurements of myocardial strain can be somewhat inconsistent between different modalities, methods and vendors (25). This means that there were no established baseline values for us to compare our measurements with, so extensive validation would be necessary to get a full picture of the applicability of the Selskog method.

Lastly, the study population size was quite small, especially for the mean measurements in the chronic stage (day ~40). More raw data was available to use, but would have to be segmented and processed for it to be interpretable by the Python framework. In

other words, this was an issue of time restriction. Applying the framework on larger datasets, and on a variety of different pathologies, would be a natural continuation in further investigating and developing the strain rate tensor analysis framework.

# Chapter 6

## Conclusion

For this thesis we have implemented a method of measuring myocardial strain rate from MRI acquisitions that had previously never before been used in quantitative analysis. A Python framework was developed to input velocity field data from TPM acquisitions and produce strain rate tensor fields which lets us study myocardial deformation on voxel-scale. The framework includes a tool to visualize the tensor fields as ellipse plots. The framework was applied to LV data from an MI rat model to prove the functionality of the method and to use it to study post-infarct regional dysfunction, using strain and strain rate measurements as well as a new form of analysis using strain rate angle distributions as a functional parameter. The framework was applied to a basal slice of the LV using 2D strain rate tensors and a series of slices using 3D strain rate tensors, describing 2D and 3D LV deformation respectively.

Circumferential strain rate and strain measurements were used successfully, both in global and regional LV analysis using 2D and 3D strain rate tensors, to identify post-infarct hearts with mean values comparable to previous studies using different methods. Strain rate angle distributions produced from the strain rate tensors were used successfully, and for the first time, to identify post-infarct myocardial dysfunction. This result suggests that not only the magnitude of strain rate, but also the direction of strain rate and the organization of the myocardium, have a central role in myocardial dysfunction. Linear regression was used to study the development of all the functional parameters over six weeks, where the most significant differences between the Sham and MI group were due to the Sham group improving over time naturally because the adolescent rats were maturing whereas this development appeared to be hindered for MI rats.

The findings in this thesis demonstrate that strain rate tensor fields describing myocardial deformation have potential as a flexible tool of assessing regional myocardial dysfunction. Future research and development to the applications of strain rate tensors could give a more decisive indication of how effective the method truly is, as well as potentially revealing more about the complex 3D strain dynamics of the heart.



# Bibliography

- [1] G. Savarese, P. M. Becher, L. H. Lund, P. Seferovic, G. M. C. Rosano, and A. J. S. Coats. Global burden of heart failure: a comprehensive and updated review of epidemiology. *Cardiovasc Res*, 118(17):3272–3287, 2023. 1
- [2] G. Savarese and L. H. Lund. Global public health burden of heart failure. *Card Fail Rev*, 3(1):7–11, 2017. 1
- [3] S. Heo, T. A. Lennie, C. Okoli, and D. K. Moser. Quality of life in patients with heart failure: ask the patients. *Heart Lung*, 38(2):100–8, 2009. 1
- [4] NIH NHLBI. What is heart failure? 2022. <https://www.nhlbi.nih.gov/health/heart-failure>, accessed 26.02.24. 1
- [5] Cleveland Clinic. Heart attack: symptoms, causes treatment. 2024. <https://my.clevelandclinic.org/health/diseases/16818-heart-attack-myocardial-infarction>, accessed 04.04.24. 1, 2.2.2
- [6] R. Folse and E. Braunwald. Determination of fraction of left ventricular volume ejected per beat and of ventricular end-diastolic and residual volumes. Experimental and clinical observations with a precordial dilution technic. *Circulation*, 25:674–85, 1962. 1
- [7] A. Scatteia, A. Baritussio, and C. Bucciarelli-Ducci. Strain imaging using cardiac magnetic resonance. *Heart Fail Rev*, 22(4):465–476, 2017. 1
- [8] E. K. Espe. Measuring in vivo regional myocardial function using high field MRI. 2014. University of Oslo, Oslo. 1, 2.1.6, 2.3, 2.3
- [9] F. Valente, L. Gutierrez, L. Rodriguez-Eyras, R. Fernandez, M. Montano, A. Sao-Aviles, V. Pineda, A. Guala, H. Cuellar, A. Evangelista, and J. Rodriguez-Palomares. Cardiac magnetic resonance longitudinal strain analysis in acute ST-segment elevation myocardial infarction: A comparison with speckle-tracking echocardiography. *Int J Cardiol Heart Vasc*, 29:100560, 2020. 1
- [10] J. J. Hjertaas, E. Einarsen, E. Gerdts, M. Kokorina, C. A. Moen, S. Urheim, S. Saeed, and K. Matre. Impact of aortic valve stenosis on myocardial deformation in different left ventricular levels: A three-dimensional speckle tracking echocardiography study. *Echocardiography*, 40(10):1028–1039, 2023. 1, 3.2.1, 5.4

- [11] P. Lim, A. Buakhamsri, Z. B. Popovic, N. L. Greenberg, D. Patel, J. D. Thomas, and R. A. Grimm. Longitudinal strain delay index by speckle tracking imaging: a new marker of response to cardiac resynchronization therapy. *Circulation*, 118(11):1130–7, 2008. 1, 5.1.5
- [12] M. J. Gotte, T. Germans, I. K. Russel, J. J. Zwanenburg, J. T. Marcus, A. C. van Rossum, and D. J. van Veldhuisen. Myocardial strain and torsion quantified by cardiovascular magnetic resonance tissue tagging: studies in normal and impaired left ventricular function. *J Am Coll Cardiol*, 48(10):2002–11, 2006. 1
- [13] G. Pedrizzetti, P. Claus, P. J. Kilner, and E. Nagel. Principles of cardiovascular magnetic resonance feature tracking and echocardiographic speckle tracking for informed clinical use. *J Cardiovasc Magn Reson*, 18(1):51, 2016. 1
- [14] O. A. Smiseth, H. Torp, A. Opdahl, K. H. Haugaa, and S. Urheim. Myocardial strain imaging: how useful is it in clinical decision making? *Eur Heart J*, 37(15):1196–207, 2016. 1
- [15] P. Selskog, E. Heiberg, T. Ebbers, L. Wigström, and M. Karlsson. Kinematics of the heart: strain-rate imaging from time-resolved three-dimensional phase contrast MRI. *IEEE Trans Med Imaging*, 21(9):1105–9, 2002. 1, 2.3, 3.2.2, 3.2.3, 3.2.4, 5.1.2
- [16] A. Bjørnerud and E. K. Espe. *Physics of MR imaging: Compendium for FYS4740/9740*. 2023. 2.1
- [17] E. K. Espe, L. Zhang, and I. Sjaastad. Unwrapping eddy current compensation: improved compensation of eddy current induced baseline shifts in high-resolution phase-contrast MRI at 9.4 Tesla. *Magn Reson Med*, 72(4):1096–102, 2014. 2.1.6
- [18] J. Hennig, M. Markl, B. Schneider, and S. Peschl. Regional myocardial function with tissue phase mapping. *MAGMA*, 6(2-3):145–6, 1998. 2.1.6
- [19] Cleveland Clinic. What is the heart? 2024. <https://my.clevelandclinic.org/health/body/21704-heart>, accessed 07.03.24. 2.2.1, 2.2.1
- [20] H. Fukuta and W. C. Little. The cardiac cycle and the physiologic basis of left ventricular contraction, ejection, relaxation, and filling. *Heart Fail Clin*, 4(1):1–11, 2008. 2.2.1
- [21] Radiopaedia. Late gadolinium enhancement. 2023. <https://radiopaedia.org/articles/late-gadolinium-enhancement-2>, accessed 04.04.24. 2.2.2
- [22] D. Westermann, M. Kasner, P. Steendijk, F. Spillmann, A. Riad, K. Weitmann, W. Hoffmann, W. Poller, M. Pauschinger, H. P. Schultheiss, and C. Tschope. Role of left ventricular stiffness in heart failure with normal ejection fraction. *Circulation*, 117(16):2051–60, 2008. 2.2.2
- [23] S. Frantz, M. J. Hundertmark, J. Schulz-Menger, F. M. Bengel, and J. Bauersachs. Left ventricular remodelling post-myocardial infarction: pathophysiology, imaging, and novel therapies. *Eur Heart J*, 43(27):2549–2561, 2022. 2.2.2

- [24] J. M. Wakeling, S. A. Ross, D. S. Ryan, B. Bolsterlee, R. Konno, S. Dominguez, and N. Nigam. The energy of muscle contraction. I. Tissue force and deformation during fixed-end contractions. *Front Physiol*, 11:813, 2020. 2.3
- [25] M. S. Amzulescu, M. De Craene, H. Langet, A. Pasquet, D. Vancraeynest, A. C. Pouleur, J. L. Vanoverschelde, and B. L. Gerber. Myocardial strain imaging: review of general principles, validation, and sources of discrepancies. *Eur Heart J Cardiovasc Imaging*, 20(6):605–619, 2019. 2.3, 5.1.3, 5.4
- [26] E. K. S. Espe, J. M. Aronsen, M. Eriksen, O. M. Sejersted, L. Zhang, and I. Sjaastad. Regional dysfunction after myocardial infarction in rats. *Circ Cardiovasc Imaging*, 10(9), 2017. 3.1, 5.1.3
- [27] E. K. Espe, J. M. Aronsen, B. Skrbic, V. M. Skulberg, J. E. Schneider, O. M. Sejersted, L. Zhang, and I. Sjaastad. Improved MR phase-contrast velocimetry using a novel nine-point balanced motion-encoding scheme with increased robustness to eddy current effects. *Magn Reson Med*, 69(1):48–61, 2013. 3.1.2
- [28] E. K. Espe, J. M. Aronsen, K. Skardal, J. E. Schneider, L. Zhang, and I. Sjaastad. Novel insight into the detailed myocardial motion and deformation of the rodent heart using high-resolution phase contrast cardiovascular magnetic resonance. *J Cardiovasc Magn Reson*, 15(1):82, 2013. 3.1.2
- [29] W. Kroon, T. Delhaas, P. Bovendeerd, and T. Arts. Structure and torsion in the normal and situs inversus totalis cardiac left ventricle. II. Modeling cardiac adaptation to mechanical load. *Am J Physiol Heart Circ Physiol*, 295(1):H202–10, 2008. 3.2.1
- [30] N. Funabashi, H. Takaoka, K. Ozawa, T. Kamata, M. Uehara, I. Komuro, and Y. Kobayashi. Quantitative differentiation of LV myocardium with and without layer-specific fibrosis using MRI in hypertrophic cardiomyopathy and layer-specific strain TTE analysis. *Int Heart J*, 59(3):523–530, 2018. 3.2.3
- [31] H. Haraldsson, L. Wigstrom, M. Lundberg, A. F. Bolger, J. Engvall, T. Ebbers, and J. P. Kvitting. Improved estimation and visualization of two-dimensional myocardial strain rate using MR velocity mapping. *J Magn Reson Imaging*, 28(3):604–11, 2008. 3.2.4, 5.1.1
- [32] J. He, W. Yang, W. Wu, S. Li, G. Yin, B. Zhuang, J. Xu, X. Sun, D. Zhou, B. Wei, A. Sirajuddin, Z. Teng, S. Zhao, F. Kureshi, and M. Lu. Early diastolic longitudinal strain rate at MRI and outcomes in heart failure with preserved ejection fraction. *Radiology*, 301(3):582–592, 2021. 3.2.6, 3.2.10, 5.2.1
- [33] N. J. Pelc, M. Drangova, L. R. Pelc, Y. Zhu, D. C. Noll, B. S. Bowman, and R. J. Herfkens. Tracking of cyclic motion with phase-contrast cine MR velocity data. *J Magn Reson Imaging*, 5(3):339–45, 1995. 3.2.7, 3.9, 3.2.7
- [34] T. Røe Å, M. Ruud, E. K. Espe, O. Manfra, S. Longobardi, J. M. Aronsen, E. S. Nordén, T. Husebye, T. R. S. Kolstad, A. Cataliotti, G. Christensen, O. M. Sejersted, S. A. Niederer, GØ Andersen, I. Sjaastad, and W. E. Louch. Regional diastolic dysfunction in post-infarction heart failure: role of local mechanical load and

- SERCA expression. *Cardiovasc Res*, 115(4):752–764, 2019. 3.2.8, 5.1.1, 5.1.3, 5.1.4
- [35] Ahmed M. El Missiri. Echocardiographic assessment of left ventricular mechanical dyssynchrony A practical approach. *Echocardiography*, 2014. 3.2.8
- [36] C. Pernet. Null hypothesis significance testing: a short tutorial. *F1000Res*, 4:621, 2015. 3.3.1
- [37] Yale University Courses. Confidence intervals. n.d. <http://www.stat.yale.edu/Courses/1997-98/101/confint.htm>, accessed 15.03.2024. 3.3.1
- [38] A. Soghomonian, A. Dutour, N. Kachenoura, F. Thuny, A. Lasbleiz, P. Ancel, R. Cristofari, E. Jouve, U. Simeoni, F. Kober, M. Bernard, and B. Gaborit. Is increased myocardial triglyceride content associated with early changes in left ventricular function? A (1)H-MRS and MRI strain study. *Front Endocrinol (Lausanne)*, 14:1181452, 2023. 5.1.3
- [39] J. Francis. Mitral E-A fustion and E/A reversal. 2015. <https://johnsonfrancis.org/professional/transmitral-doppler-showing-mitral-e-a-fusion-and-e-a-reversal/>, accessed 17.04.24. 5.1.3
- [40] K Papangelopoulou, M Orlowska, N Cauwenberghs, J U Voigt, T Kuznetsova, and J D'hooge. Prognostic value of strain rate during isovolumic relaxation in a general population. *European Heart Journal*, 2021. 5.1.3
- [41] R. Dragoi Galrinho, A. O. Ciobanu, R. C. Rimbas, C. G. Manole, B. M. Leena, and D. Vinereanu. New echocardiographic protocol for the assessment of experimental myocardial infarction in rats. *Maedica (Bucur)*, 10(2):85–90, 2015. 5.1.3, 5.2.1
- [42] K. Zhang, R. Sheu, N. M. Zimmerman, A. Alfirevic, S. Sale, A. M. Gillinov, and A. E. Duncan. A comparison of global longitudinal, circumferential, and radial strain to predict outcomes after cardiac surgery. *J Cardiothorac Vasc Anesth*, 33(5):1315–1322, 2019. 5.1.3
- [43] A. H. Soepriatna, A. K. Yeh, A. D. Clifford, S. E. Bezci, G. D. O'Connell, and C. J. Goergen. Three-dimensional myocardial strain correlates with murine left ventricular remodelling severity post-infarction. *J R Soc Interface*, 16(160):20190570, 2019. 5.1.4
- [44] E. K. Espe, J. M. Aronsen, G. S. Eriksen, L. Zhang, O. A. Smiseth, T. Edvardsen, I. Sjaastad, and M. Eriksen. Assessment of regional myocardial work in rats. *Circ Cardiovasc Imaging*, 8(2):e002695, 2015. 5.1.4
- [45] A. Petersen, S. N. Nagel, B. Hamm, T. Elgeti, and L. A. Schaafs. Cardiac magnetic resonance imaging in patients with left bundle branch block: Patterns of dyssynchrony and implications for late gadolinium enhancement imaging. *Front Cardiovasc Med*, 9:977414, 2022. 5.1.4

- [46] S. Militaru, R. Panovsky, V. Hanet, M. S. Amzulescu, H. Langet, M. M. Pisciotti, A. C. Pouleur, J. J. Vanoverschelde, and B. L. Gerber. Multivendor comparison of global and regional 2D cardiovascular magnetic resonance feature tracking strains vs tissue tagging at 3T. *J Cardiovasc Magn Reson*, 23(1):54, 2021. 5.2.2
- [47] S. Salles, T. Espeland, A. Molares, S. A. Aase, T. A. Hammer, A. Stoylen, S. Aakhus, L. Lovstakken, and H. Torp. 3D Myocardial Mechanical Wave Measurements: Toward In Vivo 3D Myocardial Elasticity Mapping. *JACC Cardiovasc Imaging*, 14(8):1495–1505, 2021. 5.2.2
- [48] L. Oyehaug, K. O. Loose, G. F. Jolle, A. T. Roe, I. Sjaastad, G. Christensen, O. M. Sejersted, and W. E. Louch. Synchrony of cardiomyocyte Ca(2+) release is controlled by T-tubule organization, SR Ca(2+) content, and ryanodine receptor Ca(2+) sensitivity. *Biophys J*, 104(8):1685–97, 2013. 5.2.3
- [49] W. E. Louch, H. K. Mork, J. Sexton, T. A. Stromme, P. Laake, I. Sjaastad, and O. M. Sejersted. T-tubule disorganization and reduced synchrony of Ca<sup>2+</sup> release in murine cardiomyocytes following myocardial infarction. *J Physiol*, 574(Pt 2):519–33, 2006. 5.2.3
- [50] A. Banerjee, U. B. Chitnis, S. L. Jadhav, J. S. Bhawalkar, and S. Chaudhury. Hypothesis testing, type I and type II errors. *Ind Psychiatry J*, 18(2):127–31, 2009. 5.3
- [51] G. Hamel. Python for Data 26: ANOVA, Version 3. 2020. <https://www.kaggle.com/code/hamelg/python-for-data-26-anova/notebook>, accessed 25.04.24. 5.3
- [52] L. A. McGill, P. F. Ferreira, A. D. Scott, S. Nielles-Vallespin, A. Giannakidis, P. J. Kilner, P. D. Gatehouse, R. de Silva, D. N. Firmin, and D. J. Pennell. Relationship between cardiac diffusion tensor imaging parameters and anthropometrics in healthy volunteers. *J Cardiovasc Magn Reson*, 18:2, 2016. 5.4